Vibrational Energy Harvesting with Piezoelectric Cantilevers

By

Mathias Pielahn

A thesis submitted to the Faculty of Graduate Studies of

the University of Manitoba

in partial fulfilment of the requirements of the degree of

MASTER OF SCIENCE

Department of Electrical and Computer Engineering

University of Manitoba

Winnipeg, Manitoba, Canada

Abstract

Due to decreasing power requirements for wireless networks and other microwatt devices, energy harvesting from ambient vibrations has become a realized power source. Piezoelectric cantilevers are a viable option as the transducer element for converting mechanical to electrical energy. Being able to accurately model piezoelectric cantilevers is important in designing efficient converters needed in the power management circuitry. In this thesis a method is outlined that enables the modeling of the physical behaviour of piezoelectric cantilevers with an equivalent circuit model comprised of RLC circuits.

A MatLab model of piezoelectric cantilevers is developed and verified via literature comparisons. The equivalent circuit model, which is particularly important in electrical engineering of power management circuity, is demonstrated with a proof-of-concept harvester unit design. In the process and for a fraction of the traditional cost, the accuracy and usability of a low-cost vibration shaker is shown.

The design is tested on two real-world applications. The first application is a transformer that has regular vibrations with low harmonic content. The second application are industrial fans with high harmonic content vibrations. The results of both applications show that energy harvesting is possible with a simplistic approach as presented. Further it is shown that high harmonic content, such as was found in the fans, can interfere with energy harvesting in both a constructive and destructive manner leading to further analysis. These findings have implications in designing vibrational energy harvester units as discussed.

Acknowledgments

Developing this thesis work was only possible due the unlimited support of various peoples whom I am grateful to have had the pleasure to meet and interact with. Their dedication has shaped me into the researcher I am today.

First and foremost I am thankful to my knowledgable and patient supervisor Dr. Shaahin Filizadeh. His support is unmatched and has provided me with the tools I needed to succeed. I am also equally thankful to my co-supervisor Dr. Cyrus Shafai. Their insight and physical understanding along with countable hours of stimulating discussions have made my studies more than enjoyable. Through this process I have learned a great deal and for this I am thankful. There is nothing more powerful and liberating than knowledge.

Next I want to thank some of the technical support staff of the Electrical and Computer Engineering department. The technologists Erwin Dirks, Sinisha Janjic, Cory Smit, and Dwayne Chrusch have provided more aid than I can even begin to summarize. Their passion and experience is evident in their work.

Further, I wish to thank a former physics professor of mine Dr. Steen Dannefaer, with whom I've had stimulating and informative discussions regarding piezoelectricity and related physics. His superb teaching style, expertise, and love for the subject continues to inspire me.

Lastly I wish to thank the National Science and Engineering Council of Canada for financial support not just for the duration of my M.Sc. program but also for the majority of my undergraduate studies. I am happy and privileged to live in a country that so actively supports science and engineering research.

Dedication

To all the educators, mentors, and role models whom have encouraged and guided me along my path, I dedicate this thesis to them.

> *If we knew what we were doing, it would not be called research, would it?*
>
> – Albert Einstein, 1879 - 1955

Contents

List of Tables

List of Figures

List of Abbreviations

ac	Alternating current
DMM	Digital multimeter
dc	Direct current
DCM	Discontinuous conduction mode
EoM	Equations of motion
ECM	Equivalent circuit model
PZT	Lead zirconate titanate
MPPT	Maximum power point tracking
PM	Power management
RLC	Resistor, inductor, capacitor
SDOF	Single degree of freedom
SMD	Surface-mount device
WSN	Wireless sensor network
w.r.t.	With respect to
w.l.o.g.	Without loss of generality

Chapter 1

Introduction

1.1 Overview of Piezoelectricity

The properties of piezoelectricity are well understood for quite some time. Indeed the brothers Jacques and Pierre Curie discovered the piezoelectric and inverse-piezoelectric effects in 1880 [1, 2]. Since then many materials, both human-made as well as naturally occurring, exhibiting piezoelectricity have been created and discovered.

Piezoelectricity arises in crystals and ceramics that have a net electric dipole moment (or just moment for short), making them dielectrics. When the material with a moment is subjected to a force applied to one of its surfaces, each dipole experiences a distortion, either growing or shrinking in size. The change in dipole moment establishes a potential difference across the faces due to unbalanced charges. This phenomena is called the *piezoelectric effect*. If the faces are electrically connected either short circuited or via a load, electrons and holes rush towards their respective potential side and neutralize the change of the distorted dipole moment. The inverse of the piezoelectric effect is also present in piezoelectric materials. In other words an applied electric field deforms the physical dimensions of a piezoelectric material.

The identifying difference between crystals and ceramics is the arrangement of the atomic structure. Crystals have a well-defined and periodic structure that can lead to dipole moments. Crystals such as barium titanate have a perovskite arrangement[1] with a central Ti^{4+} atom slightly offset from the geometric centre. With increasing temperature the offset starts to reduce until the central atom is in the geometric centre, causing the dipole moment to vanish. The temperature at which this happens is called the Curie point [3]. Not all crystals have a Curie point however, which is the case when the melting temperature is less than the curie temperature.

Ceramics on the other hand do not have perfect periodic lattice structure like crystals. They can have large regions within them called domains in which the local group of atoms have a crystalline structure. Each domain can be randomly orientated for which the ceramic is then called a polycrystalline ceramic. However, ceramics may also be amorphous or a combination of different arrangements. Thus while piezoelectric crystals already have the individual dipole moments aligned causing a net dipole moment, polycrystalline ceramics usually have a zero net polarization as the various randomly-orientated domains have a cancelling effect.

For a ceramic with piezoelectric properties to have a non-zero net dipole moment, it must be specially treated. This is often done with a high voltage applied to a surface of the ceramic[2] [2, 4]. Upon removal of the voltage the global or macroscopic domain arrangement stays such that the net dipole moment is no longer zero. It is thus evident that high temperatures and/or strong electric fields can destroy artificially arranged domains, much like how temperatures or magnetic fields can destroy the Weiss domains within magnets.

[1]The perovskite arrangement for barium titanate has Ba^{2+} atoms on the corner of the cube, O^{2-} atoms on the faces of the cube and a single Ti^{4+} atom around the centre of the cubic lattice.

[2]Some companies such as Piezo Systems Inc. mark the side where the high voltage was applied with a red line.

1.2 Mathematical Conventions of Piezoelectricity

This section is not essential for the remainder of the thesis. However, it does present the mathematical convention and notation of piezoelectricity. In that regard, piezoelectricity can be made precise with the following standard outline. First the electrical properties are established and following the mechanical properties, which are then combined in a system of equations to describe a piezoelectric material.

When considering the effects of free charges in a material, the electric charge density displacement, $\vec{D}$, is often used [3]. The electric displacement relates the applied electric field, $\vec{E}$, and the polarization density, $\vec{P}$, by

$$\vec{D} = \varepsilon_0 \vec{E} + \vec{P} \tag{1.2.1}$$

where ε_0 is the permittivity in free space. The polarization density vector, which is the total dipole moment per unit volume, accounts for all permanent and induced electric dipole moments. In other words the net polarization or the macroscopic polarization. Isotropic dielectric materials, such as common piezoelectric ceramics with hexagonal structure class[3] $C_{6V} = 6$ mm, have the relationship [3, 5]

$$\vec{P} = \varepsilon_0 [\chi] \vec{E}, \tag{1.2.2}$$

where $[\chi]$ is the electric susceptibility given by $[\chi] = [\varepsilon]/\varepsilon_0 - 1$ with $[\varepsilon]$ the dielectric constant of the material. The electric susceptibility as well as the dielectric constant can be different in each direction and both $[\chi]$ and $[\varepsilon]$ are 3x3 diagonal matrices. The dielectric constant (matrix) is given by

$$[\varepsilon] = \begin{pmatrix} \varepsilon_{11} & 0 & 0 \\ 0 & \varepsilon_{22} & 0 \\ 0 & 0 & \varepsilon_{33} \end{pmatrix}. \tag{1.2.3}$$

[3]A common piezoelectric ceramic with a hexagonal crystal structure of class $C_{6V} = 6$ mm is lead zirconate titanate (PZT) as is introduced further in this section.

Combining equations (1.2.1) and (1.2.2) yields

$$\vec{D} = \varepsilon_0 \vec{E} + \varepsilon_0 [\chi] \vec{E} \tag{1.2.4}$$

$$= [\varepsilon] \vec{E}. \tag{1.2.5}$$

In terms of the mechanical properties all that is needed is a version of Hooke's law:

$$[S] = [s][T] \tag{1.2.6}$$

where $[S]$ is the strain matrix on the material based on the stress matrix $[T]$, with the compliance matrix, $[s]$, relating the two. Strain is a measure of how much the atoms in a material deform. Thus the larger the compliance in one material, the less the deformations will be compared to a material with a lower compliance when a constant stress is applied.

Both stress and strain are in reality $3x3$ matrices. It is common to use the *Voigt notation* [5, 6] to represent a symmetric square matrix of order n in terms of a $mx1$ column vector where $m = n(n+1)/2$. The transformation[4]

$$a_{11} \to a_1, a_{22} \to a_2, a_{33} \to a_3$$

$$a_{23} \to a_4, a_{13} \to a_5, a_{12} \to a_6$$

changes the matrix

$$[A]_{3,3} = \begin{pmatrix} a_{11} & a_{12} & a_{13} \\ a_{12} & a_{22} & a_{23} \\ a_{13} & a_{23} & a_{33} \end{pmatrix} \tag{1.2.7}$$

to the vector

$$[A]_{6,1} = (a_1\ a_2\ a_3\ a_4\ a_5\ a_6)^t, \tag{1.2.8}$$

w.l.o.g. and where the superscript ^{t} denotes the transpose.

Since the stress and strain tensors are symmetric [7], the Voigt notation allows for simpler-looking equations using only vectors as is commonly employed.

[4]Note that an alternative convention is such that $a_{12} \to 4$, $a_{23} \to 5$, $a_{31} \to 6$.

Finally the electric displacement and Hook's law can be combined in the following manner in order to describe piezoelectric materials [3, 5, 7, 8]. The system of equations is then given by:

$$\begin{aligned} \{S\} &= [s^E]\{T\} + [d]^t\{E\} \\ \{D\} &= [d]\{T\} + [\varepsilon^T]\{E\} \end{aligned} \tag{1.2.9}$$

where the subscripts E and T denote measured at constant electric field and stress, respectively. Also the matrix $[d]$ is the matrix of piezoelectric strain constants, and hence $[d]^t$ corresponds to the matrix of inverse piezoelectric strain constants corresponding to the inverse piezoelectric effect. The coupled system in (1.2.9) fully describes a piezoelectric material. For a particular type of crystal or ceramic one needs to specify the compliance and piezoelectric strain matrices.

Over the decades many ceramics have been developed with exhibit strong piezoelectric properties. By far the most widely used commercially is lead zirconate titanate (PZT) defined as [9]

$$Pb\,[Zr_x Ti_{1-x}]\,O_3 \,\text{for}\; 0 \leq x \leq 1. \tag{1.2.10}$$

discovered by Japanese scientists in the early 50's [2]. The compliance and piezoelectric strain matrices for PZT are defined as per the American National Standards Institute (ANSI) and IEEE Standard on Piezoelectricity [6] as

$$[s^E] = \begin{pmatrix} s^E_{11} & s^E_{12} & s^E_{13} & 0 & 0 & 0 \\ s^E_{21} & s^E_{22} & s^E_{23} & 0 & 0 & 0 \\ s^E_{31} & s^E_{32} & s^E_{33} & 0 & 0 & 0 \\ 0 & 0 & 0 & s^E_{44} & 0 & 0 \\ 0 & 0 & 0 & 0 & s^E_{55} & 0 \\ 0 & 0 & 0 & 0 & 0 & s^E_{66} \end{pmatrix}, \text{ with } s^E_{66} = 2(s^E_{11} - s^E_{12}) \tag{1.2.11}$$

and

$$[d] = \begin{pmatrix} 0 & 0 & 0 & 0 & d_{15} & 0 \\ 0 & 0 & 0 & d_{24} & 0 & 0 \\ d_{31} & d_{32} & d_{33} & 0 & 0 & 0 \end{pmatrix} \tag{1.2.12}$$

respectively.

1.3 Operation of Piezoelectric Cantilevers

Generally speaking, a cantilever is a lever attached at one end to a rigid surface or wall via a mounting device. There are many types of cantilevers used in a broad range of applications. A simple example is a diving board, which is a useful analogy when discussing cantilevers. Piezoelectric cantilevers are made out of a piezoelectric material, which in this study is PZT (see Section 1.2). For simplicity, henceforth piezoelectric cantilevers are simply referred as levers as the meaning is clear from context.

There are predominantly two types of levers mentioned in the research literature, yet many others exist. A *unimorph* lever is made of a single PZT layer that may or may not have a supporting structure [10]. The second type, which is the preferred type, is the *bimorph* lever. This sandwich structure has two outer PZT layers and a supporting structure (shim) in the centre [8, 11, 12]. The shim is often made of a brass alloy, but can also be made of stainless steel, a composite material, among other materials [4]. The shim can be omitted but most authors opt to include a shim for structural support as the lever is subjected to mechanical stress and PZT can easily break without support.

The bimorph lever has two types of configurations of the PZT layers. The layers can either be poled for series operation or for parallel operation. This will be discussed in some detail in Section 3.4.1. Lastly and for completion, one can in principle stack any number of PZT layers[5].

All piezoelectric cantilevers are classified as a transducers that convert one form of energy to another. There exists an overwhelming number of different types of transducers which include but are not limit to the conversion of chemical, mechanical, and electrical signals and energies. When a lever converts mechanical energy (in terms of vibration) to electrical energy is it called a *generator* or *sensor*. However, one can also use a lever to convert electrical energy to mechanical

[5]For example, Piezo Systems Inc. [4] sells off-the-shelf four-layer levers, many-layers levers called stacks, as well as custom made levers.

energy that is called an *actuator* or *motor* making use of the inverse piezoelectric effect. A unimorph or bimorph lever can act as either a generator or actuator [4].

In terms of energy harvesting, the generator mode of operation is used. Input ambient vibrational energy bends the lever as to create electrical energy in terms of a potential difference.

1.4 Vibration Sources

One of the most notable applications of vibrational energy harvesting is for powering individual nodes of wireless sensor networks (WSNs). Currently WSNs are powered with batteries that require maintenance for recharging or exchanging the exhausted batteries. This process is costly. A growing trend within WSNs is for each node of the network to be self powered. There are several options to consider to power a node such as solar power, thermal, and vibrational. The vibrational option has three sub-options: piezoelectric, electrostatic, and electro-magnetic. This thesis investigates the piezoelectric vibrational energy harvesting method but does not discuss applications such as WSNs in much detail.

Over the last decade the power requirements for WSNs has decreased dramatically. In 2002 WSNs consuming less than 100 μW was claimed to be attainable [13] while in active mode. Roundy et al. in 2004 designed a custom 1.9 GHz radio that used only 12 mW of power while transmitting [8]. In 2007 Lefeuvre et al. were using an off-the-shelf 2.4 GHz IEEE 802.15.4 radio transceiver that only uses 900 μW of power with a 10 Hz sampling rate, or 90 μW of power with a 1 Hz sampling rate [11]. Further, Wang et al. in 2008 claimed the power consumption for building environment and energy monitoring with their design to be 320 μW while in active mode for five minutes [14]. Whereas for biosensor applications, Mitcheson et al. in 2010 suggest for a WSN to have a total power consumption of 20 μW. Overall modern WSNs as a whole may consume anywhere between a few μW to hundreds of mW of power [15]. However, the active period when the WSNs draw the most current is usually only a few minutes to about 15 minutes. Therefore, if a vibrational energy harvesting system can collect enough energy to meet these demands, such a energy source may become a realistic alternative to batteries.

In order to harvest vibrational energy to be converted to useful electrical energy, the appropriate vibrational sources must be located. The vibrational sources must posses the following three characteristics in order to be useful for application in piezoelectric energy conversion. First the vibrational source must have amplitudes large enough to produce a significant voltage. By this it is meant that if the amplitudes are too small then the voltage produced at the terminals of the piezoelectric cantilever is not large enough to turn on the diodes used in the full bridge of the power management circuit.

Secondly the input vibrations should be periodic in nature and long lasting in order to collect significant energy. If the vibrations are not focused around a particular resonance frequency then tuning the lever to harvest optimal power is not possible. Lastly the vibrations should be around a frequency that is physically manageable to capture with a piezoelectric cantilever. This means that if a vibration source has a frequency in the kilo hertz, then it will be very difficult to tune the lever to such high frequencies. Alternatively if the frequency is too low, say in the tens of hertz, then it is also very difficult to tune the cantilever.

As will become more apparent in Chapter 4, some of these conditions are more relaxed than others and they depend on the physical setup of the piezoelectric cantilever. For example the resonance frequency of the piezoelectric cantilever is proportional to the length of the lever. Therefore, one could in principle tune the lever, by adjusting its length, to practically any vibration source frequency. However, a cantilever a meter in length for example is not practical in applications such as for WSNs. Therefore, there are some engineering restrictions but they change on a case-to-case scenario.

Sources of vibration are quite widespread and can be found nearly anywhere. if the above three conditions are met within a reasonable range then using vibrational energy harvesting can be realized. The following is a table of data collected by Roundy et al. [16] that gives details of some vibration sources.

Table 1.1: SOURCES OF VIBRATIONS FROM REF. [16]

Vibration source	Amplitude [m/s^2]	Peak frequency [Hz]
Car engine compartment	12	200
Base of 3-axis machine tool	10	70
Blender casing	6.4	121
Clothes dryer	3.5	121
Car instrument panel	3	13
Small microwave oven	2.5	121
HVAC vents in office building	0.2-1.5	60
Windows next to a busy road	0.7	100
CD on notebook computer	0.6	75
Second story floor of a busy office	0.2	100

Some of these applications are not quite realizable for vibrational energy harvesting. For example a clothes dryer is usually not in operation for very long and so not much energy could be harvested. The applications studied in this thesis are not listed in this table. They include a laboratory transformer that has a frequency of 120 Hz and typical amplitudes of less than 1 m/s^2, as well as industrial fans that do not have a well defined frequency and amplitudes of a couple m/s^2. These vibration sources will be used to harvest energy as outlined in Chapter 4.

1.5 Power Management Circuit Designs

An ac voltage is produced on the terminals of a piezoelectric cantilever if it is employed in the generator mode as is done in this study. The ac voltage is due to the dipole moments alternating directions with vibrating input accelerations. In an ideal setting the voltage is a perfect sinusoidal wave, however harmonics or distortions are often present in the vibrations. In order to harvest the electrical energy from the mechanical vibrations, the output voltage must be conditioned with the use of a power management (PM) circuit.

Many different PM circuits have been proposed and studied in literature since the early 2000's. Ottman et al. [17, 18] first proposed a two stage PM circuit design. The first stage is a full diode bridge followed by a smoothing or rectifying capacitor. The rectified voltage is the input into a buck converter that is followed by a rechargeable battery. The rectified voltage is kept around half the open-circuit voltage of the generator that harvests the maximum power. This is essentially also equal to the maximum current that can be drawn into the battery since the voltage across the chargeable battery is fairly constant over short intervals. Hence a current sensor was used in the battery branch to adjust the duty cycle in order to realize maximum current drawn. Ottman et al. state that this design is able to harvest about four times more power than PM circuits without a dc-dc converter.

One of the drawbacks of using a buck converter is that it is only able to step down the voltage. This is not always useful especially when the input accelerations decrease or produce a voltage that is already too low. Lefeuvre et al. [11] suggested a buck-boost converter as the secondary stage of the PM circuit. The buck-boost converter is operated at the optimal power point in such a way as to optimize the power flow by matching the impedance of the generator to that of the PM circuitry. This is done by operating the converter in discontinuous conduction mode (DCM) that makes the converter behave as a resistor and enables optimal power flow [19]. Their PM design is focused on circuit simplicity to reduce power consumption of the components that is why they use a low-power crystal clock to drive the power switch for the converter.

Kong et al. [20] improved on this buck-boost PM design by incorporating a closed-loop control that enables the dynamic adaption of the input impedance in order to realize optimal power flow with a wider range of input voltages. In a successive design, Kong et al. [21] further improved their PM circuit by firstly eliminating the large smoothing capacitor and secondly by adapting a resistive matching algorithm as opposed to their previous design that implemented an impedance matching algorithm. If the converter is operated in the range of the open circuit and closed circuit resonance frequencies, then a resistive impedance matching method is quite accurate as the complex impedance is near a minimum[6]. They use a low power oscillator circuit and with their design are able to control both the duty cycle as well as the switching frequency allowing for a wider range of source impedance matching.

Further still, Kong et al. [15] proposed yet another PM design making use of a flyback converter. The flyback converter is also operated in DCM that allows for a maximum power point tracking (MPPT) algorithm to be implemented with a single current sensor. Their system allows for lowering the clock frequency by an order of magnitude as compared to their previous design, thus reducing power dissipation due to fast switching. It should be noted that with their experimental work, a 0.5g (RMS) vibration acceleration input was provided as an input over four piezoelectric bimorph cantilevers that allowed them to harvest a maximum of 8.4 mW of power. As will be shown in the experimental Chapter 4, such a vibration input is rather large and is difficult to find outside an ideal laboratory setting and in a real-world application.

The PM circuit design implemented in this thesis is a simple rectifier bridge followed by a super-capacitor for large storage. The capacitor is protected by a zener diode that clamps down the voltage. This PM circuit does not make use of any dc-dc converter nor optimized power point tracking algorithm. The reason for this is twofold. First of all, from measurements of the input vibrations, the voltage produced by the generator is reasonably close to that of the capacitor rating. Albeit the generator voltage is a little lower sometimes and could be improved upon by using a step-up converter. A buck converter is hardly useful in

[6]See Appendix B for a brief analysis of the impedance of a piezoelectric cantilever.

real-world applications as the source vibrations are usually not strong enough as to produce a voltage that is greater than the rated voltage of the capacitor.

Secondly, as argued by Roundy et al. [8], for applications in WSNs the radio IC typically turns on for only a short period of time (on the order of less than an hour) and then returns to sleep mode. Only during the time when the radio IC receives and transmits the data of whatever that is being measured is the power demand at a peak. The duty cycles are typically close to 1% and so for a large portion of the time the radio IC is in sleep mode and draws little current. During this sleep mode the dc-dc converter typically implemented as outlined above may also be shut down during and thus all the power generated directly goes towards charging the super-capacitor.

The focus of this thesis is not to design an even more efficient PM circuit as has already been done, but to study energy harvesting using piezoelectric cantilevers as a whole. This is further explained in the following section.

1.6 Research Objectives

This thesis is an investigation into energy harvesting of vibrational sources using piezoelectric cantilevers. The entire process starting from the physical description of base vibration as applied to piezoelectric cantilever to the conditioning and harvesting of electrical energy in order to charge a storage device is discussed. The emphasis in this study is twofold. The first focus is placed on modelling the piezoelectric cantilever. The detailed equations describing the physics of the piezoelectric cantilever are derived and then modelled using MatLab. Case studies from literature are used to verify the accuracy of the MatLab script.

The second focus of this study is to build a working prototype harvester unit and use it to charge a super-capacitor. In order to do this a simple power management circuit is used to collect and convert the output electric energy into a more useful form to charge the storage device. This thesis examines two different vibration sources as applications for the harvester unit. The first is a transformer whose housing vibrates at a regular frequency and has relatively clean input vibrations.

The second application includes various industrial fans that have larger amplitudes than the transformer but also posses more harmonics and distortions. These two applications will show not only proof-of-concept for the harvester unit but also help underline some engineering aspects when it comes to designing the harvester unit. As both applications contain higher harmonics in the vibrations to be used and harvested, studying these is useful and more realistic than ideal laboratory settings.

The objective of this thesis is to take a reader unfamiliar to vibrational energy harvesting from a minimal or non-existing knowledge base to a working understanding of the entire system as a whole. As both modelling/simulation as well as experimentation of the vibrational energy harvesting procedure is discussed, a reader should have a good outline of this active field of research after studying this thesis.

1.7 Thesis Organization

This current chapter gives an outline of piezoelectricity, the operation of piezoelectric cantilevers, and a discussion on vibration sources as well as power management circuits. Chapter 2 presents a detailed derivation of the equations describing the physics of piezoelectric cantilevers. First the equations of motion are derived using Hamilton's principle. Then the connection to RLC circuits is drawn that prepares for the simulation aspect.

Chapter 3 is the simulation chapter in which the derived equations from the previous chapter are simulated via a MatLab script. The simulations examine two case studies to verify the accuracy of the code. The ladder part of the chapter prepares for the experimental chapter by examining the actual piezoelectric cantilever used in the applications.

Chapter 4 makes use of the results in the simulation chapter and discusses various experimental procedures. This chapter's main purpose is to demonstrate proof-of-concept of a built energy harvester unit by charging a super-capacitor. Two applications for vibrational energy harvesting are examined in various aspects. These are a laboratory transformer vibrating at 120 Hz and industrial fans with more chaotic and stronger vibrations.

Finally Chapter 5 summarizes the thesis and the results found as well as suggests future works that may be carried out. There are appendices added to the end of this thesis that contain useful information but did not find an appropriate spot within the body of thesis in order to keep the flow. These appendices include a brief outline of Hamilton's principle with a worked-out example in Appendix A followed by a study of the impedance of piezoelectric cantilevers in Appendix B.

Chapter 2

Theoretical Framework

There are three main schools of thought when it comes to mathematically modelling piezoelectric cantilevers [10]. The first is the single degree-of-freedom (SDOF) also known as the lumped parameter model. This technique treats the piezoelectric cantilever as a damped mass-spring system. Early works by Roundy and Wright in 2003 used this model to derive an equivalent generator comprised of a voltage source in series with a capacitor and a resistor [16]. This model was found to be only accurate if the proof mass is rather large and located at the tip of the lever. It has been shown to be inaccurate for small or no tip mass [10, 22].

The SDOF model can be made more accurate if one is only interested in the first mode of vibration and when the proportions of the tip mass are appropriate. Some authors continued to use this model until 2008 such as in [23]. Correction terms were introduced by Erturk and Inman to build on this model [22]. In 2004 Roundy and Wright extended their SDOF model to that that will be presented here [8]. However, their model only is able to capture the dynamics of the first vibration mode. The difference between the two successive models by Roundy and Wright is the added ideal transformer that models the electromechanical coupling of the piezoelectric cantilever. This work was initially done by Flynn and Sanders in 2002 [24]. Among various authors, Ajitsaria in 2007 [25] as well as Khaligh in 2010 [26] make use of this model. Elvin and Elvin acknowledge this model in 2009 [27] but dramatically improve it by adding the multiple modes of vibrations.

Indeed the Elvin and Elvin model as is presented in this chapter belongs to the second type of modelling known as approximate distributed parameter models [10, 22]. As will be shown, this model starts out with Hamiltonian analysis and makes use of three vital assumptions. Of particular interest within these assumptions is the Rayleigh-Ritz and the Euler-Beam assumptions. These are outlined in Section 2.1.

However, Elvin and Elvin were not the first to use the approximate distributed model. It was the pioneering work by Sodano et al. [28] in 2004 that laid the foundation with the Hamiltonian method that is employed in this chapter. Further work was done by duToit et al. the following year [29]. The approximate distributed parameter model is still an approximation to the system, however, as it will be shown, any degree of accuracy can be obtained by considering higher mode shapes. This becomes quite easy to do with programming software.

Finally among several closed form models, Erturk and Inman in 2008 [10] present an exact model that captures the dynamics of the lever quite well. However, this method is not considerd in this study but will only be used as a literature comparison to verify the simulation results in Chapter 3.

This chapter shows the detailed theoretical derivation of the equations of motion (EoM) of a piezoelectric cantilever via the use of Hamilton's principle and three key assumptions. These EoM are a system of second order differential equations containing coupled off-diagonal terms that can be diagonalized to a simpler and more intuitive form. The resulting diagonal system of equations are isomorphic to the second order equations of simple RLC circuits connected in parallel. The end result of the derivation is an equivalent circuit model (ECM) that is able to capture the physics of the mechanical vibrations and the electro-mechanical coupling of a piezoelectric cantilever with simple RCL circuits. The accuracy of the ECM is discussed in Chapter 4 in the context of and in reference to experimental results.

The theory developed in this chapter is for a bimorph piezoelectric cantilever as shown in the the following figure[1]. Tt is straightforward to adapt the geometry to a unimorph or even a stacked cantilever composed of several layers.

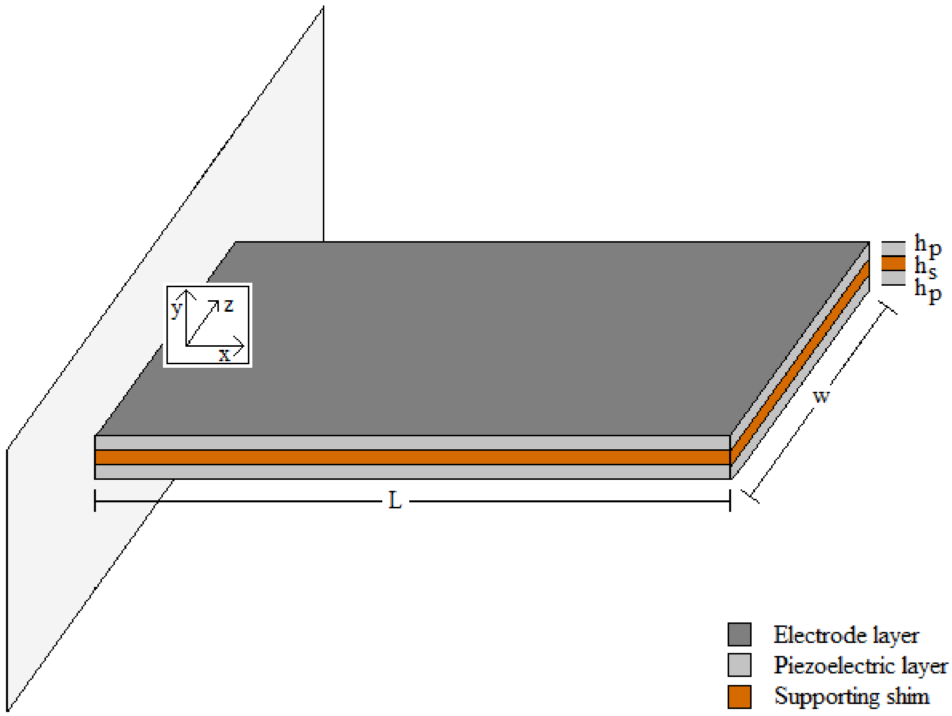

Figure 2.1: The geometry of a bimorph piezoelectric cantilever.

2.1 Hamilton's Principle to Derive the EoM

This section makes use in large part the work contained in references [30] and [28]. For the reader unfamiliar with Hamilton's principle a brief overview and example is provided in Appendix A. Hamilton's principle states that the variation of the action S between time t_1 and t_2 must be zero. In other words

$$\delta S = 0. \tag{2.1.1}$$

[1]The thickness of the electrode layer as seen in Fig. 2.1 is on the order of a one micron [32] and thus can be ignored in the following analyses.

The action is the integral of the Lagrangian that is the kinetic energy minus the potential energy of a physical system [31]. This principle is powerful and reproduces the EoM of a system analogous to using Newtonian mechanics to derive the same EoM. The variation of the action for a piezoelectric cantilever, which behaves as a deformable body, is given by

$$\delta S = \int_{t_1}^{t_2} (\delta T - \delta U + f\delta x) dt = 0, \tag{2.1.2}$$

where T, U, and $f\delta x$ are the kinetic and potential energies and the external applied work respectively and are given by:

$$T = \frac{1}{2}\int_{V_s} \rho_s \dot{\underline{u}}^t \dot{\underline{u}} dV_s + \frac{1}{2}\int_{V_p} \rho_p \dot{\underline{u}}^t \dot{\underline{u}} dV_p \tag{2.1.3}$$

$$U = \frac{1}{2}\int_{V_s} \underline{S}^t \underline{T} dV_s + \frac{1}{2}\int_{V_p} \underline{S}^T \underline{T} dV_p - \int_{V_p} \underline{E}^t \underline{D} dV_p \tag{2.1.4}$$

$$f\delta x = \sum_{i=1}^{nf} \delta \underline{u}(x_i) \underline{f}_i(x_i) - \sum_{j=1}^{nq} \delta \underline{v} \underline{q}_j \tag{2.1.5}$$

with the following definitions. The displacement of the lever away from its equilibrium position is given by $\underline{u}$, which is a vector, denoted by the underbar, and a function of the position along the lever as measured from the base given by x. The subscripts s and p denote the substrate and piezoelectric layers respectively. The integrals are volume integrals over the respective substrate or piezoelectric layers. The densities are given by ρ_s and ρ_p. The external applied force is $\underline{f}$ and the number of applied forces at positions x_i is denoted by nf. Lastly, the applied voltage, in case of operations in the inverse piezoelectric effect, is given by $\underline{v}$ that acts on the charges $\underline{q}_j$ given the number of charges nq. It is noted that in (2.1.4) there is no term of the volume integral $\underline{E}^T \underline{D}$ over the substrate. This is due to the fact that the substrate is not piezoelectric and therefore experiences no electric displacement.

Using the Voigt notation as described in Section 1.2, the system given in (1.2.9) is often also presented in the equivalent form

$$\underline{T} = c^E \underline{S} - e^T \underline{S} \tag{2.1.6}$$

$$\underline{D} = e\underline{S} + \varepsilon^S \underline{E} \tag{2.1.7}$$

in which the relation $e = d_{ij}c^E$ is used where c^E is the modulus of elasticity at constant electric field E. There are various forms of elasticities, however the one of interest is of tensile elasticity that is often denoted by Young's constant of elasticity Y^E.

The coupled system in (2.1.6) and (2.1.7) can be used to eliminate $\underline{T}$ and $\underline{D}$ in (2.1.4) which yields

$$U = \frac{1}{2}\left[\int_{V_s} \underline{S}^t c_s \underline{S} dV_s + \int_{V_p} \underline{S}^t c^E \underline{S} dV_p - \int_{V_p} \underline{S}^t e^T \underline{E} dV_p - \int_{V_p} \underline{E}^t e \underline{S} dV_p - \int_{V_p} \underline{E}^t \varepsilon^S \underline{E} dV_p\right] \tag{2.1.8}$$

Keeping in mind that the integrand of each of these five terms is symmetric, taking the variance simply becomes

$$\begin{aligned}\delta U = &\int_{V_s} \delta\underline{S}^t c_s \underline{S} dV_s + \int_{V_p} \delta\underline{S}^t c^E \underline{S} dV_p - \int_{V_p} \delta\underline{S}^t e^T \underline{E} dV_p \\ &- \int_{V_p} \delta\underline{E}^t e \underline{S} dV_p - \int_{V_p} \delta\underline{E}^t \varepsilon^S \underline{E} dV_p,\end{aligned} \tag{2.1.9}$$

where the factor of $1/2$ is eliminated due to the symmetric matrices after taking the dot product for the variance. Similarly the variance of (2.1.3) becomes

$$\delta T = \int_{V_s} \rho_s \delta\underline{\dot{u}}^t \underline{\dot{u}} dV_s + \int_{V_p} \rho_p \delta\underline{\dot{u}}^t \underline{\dot{u}} dV_p. \tag{2.1.10}$$

Substituting the equations for δU and δT into (2.1.2) yields

$$\begin{aligned}\delta S = \int_{t_1}^{t_2} \Bigg[&\int_{V_s} \rho_s \delta\underline{\dot{u}}^t \underline{\dot{u}} dV_s + \int_{V_p} \rho_p \delta\underline{\dot{u}}^t \underline{\dot{u}} dV_p - \int_{V_s} \delta\underline{S}^t c_s \underline{S} dV_s \\ &- \int_{V_p} \delta\underline{S}^t c^E \underline{S} dV_p + \int_{V_p} \delta\underline{S}^t e^T \underline{E} dV_p + \int_{V_p} \delta\underline{E}^t e \underline{S} dV_p \\ &+ \int_{V_p} \delta\underline{E}^t \varepsilon^S \underline{E} dV_p + \sum_{i=1}^{nf} \delta\underline{u}(x_i)\underline{f}_i(x_i) - \sum_{j=1}^{nq} \delta\underline{v}\underline{q}_j \Bigg],\end{aligned} \tag{2.1.11}$$

remembering that by (2.1.1) this is identically equal to zero.

The above can be greatly simplified with three essential key assumptions outlined as follows.

Assumption 1 - Rayleigh-Ritz procedure and mode shape: Given an assumed mode shape $\phi_i(x)$ and a temporal coordinate $r_i(t)$ the displacement of the beam from the equilibrium position is given by

$$u(x,t) = \sum_{i=1}^{N} \phi_i(x) r_i(t), \tag{2.1.12}$$

where in practice only the first N modes of significance are considered. As long as the set of geometric boundary conditions are satisfied any modal shape can be assumed [27]. Hence the modal shape

$$\phi_i(x) = 1 - \cos\left(\frac{(2i-1)\pi x}{2L}\right) \tag{2.1.13}$$

is assumed to hold true with boundary conditions [5]

$$\phi_i(x=0) = 0, \partial_x \phi_i(x=0) = 0. \tag{2.1.14}$$

The first four modal shapes are plotted in the following figure[2].

[2]By no means is this the only acceptable modal shape. Indeed many authors use a more complicated format such as in [10, 12] and two additional boundary conditions. However, for the purpose of deriving the theoretical framework needed to simulate piezoelectric cantilevers, the assumed mode shapes as presented here is accurate. This is verified in the Chapter 3.

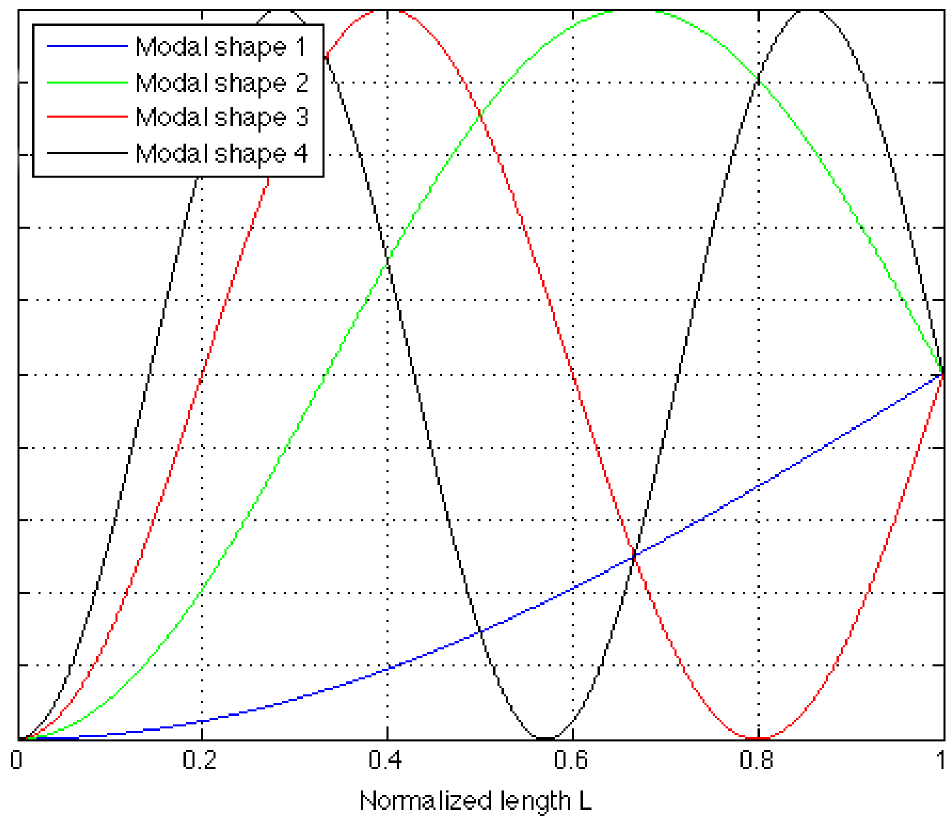

Figure 2.2: Displacement curves of the first four modal shapes with normalized length. The amplitudes in the y-axis are in arbitrary units of length.

Assumption 2 - Euler-Beam theory: Given the distance y from the neutral axis and the second derivative of the displacement w.r.t. the position along the cantilever, the strain in the cantilever can be expressed as

$$\underline{S} = -y\frac{\partial^2 \underline{u}(x,t)}{\partial x^2}, \tag{2.1.15}$$

that, by Assumption 1, can be simplified to yield

$$\underline{S} = -y\underline{\phi}''(x)\underline{r}(t). \tag{2.1.16}$$

Assumption 3 - Constant electric field: Given that the piezoelectric layer is very thin and that no external electric field is applied, the internal electric field within the piezoelectric material is given by

$$\underline{E} = \psi(y)v(t), \tag{2.1.17}$$

where v is the voltage across the electrodes. Considering a bimorph piezoelectric cantilever as in Fig. 2.1 then the electric field can be taken as

$$\underline{E}(y) = \begin{cases} -v/h_p & \text{when } h_s/2 < y < h_s/2 + h_p \\ 0 & \text{when } -h_s/2 < y < h_s/2 \\ v/h_p & \text{when } -h_s/2 - h_p < y < -h_s/2 \end{cases} \tag{2.1.18}$$

With these three assumptions established it is possible to reduce the equation in (2.1.11) into a simpler form given the proper identification of the physical parameters belonging to the bimorph cantilever. The identification of the physical parameters are as follows. The mass matrices for the supporting shim and the piezoelectric layers are given by

$$M_s = \int_0^L \rho_s \underline{\phi}^t(x)\underline{\phi}(x)dx \tag{2.1.19}$$

$$M_p = \int_0^L \rho_p \underline{\phi}^t(x)\underline{\phi}(x)dx, \tag{2.1.20}$$

respectively. Similarly the stiffness matrices are given by

$$K_s = \int_{V_s} y^2 \underline{\phi}^{t\prime\prime}(x) c_s \underline{\phi}^{\prime\prime}(x) dV_s \tag{2.1.21}$$

$$K_p = \int_{V_p} y^2 \underline{\phi}^{t\prime\prime}(x) c^E \underline{\phi}^{\prime\prime}(x) dV_p. \tag{2.1.22}$$

Keeping in consideration that the volume integral over the two piezoelectric layers must be broken into two integrals along the y-axis as the centre shim should not be included. Finally the electromechanical coupling of the piezoelectric material is given by the coupling matrix

$$\theta = -\int_{V_p} y \underline{\phi}^{t\prime\prime}(x) e^t \psi(y) dV_p \tag{2.1.23}$$

while the capacitance of the lever is given by

$$C_p = \int_{V_p} \psi^t(y)\varepsilon^S\psi(y)dV_p \tag{2.1.24}$$

where the volume integral for the capacitance is over both piezoelectric layers[3]. Note that the mass matrices and the stiffness matrices are square matrices of dimension N which is the number of mode shapes considered. The coupling matrix is a vector of dimension N while the capacitance is a scalar value.

Given these physical parameter identifications, (2.1.11) becomes

$$\begin{aligned}\delta S = &\int_{t_1}^{t_2}\Bigg[\delta\dot{\underline{r}}^t(t)(M_s+M_p)\dot{\underline{r}}(t) - \delta\underline{\mathrm{r}}^t(t)(M_s+M_p)\underline{\mathrm{r}}(t) + \delta\underline{\mathrm{r}}^t(t)\theta v(t)\\ &\delta v(t)\theta^t\underline{\mathrm{r}}(t) + \delta v(t)C_p v(t) + \sum_{i=1}^{nf}\delta\underline{\mathrm{r}}(t)\theta^t(x_i)f_i(x_i) - \sum_{j=1}^{nq}\delta\underline{\mathrm{v}}(t)\underline{\mathrm{q}}_j\Bigg]dt\\ =&0.\end{aligned} \tag{2.1.25}$$

With the use of integration-by-part, remembering that at the boundaries (t_1 and t_2) the variation is zero, and rearranging the terms the above can be expressed as

$$\begin{aligned}\delta S = &\int_{t_1}^{t_2}\Bigg[\delta\underline{\mathrm{r}}^t(t)(-(M_s+M_p)\ddot{\underline{r}}(t) - (K_s+K_p)\underline{\mathrm{r}}(t) + \theta v(t) + \sum_{i=1}^{nf}\phi^t(x_i)f_i(t))\\ &\delta v(t)(\theta^t\underline{\mathrm{r}}(t) + c_p v(t) - q(t))\Bigg]dt\\ =&\ 0.\end{aligned} \tag{2.1.26}$$

Examining the above integrant, it is obvious that in order to satisfy the variation of the action to be zero, both grouped terms must be identically zero yielding the

[3]If these equations are applied to the bimorph geometry then special care must be given to whether the two PZT layers are attached in series or in parallel. For the series connection both θ as well as C_p must be divided by 2, whereas for the parallel connection they must be multiplied by 2.

the coupled system of equations

$$(M_s + M_p)\ddot{\underline{r}}(t) + (K_s + K_p)\underline{r}(t) - \theta v(t) = \sum_{i=1}^{nf} \phi^t(x_i) f_i(t) \tag{2.1.27}$$

$$\theta^t \underline{r}(t) + c_p v(t) = q(t). \tag{2.1.28}$$

Equation (2.1.27) is simply Newton's second law of motion [33] $F = ma$ while (2.1.28) is a conservation of charge law. However, these coupled equations are ideal and do not consider any resistive forces. This is not accurate and so the above system must be modified to include energy dissipative terms. There are two types of energy dissipative terms that must be included. The first is to account for the electrical energy that is harvested from the mechanical vibrations. This can be accounted for by Ohm's law such that

$$v(t) = -R\dot{q}(t), \tag{2.1.29}$$

with the resistor R connected between the electrodes of the piezoelectric elements. Thus the energy harvested by the piezoelectric elements can be measured over the resistor directly by counting the charge $q(t)$ that flows past in a given time interval. The second dissipative term comes from mechanical damping caused by the stiffness of the material and external air resistance. It is assumed that the damping follows a relationship known as proportional damping [7] which is given by

$$D = \alpha_0(M_s + M_p) + \alpha_1(K_s + K_p). \tag{2.1.30}$$

The terms α_0 and α_1 can be calculated by experimentally measuring the first two damping ratios ξ_1 and ξ_2. This is explained in further detail in Section 3.4.2. With these two energy dissipative terms the final form of the coupled system of equations describing the bimorph piezoelectric cantilever is given by[4]

$$(M_s + M_p)\ddot{\underline{r}}(t) + D\dot{\underline{r}}(t) + (K_s + K_p)\underline{\mathrm{r}}(t) - \theta v(t) = \sum_{i=1}^{nf} \phi^t(x_i) f_i(t) \tag{2.1.31}$$

$$\theta^t r(t) + c_p R\dot{q}(t) = q(t). \tag{2.1.32}$$

The final term left to define is the external forcing function $f_i(t)$. In practice both within a laboratory setting as well as real world applications of the piezoelectric cantilever, the forcing term is actually nothing but base excitations. Hence the lever is excited at the base and not at the tip at $x = L$. The boundary conditions given in (2.1.14) however are for a cantilever that has a clamped base, which is unlike a forcing term applied to the tip of the cantilever. To overcome this one could re-define the modal shapes that satisfy a new set of boundary conditions appropriate for base excitations on the cantilever. Alternatively using a forcing function corresponding to the inertia of the the cantilever the original modal shapes can continue to be used. As the base is excited the inertia of the cantilever transfers the energy to the tip in turn deflecting it from the equilibrium position. Hence the forcing function is given as

$$f(t) = \int_0^L \int_{-w/2}^{w/2} \int_{-h_s - h_p/2}^{h_s + h_p/2} \rho A\omega^2 \sin(\omega t) dz dy dx, \tag{2.1.33}$$

where A is the vibration amplitude measured in m/s^2 and ρ is the density of the cantilever as appropriate for each material. Lastly, the right-hand term of (2.1.31) can be re-written for practicality as

$$-M^* \ddot{u}_g, \tag{2.1.34}$$

where M^* is the effective forcing vector

$$M^* = \int_0^L \rho\underline{\phi} dx + M_{\text{tip}}\underline{\phi}(L), \tag{2.1.35}$$

M_{tip} is a proof mass placed at the tip when $x = L$, and $\ddot{u}_g$ is the acceleration.

[4]Note that some notation indicating vectors and matrices is relaxed as it is clear from context which each term represents.

2.2 Diagonalization of the system

Apparent from the mass matrix equations in (2.1.19) and (2.1.20), there are off-diagonal terms, or coupled terms, caused by the different mode shapes within the integrals. Although there is nothing wrong with these terms, they do nonetheless make the interpretation of the system to equivalent RCL circuits difficult and non-intuitive. It is possible to diagonalize the system of equations using the Cholesky decomposition technique [7, 27]. The end result of the diagonalization is that all the first non-zero terms correspond to the first mode of vibration, the second non-zero terms correspond to the second mode, and so on. Although this procedure can be made more general, it is tailored to the specific problem of diagonalizing the system in equations (2.1.31) and (2.1.32).

Consider the undamped and unforced simple system

$$M\ddot{r} + Kr = 0. \tag{2.2.1}$$

Given that the mass matrix is symmetric and positive definite, it is possible to decompose the matrix using Cholesky decomposition yielding

$$M = M^{1/2}(M^{1/2})^t. \tag{2.2.2}$$

Thus the simple undamped and unforced system becomes

$$M^{-1/2}M(M^{-1/2})^t\ddot{r} + M^{-1/2}K(M^{-1/2})^t r = 0, \tag{2.2.3}$$

where the first term reduces to $I\ddot{r}$ with I being the identity matrix. The second term can be simplified as

$$\tilde{K} \equiv M^{-1/2}K(M^{-1/2})^t. \tag{2.2.4}$$

It is possible to construct the matrix P containing the corresponding eigenvectors by solving the eigenvalues of $\tilde{K}$ that are to be organized in ascending order. If the matrix P is invertible then the system can be diagonalized. Since this system represents physical measurements (mass, stiffness, damping) all the eigenvalues must be non-zero reals that ensures that the matrix P is invertible. Thus the system can be diagonalized by multiplying throughout by the matrix

$$\Phi \equiv (M^{-1/2})^t P. \tag{2.2.5}$$

This yields the new matrices mass and stiffness matrices for the substrate (s) and the piezoelectric layer (p) as follows respectively:

$$M_{\text{diag}} = \Phi^t M \Phi = I \tag{2.2.6}$$

$$K_{\text{diag}} = \Phi^t K \Phi. \tag{2.2.7}$$

These diagonal matrices are used to re-define the damping matrix as

$$D_{\text{diag}} = \alpha_0 (M_{s,\,\text{diag}} + M_{p,\,\text{diag}}) + \alpha_1 (K_{s,\,\text{diag}} + K_{p,\,\text{diag}}). \tag{2.2.8}$$

The piezoelectric coupling matrix (vector) θ and the effective forcing matrix (vector) M^* must also be changed in accordance to the diagonalization procedure, thus yielding

$$\theta_{\text{diag}} = \Phi^t \theta \tag{2.2.9}$$

$$M^*_{\text{diag}} = \Phi^t M^* \tag{2.2.10}$$

Notice that the total capacitance, which is a scalar value, remains unchanged. Further during the diagonalization process the mass matrix becomes the identity matrix. This has an interesting implication that becomes apparent in the next section.

2.3 Isomorphism to RLC circuits

The final step in the derivation is to establish a bridge between the diagonalized equation of motion to that of an RLC circuit corresponding to each mode of vibration. This is done simply by noticing that both differential equations of the piezoelectric cantilever and the RLC circuit are of second order and so a simple term-by-term correspondence gives the desired result [27].

Consider the RLC circuit in the following figure.

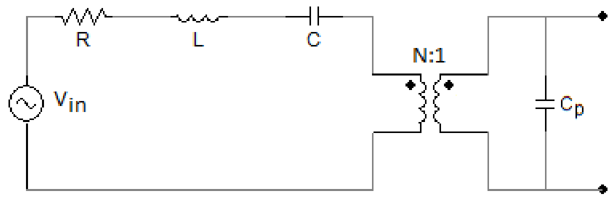

Figure 2.3: RLC circuit with ideal transformer and parallel capacitance.

The transformer is ideal and has a $N:1$ turn ratio. The second order differential equation describing the dynamics of the circuit is given by

$$L\ddot{q} + R\dot{q} + \frac{1}{C}q + NV = V_{\text{in}}, \tag{2.3.1}$$

where the voltage V is across the terminals and $\dot{q}$ is the current trough the RLC branch. Given that the equation derived in the last two sections is

$$(M_{s,\,\text{diag}} + M_{p,\,\text{diag}})\underline{\ddot{r}}(t) + D_{\text{diag}}\underline{\dot{r}}(t) + (K_{s,\,\text{diag}} + K_{p,\,\text{diag}})\underline{r}(t) - \theta_{\text{diag}}v(t) = -M^{*}\ddot{u}_{g} \tag{2.3.2}$$

the isomorphism becomes

$$M_{s,\,\text{diag}} + M_{p,\,\text{diag}} \equiv L \tag{2.3.3}$$

$$D_{\text{diag}} \equiv R \tag{2.3.4}$$

$$K_{s,\,\text{diag}} + K_{p,\,\text{diag}} \equiv \frac{1}{C} \tag{2.3.5}$$

$$\theta_{\text{diag}} \equiv -N \tag{2.3.6}$$

$$M^{*}_{\text{diag}} \equiv V_{\text{in}}, \tag{2.3.7}$$

where the input voltage is normalized to be per unit base acceleration hence the units of V_{in} are $V/m/s^2$. The transformer is considered to be ideal and captures the electro-mechanical coupling of the piezoelectric cantilever.

Recall that due to the diagonalization process the combined mass matrix is equal to the identity matrix implying that the equivalent modal inductance is unity, which makes for a very large inductor. However, for simulation purposes, as shown in Chapter 3, this is not a problem.

With the equivalent circuit model as presented here, it becomes apparent that each mode of vibration corresponds to an RLC circuit as seen in Fig. 2.3, with each successive mode connected in parallel. Further still, the piezoelectric capacitance C_p remains parallel over the output voltage. While all the components and values of the schematic represent *equivalent* components to the piezoelectric cantilever, the parallel output capacitance represents the actual capacitance of the lever.

If considering higher modes, say for example 4 equivalent modes, the schematic becomes as follows [34].

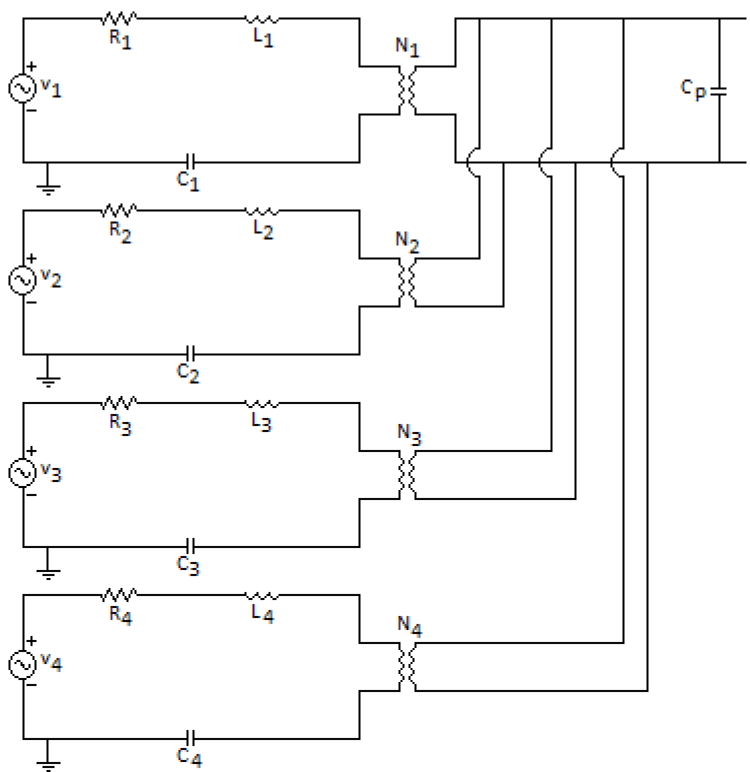

Figure 2.4: Four mode equivalent circuit model schematic.

Including more or less equivalent RLC circuits becomes a question of accuracy.

This topic is addressed in the Chapter 3 discussing simulations of the equations derived.

2.4 Chapter Contributions

This chapter presented the detailed derivation of the theoretical framework in order to fully understand and model a piezoelectric cantilever with an equivalent circuit model comprised of RLC circuits. The procedure started with Hamiltonian analysis, and with the use of three assumptions, solved the equations of motions for a bimorph cantilever. Most of the steps performed in Section 2.1 was due to Sodano et al. in [28] and [30].

The system presented off-diagonal or coupled terms that made the connection to RLC circuits non-intuitive. Hence it is ideal to eliminate the coupled terms by a diagonalization procedure based on the Cholesky decomposition technique [7, 27]. Once this was done it was straightforward to draw an isomorphism to RLC circuits. This complete comparison of the equivalent circuit components for the first mode only was first done by Roundy and Wright [8] with preliminary work by Flynn and Sanders [24]. However, with the model presented by Elvin and Elvin higher modes can be modelled [27].

Although the various steps of this theoretical derivation were done in stages by various authors, this chapter combined all these steps in a fully detailed derivation. This is useful for novel students studying piezoelectric cantilevers. Particularly for electrical engineering applications, the ECM makes it possible to use electronic simulation software such as Spice, PSpice, or PSCAD. Using these tools makes the power management circuit design simpler and more coherent as the entire system (the piezoelectric cantilever as the generator and the power management circuit) can be modelled as one circuit schematic.

Chapter 3

Simulation

The purpose of this chapter is twofold. The first purpose is to test the final equations derived in the previous chapter in a simulation setting and compare these results to published literature. For this, a MatLab script was written that, when provided with the physical parameters of the piezoelectric cantilever, can produce the equivalent circuit components (R, L, C, V_{in}, N, and C_p) for any number of modes of vibration and predict the location and amplitude of said modes.

In order to verify the code, two different case examples are presented. The first case study is of a unimorph cantilever and is to verify that the code can predict the location and amplitude of the first three modes. The second case study is for a bimorph cantilever and is to verify that the code accurately predicts the equivalent circuit components for the first mode of vibration. The bimorph of this study taken from literature is very similar to the cantilever used in the experimentation chapter and so also serves as a good starting point for the next step. Through both of these case studies, a more detailed understanding of the theory and operation of piezoelectric cantilevers is also established. This is discussed in detail after the case studies.

The second purpose of this chapter is to introduce the actual piezoelectric cantilever used in Chapter 4. This will help in being able to predict the modes of vibrations. Knowing the location of the modes of vibration, in particular the first mode, is needed in order to tune the cantilever to a particular frequency. This will prepare the cantilever to be used in real-world applications. Again this becomes useful in the experimental chapter. Further, knowing the equivalent circuit values is useful when designing a power management circuit using software such as PSCAD.

Before proceeding to the case studies, it is useful to derive the expression for the voltage across the attached load in parallel to the piezoelectric capacitance C_p. This is shown in the following section.

3.1 Voltage Output Using ECM

Given the schematic in Fig. 2.4, and in general for any number of modes, it is possible to calculate the voltage output across the piezoelectric capacitance C_p. In order to do this, one would like to simplify each equivalent mode so that the ideal transformer is eliminated. This will make deriving a closed form expression for the output voltage much easier.

The following definitions are made considering only a single mode as in Fig. 2.3. The RLC branch current is I_1 and the voltage on the primary side of the transformer is V_{t_1}. While the current and voltage on the secondary side of the transformer are primed such that they are I_1' and V_{t_1}' respectively. Given this convention, the standard voltage and current relationships on either side of the transformer are give by

$$V_{t_1} = N_1 V_{t_1}', \; I_1' = N_1 I_1. \tag{3.1.1}$$

The branch current can be expressed as

$$I_1 = \frac{V_1 - V_{t_1}}{R_1 + jX_1}, \tag{3.1.2}$$

where

$$X_1 = \omega L_1 - \frac{1}{\omega C_1}. \tag{3.1.3}$$

Combining these equations yields

$$I_1' = \frac{V_1' - V_{t_1}'}{R_1' + jX_1'}, \tag{3.1.4}$$

with

$$R_1' = \frac{R_1}{N_1^2} \tag{3.1.5}$$

$$L_1' = \frac{L_1}{N_1^2} \tag{3.1.6}$$

$$C_1' = C_1 N_1^2 \tag{3.1.7}$$

$$V_1' = \frac{V_1}{N_1}. \tag{3.1.8}$$

Thus with the primed notation each ECM loop becomes a simple RLC branch without the transformer. The four mode ECM with the primed notation is shown in the following figure.

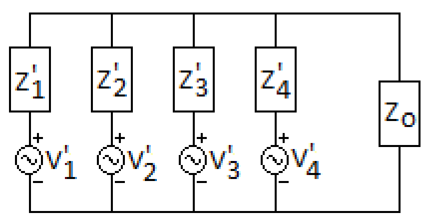

Figure 3.1: Four mode equivalent circuit model schematic with primed notation.

Each branch impedance in the figure is given in general by

$$Z_i' = R_i' + j\omega L_i' + \frac{1}{j\omega C_i'} \tag{3.1.9}$$

where the index i runs from zero to the number of modes considered (*mode*), while Z_o is the output impedance that depends on the load that is attached as well as the piezoelectric capacitance. Hence

$$Z_o = \left(j\omega C_p + \frac{1}{Z_{\text{load}}} \right)^{-1}, \tag{3.1.10}$$

where Z_{load} is the impedance of the attached load.

With the elimination of the ideal transformers within each RLC loop, the i primed branches can be combined into a single equivalent branch. The total impedance of all the branches is given by

$$Z_m = \left(\sum_{i}^{mode} \frac{1}{Z_i'} \right)^{-1}, \tag{3.1.11}$$

with the total equivalent voltage source given by

$$V_m = Z_m \sum_{i}^{mode} \frac{V_i'}{Z_i'}. \tag{3.1.12}$$

Finally the voltage across the output impedance is calculated from a voltage divider given by

$$V_o = \left(\frac{Z_o}{Z_o + Z_{\text{load}}} \right) V_m. \tag{3.1.13}$$

3.2 Unimorph Cantilever Case Study

The geometry of the piezoelectric cantilever in Fig. 2.1 is of a bimorph construction. However, for this case study a unimorph is studied and so the geometry must be adapted accordingly. This change is trivial as the only difference is that the bottom piezoelectric layer of the bimorph is removed. The unimorph studied was examined in detail by Erturk and Inman in [10]. The physical parameters of the lever are shown in the following table.

Table 3.1: PROPERTIES OF THE UNIMORPH IN REF. [10]

Description	Symbol	Value
Elastic modulus piezoelectric	$Y_p\,[GPa]$	66
Elastic modulus substrate	$Y_s\,[GPa]$	100
Piezoelectric coupling	$d_{31}\,[pm/V]$	-190
Electrical permittivity	$\epsilon\,[nF/m]$	15.93
Damping constants	α_0	4.894
	α_1	1.593x10^{-5}
Density piezoelectric	$\rho_p\,[kg/m^3]$	7800
Density substrate	$\rho_s\,[kg/m^3]$	7165
Length	$l\,[mm]$	100.0
Width	$w\,[mm]$	20.0
Piezoelectric thickness	$h_p\,[mm]$	0.4
Substrate thickness	$h_s\,[mm]$	0.5

Given the information as listed in the table it is possible to calculate the equivalent circuit components, and with the voltage equation in (3.1.13), the frequency spectrum. As mentioned before, Erturk and Inman use an analytical approach to calculate the frequency spectrum [10]. Although their approach yields exact answers as opposed to approximations, their method does not yield equivalent circuit values. Their analysis is not considered in detail here but will be used only as a reference guide to check the results as obtained from the simulations.

The equivalent circuit model works by including increasing number of modes in order to obtain the desired accuracy. Usually only the first mode of vibration is of interest which only requires at most four equivalent modes to obtain an accuracy of a hundredths of a hertz. The following plot shows the increase in accuracy as 1, 2, 3, and four equivalent modes are considered. The load attached is a simple 100 Ω resistor, or i.e. $Z_{\text{load}} = 100\,\Omega$.

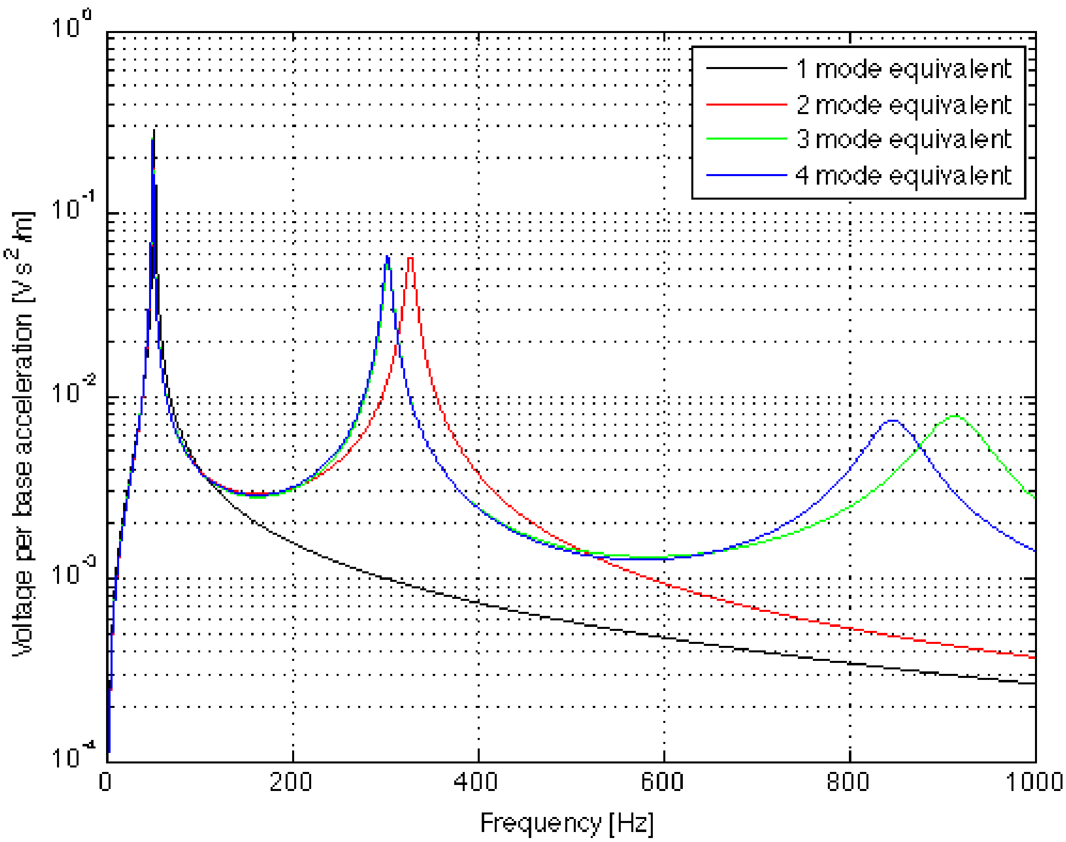

Figure 3.2: The first, second, third, and fourth equivalent mode frequency spectrum of the output voltage per base acceleration over a 100 Ω load resistor. Note that each equivalent mode is accumulative. Therefore, for example, 3 mode equivalent also includes the first and second equivalent mode.

The plot shows that as more modes are considered, the peak location of each resonant frequency increases. In order to verify the accuracy, the following table summarizes the location of the first three resonance peaks given three and four mode equivalent circuit model. The results are compared to Erturk and Inman's analytical results, and those published by Elvin and Elvin [27] for open and closed circuit.

Table 3.2: RESONANCE PEAKS COMPARISON TO LITERATURE

Open load	Erturk & Inman	Elvin & Elvin		Simulations	
Mode	Analytical	3 ECM	4 ECM	3 ECM	4 ECM
1	48.8 Hz	48.86 Hz	48.83 Hz	48.87 Hz	48.81 Hz
2	301.5 Hz	303.90 Hz	303.43 Hz	304.02 Hz	303.46 Hz
3	839.2 Hz	922.78 Hz	853.60 Hz	916.61 Hz	848.35 Hz
Closed load					
1	47.8 Hz	47.87 Hz	47.83 Hz	47.86 Hz	47.83 Hz
2	299.6 Hz	301.90 Hz	301.36 Hz	302.09 Hz	301.45 Hz
3	838.2 Hz	916.51 Hz	851.56 Hz	913.88 Hz	847.37 Hz

It can be seen that the four mode ECM more accurately predicts the mode location. The first and second modes are fairly accurately predicted with only four ECM modes. However, the third mode is still not very accurate even with four modes considered. It should be noted that the Elvin and Elvin results do not quite agree with the simulation results. Interestingly the odd numbered vibration modes (one and three) are better predicted by the simulations results from the MatLab script, while the even numbered vibration mode (2) is better predicted by Elvin and Elvin. Since both the MatLab script and the Elvin and Elvin methodologies make use of the same equations and initial conditions, it is assumed that this systematic difference in mode prediction is due to numerical errors.

Given there is a systematic error between Elvin and Elvin and the simulation results, it is desirable to check that the ECM does indeed reproduce the analytical results of Erturk and Inman. As an example, the third mode for the open load is analyzed with many more higher equivalent modes. This is shown in the following table.

Table 3.3: THIRD MODE CONSIDERATION

Open load	Analytical = 839.2 Hz
ECM	Simulations
10	840.0365 Hz
20	839.4423 Hz
30	839.3806 Hz
40	839.3655 Hz
50	839.3601 Hz
60	839.3577 Hz
70	839.3565 Hz
80	839.3558 Hz

The table shows that although the ECM approaches the analytical results, it does so rather slowly and requires a large number of ECM modes. Given these results as presented in this case study, the MatLab script appears to be working well. If one is only interested in the first two modes, then the ECM is practical and accurate. Since in the literature from which this case study was taken no equivalent circuit components were shown, another case study is presented that makes use of the equivalent circuit components. This is shown in the next section.

3.3 Bimorph Cantilever Case Study

The previous case study showed that any desired accuracy can be obtained using the ECM if enough equivalent modes are considered. The simulation results agreed well with the numerical results of Elvin and Elvin as well as the analytical results of Erturk and Inman. However, only the frequency spectrum of this particular unimorph was studied in literature while the actual equivalent circuit components values were not mentioned. Although one needs these equivalent components to derive the frequency spectrum, it would be ideal to see numerical results found in literature.

This case study compares the calculated equivalent circuit components to a study by Kong et al. [20] and Erturk and Inman [12]. This time the piezoelectric cantilever is a bimorph construction as shown in Fig. 2.1. This cantilever more closely resembles the one used in the experimental Chapter 4, thus making it ideal to study here. The following table outlines the physical parameters of the bimorph cantilever.

Table 3.4: PROPERTIES OF THE BIMORPH IN REF. [12]

Description	Symbol	Value
Elastic modulus piezoelectric	$Y_p\,[GPa]$	66
Elastic modulus substrate	$Y_s\,[GPa]$	105
Piezoelectric coupling	$d_{31}\,[pm/V]$	-190
Electrical permittivity	$\epsilon\,[nF/m]$	13.28
Damping ratios	ζ_1	2.7 %
	ζ_2	2.7 %
Density piezoelectric	$\rho_p\,[kg/m^3]$	7800
Density substrate	$\rho_s\,[kg/m^3]$	9000
Length	$l\,[mm]$	50.8
Width	$w\,[mm]$	31.8
Piezoelectric thickness	$h_p\,[mm]$	0.26
Substrate thickness	$h_s\,[mm]$	0.14

Notice that the damping ratios (ζ_1 and ζ_2) are provided as opposed to the damping constants (α_0 and α_1) that are related by

$$\zeta_r = \alpha_0 \left(\frac{1}{2\omega_r}\right) + \alpha_1 \left(\frac{\omega_r}{2}\right), \tag{3.3.1}$$

where ω_r are the undamped natural frequencies [10, 22]. To continue the flow of this case study, the details are omitted for now and referred to Section 3.4.2 where a detailed explanation is provided albeit for a slightly different bimorph cantilever.

In the study of Kong et al. [20] a tip mass of 12 grams is used. A tip mass, also called a proof mass, is useful in lowering the natural frequency modes of the lever. As will be shown in Section 3.4.3, a proof mass is used to accurately tune the lever to any desired resonance frequency within a given range.

For the purposes of this case study the attached load to the generator is of little importance. Although the natural frequency of the lever does depend on the impedance of the load attached, this study only makes use of the equivalent circuit components. In [20], Kong et al. only present the equivalent circuit values of the first mode, however as will become apparent, they use a much higher number of equivalent modes but drop all the higher order ones besides the first. Doing this makes it possible to accurately capture the first mode dynamics as long as the lever is excited on the first mode resonance frequency. Further, since only a single mode is used in the circuit schematic, the power managements circuit as attached is much simpler to analyze.

The results of their study as well as the simulation results of the first ECM component values using the first, second, third, and fourth equivalent modes is shown in the following table.

Table 3.5: RESULTS OF EQUIVALENT CIRCUIT COMPONENTS

	$L_1\,[H]$	$C_1\,[\mu F]$	$R_1\,[\Omega]$	N_1	$V_1\,[V/g]$
Kong et al.	1	12.1268	15.50671	0.01964044	0.1286161
1 Mode	1	11.8787	15.53196	0.02088165	0.1280333
2 Modes	1	12.0966	15.50973	0.01957526	0.1285328
3 Modes	1	12.1160	15.50779	0.01970899	0.1285887
4 Modes	1	12.1225	15.50715	0.01963003	0.1286046
10 Modes	1	12.1266	15.50674	0.01963970	0.1286153
15 Modes	1	12.1267	15.50672	0.01964103	0.1286158
20 Modes	1	12.1268	15.50672	0.01964036	0.1286160

It can be seen that Kong et al. used several higher equivalent modes to derive the first ECM component values. It is difficult to say how many modes they used due to some numerical errors. However, it is apparent from the table that by the time 20 modes are used, most of the component values match with the simulation results within small errors[1]. Further the piezoelectric capacitance, which is an actual and not equivalent measurement, does not depend on the number of modes considered. Kong et al. calculated a piezoelectric capacitance of $C_p = 41.24\,nF$ while the simulation produced a value of $C_p = 41.26\,nF$. Also, as was mentioned in Chapter 2, due to the diagonalization procedure outlined in Section 2.2, the inductance value is always unity and also does not depend on the modes considered.

Given the good agreement of this and the previous case study, it is accurate to say that the MatLab script functions well and precisely. With this established the focus is now shifted towards the piezoelectric cantilever that was used in the experimental stage. The next section presents the lever and with the aid of the MatLab script tunes the lever to a particular frequency.

3.4 Modified Bimorph Cantilever

The piezoelectric cantilever used in the experiments of Chapter 4 is a bimorph type similar to the one depicted in Fig. 2.1. This section establishes the required background and set up that is useful for the experimental chapter.

3.4.1 Original Cantilever Description

A bimorph configuration has two layers of piezoelectric material which essentially can double the power of a unimorph cantilever. However, the more layers are

[1] It is conjectured that at such a high mode number, the values that do not agree to every decimal listed is due to numerical rounding. This can be seen in the monotonically convergence of the component values except in the turn ratio N_1 that for 15 modes overshoots Kong's value and then for 20 modes reduces again.

added the smaller the displacement of the lever becomes and so less power can be harvested. Therefore, a stack of more than two piezoelectric layers may not be as ideal in this application of vibrational energy harvesting. A bimorph cantilever is therefore the preferred geometry in literature.

The piezoelectric cantilever was purchased from Piezo Systems Inc. [4] and is very similar to the one used in the previous case study [10, 20]. The characteristics and properties of the cantilever are essential for an in-depth analysis and understanding. A thorough description is presented in this subsection.

Piezo Systems Inc. makes use of a particular naming convention for their cantilevers. The part numbers are outlined as follows.

Part number:	$(letter)$	$(\#)$	$(\#\#)$	$(-letter\#)$	$(letters)$	$(-\#\#\#)$	$(letter)$
Placeholder:	A	B	C	D	E	F	G

With the following placeholder descriptions:

- A Mounting style.[a] T = unmounted, Q = quick mount.
- B Number of piezo layers.
- C Total lever thickness measured in milli-inches.
- D Piezo material.
- E Centre shim material. Blank = brass alloy.
- F Size.
- G Polarization. Y = parallel, X = series.

Note:

a The quick mount option, Q, also includes a SMD high-resistance bleeding resistor, as shown in Fig. 3.4. The purpose of the bleeding resistor is to discharge the piezo layers when not in operation.

The purchased cantilever had the following part number:

Q 2 20 -A4 -503 Y

The "-A4" is the piezoceramic PSI-5A4E[2]. Hence this lever is a quick mount, bimorph, 0.020 inches total thickness, made of PSC-5A4E PZT, brass shim, is 1.25 inches by 2.5 inches in area and is Y-poled.

Piezo Systems Inc. marks a PZT side with a red line to indicate the side on which a high voltage was supplied during the manufacturing process [4]. This determines which way the sheet of PZT is polarized (See Section 1.2). As mentioned the cantilever is Y-poled for parallel operation. This is one of the differences between the cantilever used in this study and the one by Kong et al. as they use the X-poled for series operation. The difference lies in how the two PZT layers are attached. In their study the PZT layers are attached in series which doubles the voltage across the terminals, whereas in this study the layers are attached in parallel which doubles the current flow.

Both types are useful depending on how the cantilever is operated. A higher voltage is useful for when the input accelerations are small in amplitude. Most power management circuits, which are to transform the ac current output of the cantilever into a useful format to charge a super capacitor or a battery, make use of a rectifying diode bridge. If the acceleration amplitudes are small then only a small voltage is produced across the terminals that may not be enough to turn on the diodes. Therefore, a series poling is useful. However, if the amplitudes are large enough such that the diodes can be turned on, then a parallel poling helps in drawing a higher current that in turn charges the super capacitor or battery faster.

The following figure shows the unaltered[3] cantilever.

[2]According to Piezo Systems Inc. this material "is an industry type 5A (Navy Type II) piezoceramic. Thin vacuum sputtered nickel electrodes produce extremely low current leakage and low magnetic permeability. 5A has a wide temperature range and is most insensitive to temperature." The Ni electrodes on both sides are $\approx 1\mu$m thick in total [32].

[3]In Subsection 3.4.3 the MatLab script is used to calculate how much of the cantilever needs to be cut off in order to tune it to a particular frequency.

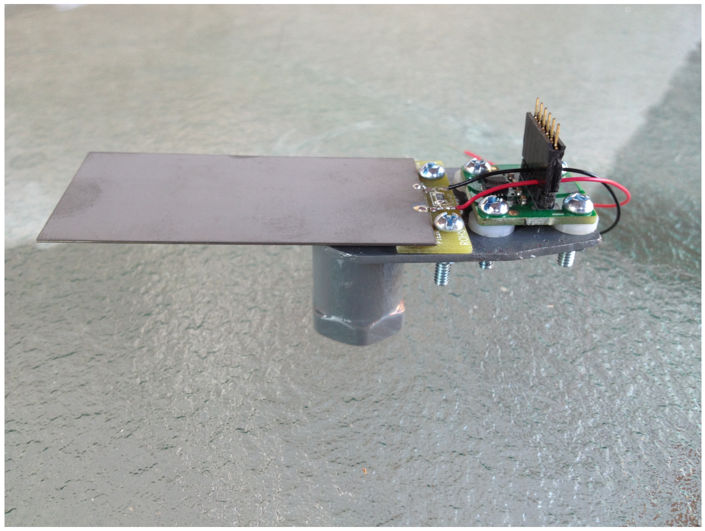

Figure 3.3: The piezoelectric cantilever as seen from the side with an accelerometer. Both are attached to a grey mount below.

This figure shows the cantilever with the quick mount (in yellow) as purchased. The green PCB with the black connector is the accelerometer (See Section 4.2). Both the quick mount and the accelerometer are attached to a mount that is attached to the shaker. This is further explained in Chapter 4.

As mentioned above, the quick mount cantilevers from Piezo Systems Inc. comes with a bleeding SMD resistor. This is shown in a close up picture in the following figure.

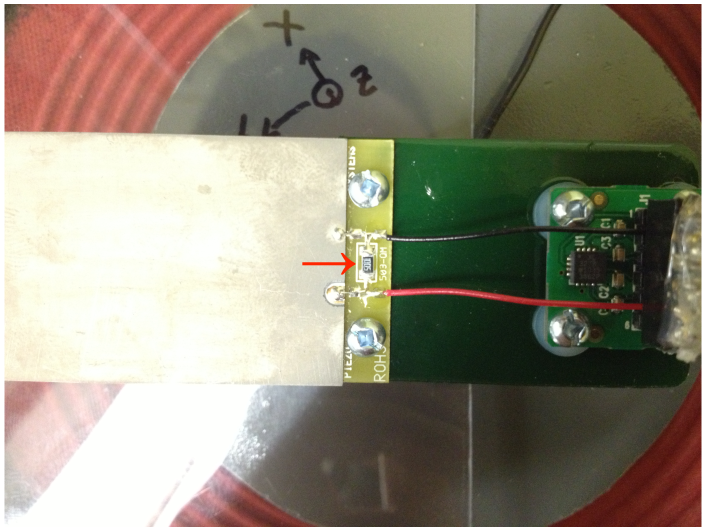

Figure 3.4: The piezoelectric bimorph cantilever as seen from the top showing the bleeding resistor.

Notice that Fig. 3.3 and Fig. 3.4 show two different mounting devices (grey and green respectively). This will be explained further in Section 4.5.

Next, the following image is of the cross-section of a bimorph cantilever[4] obtained using an Olympus BX51 microscope. The image shows scratches predominately on the bottom right. These scratches were created during the manufacturing process either while cutting the material or polishing it. They are insignificant and should not cause any errors in the analysis. Also visible on the right edge are small imperfections making the edge not as sharply defined. Since the total thickness was measured with digital venire callipers using average values, these edge imperfections are averaged out. Thus any error associated with imperfections can safely be ignored, and the lever assumed to be ideal.

[4] This image is not of the actual bimorph as studied in this section or in the Experimental Chapter 4. However, this lever is very similar in construction and the cross-sectional area is nearly identical.

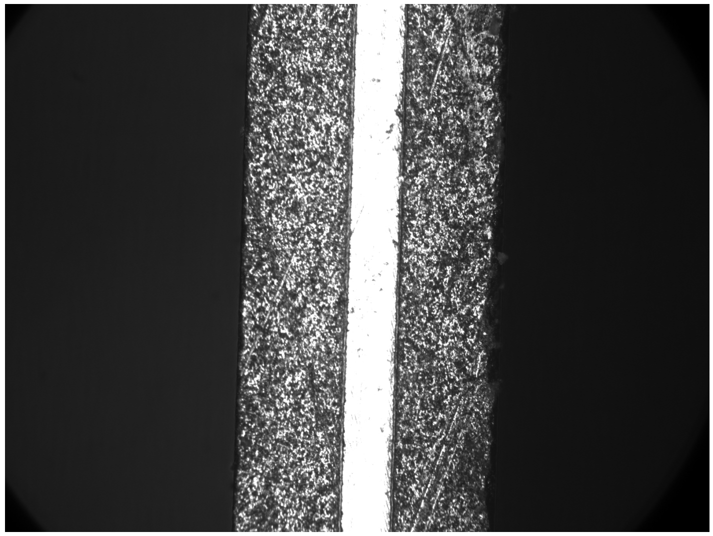

Figure 3.5: Cross-section of a piezoelectric bimorph cantilever. Using the Olympus BX51 microscope, the shim thickness was measured with the scaling on the eyepiece of the microscope (not shown in picture) to have an average value of 0.166 mm thick.

Lastly, the Table 3.6 summarizes the various parameters used to describe the piezoelectric bimorph cantilever. Note that lengths, widths, and total thickness were determined by averaging over several measured values using digital venire callipers with an accuracy of 0.02 mm. If both measured and published values are available, the measured ones are used in any analyses.

Table 3.6: PROPERTIES OF THE BIMORPH CANTILEVER

Q 2 20 -A4 -503 Y				
Description	Symbol/ Unit	Measured/ Calculated	Published	Ref.
Elastic modulus piezoelectric	$Y_p\,[GPa]$	–	66	[12]
Elastic modulus substrate	$Y_s\,[GPa]$	–	105	[12]
Piezoelectric coupling	$d_{31}\,[pm/V]$	–	-190	[12]
Electrical permittivity	$\epsilon\,[\mu F/m]$	–	15.98	[4]
Damping ratios	ζ_1	(2.8 ± 0.6) %	–	–
(See Section 3.4.2)	ζ_2	(2.0 ± 0.6) %	–	–
Mass (without mount)[a]	$M\,[g]$	–	8.0	[4]
Density piezoelectric	$\rho_p\,[kg/m^3]$	–	7800	[12]
Density substrate	$\rho_s\,[kg/m^3]$	–	9000	[12]
Length (unmounted)	$l\,[mm]$	63.7	63.5	[4]
Length (mounted)[b]	$l\,[mm]$	57.3	57.2	[4]
Width	$w\,[mm]$	31.8	31.8	[4]
Total thickness	$h\,[mm]$	0.52	0.51	[4]
Piezoelectric thickness [c]	$h_p\,[mm]$	0.19	–	[4]
Substrate thickness[c]	$h_s\,[mm]$	–	0.14	[12]

Several important notes as marked in the table are in order:

- Note a: Since the cantilever came with an attached quick mount and the exact mass of it is unspecified, hence it was impossible to calculate the densities.
- Note b: The effective length of the bending portion of the lever is between 57.3 and 63.7 mm, and it is impossible to determine the exact length. This is discussed in detail below.
- Note c: A company representative of Piezo Systems Inc. claimed that the brass shim has the same thickness for all cantilever types they manufacture.

However, the published value of the thickness is 0.14 mm [12] while the measured thickness with the microscope as seen in Fig. 3.5 is 0.166 mm, albeit that measurement is for a slightly different cantilever. The published value is chosen to be more accurate. Hence, it is possible to calculate the piezoelectric thickness by

$$\begin{aligned} h_p &= \frac{h\,(\text{as measured}) - h_s\,(\text{from Ref. [12]})}{2} \\ &= 0.19\,mm\,(\text{as shown in Table 3.6}) \end{aligned}$$

Due to the mount as manufactured by Piezo Systems Inc. the bimorph cantilever does not have a well-defined length but only an effective length. The overlap of the PZT layer with the yellow plastic mount (as seen in Fig. 3.3) ranges between 57.3 mm to 63.7 mm and thus has a parametric range of 6.4 mm. Therefore, depending on the input vibrations, the effective length can take on any value between the specified range. This effective length is likely a consequence of the way the two materials are glued together and their combined stiffness. Different input vibrations may change the effective length. Due to the several unknown factors of this construction it is not possible to incorporate this phenomena into the MatLab script that was developed. However, it is possible to adjust the simulations accordingly by tuning or calibrating the code.

The manner in which the code was tuned is as follows. If one has access to either literature data of the location of the first mode of vibration or experimental data of the actual piezoelectric cantilever, then by adjusting the effective length within the code within the specified range one can overlap the first mode of vibration. Of course if the first mode of vibration cannot be overlapped in the simulation results with the experimental/literature results within the specified range, then there may be another issue such as for example incorrect measurements of the physical parameters. Once the code is tuned to the experimental first mode the effective length of the cantilever is set. It should be noted, however, that the effective length may change if the amplitude of the input vibrations is changed and should be re-calibrated if these conditions change.

3.4.2 Damping of the Cantilever

This subsection is in part theoretical but also contains some experimental results. However, to keep the flow and organization, results are presented here as opposed to in the experimental chapter.

A cantilever in motion is subjected to frictional forces. The piezoelectric cantilever of the kind studied has two frictional forces. The internal stiffness of the lever causes friction and hence damping of the system. The stiffer the lever the more highly damped it is and therefore a greater strain has to be applied to displace the lever by the same amount as compared to a lesser stiff lever. Furthermore the external air resistance causes the system to be damped as well. Recall in Section 2.1 the total damping, which was assumed to proportional damping, was of the form

$$D_{\text{diag}} = \alpha_0(M_{s,\,\text{diag}} + M_{p,\,\text{diag}}) + \alpha_1(K_{s,\,\text{diag}} + K_{p,\,\text{diag}}). \tag{3.4.1}$$

The proportional constants α_0 and α_1 are related to the damping ratios as in (3.3.1), namely,

$$\zeta_r = \alpha_0\left(\frac{1}{2\omega_r}\right) + \alpha_1\left(\frac{\omega_r}{2}\right) \tag{3.4.2}$$

where the ω_r are the undamped natural frequencies [10, 12, 7], given by

$$\omega_r = \frac{\lambda_n^2}{2}\left(\frac{YI}{ml^4}\right)^{1/2}. \tag{3.4.3}$$

The λ_n values are found by numerically solving

$$1 + \cosh(\lambda)\cos(\lambda) + \frac{\lambda M_{tip}}{mL}(\cos(\lambda)\sinh(\lambda) - \sin(\lambda)\cosh(\lambda)) = 0 \tag{3.4.4}$$

Here m is the mass density of the combined lever (without tip mass M_{tip}), while YI is the bending stiffness [10, 12, 22]. The bending stiffness is given by

$$YI = \int_{-(h_s/2+h_p)}^{h_s/2+h_p}\int_{-w/2}^{w/2} z^2 Y^E(z)\,dy\,dz \tag{3.4.5}$$

with

$$Y^E(z) = \begin{cases} Y_p & \text{when } -(h_s/2 + h_p) \le z \le -h_s/2 \\ Y_s & \text{when } -h_s/2 < z < h_s/2 \\ Y_p & \text{when } h_s/2 \le z \le h_s/2 + h_p \end{cases}$$

being the piecewise function defining Young's constant for the bimorph geometry as in Fig. 2.1.

Solving the system of linear equations in (3.4.2) for $r = 1$ and $r = 2$ gives the expressions for the damping constants as

$$\alpha_0 = \left(\zeta_2 - \zeta_1 \frac{\omega_2}{\omega_1}\right) \left(\frac{1}{2\omega_2} - \frac{\omega_2}{2\omega_1^2}\right)^{-1}, \tag{3.4.6}$$

$$\alpha_1 = \left(\zeta_2 - \zeta_1 \frac{\omega_1}{\omega_2}\right) \left(\frac{\omega_2}{2} - \frac{\omega_1^2}{2\omega_2}\right)^{-1}. \tag{3.4.7}$$

Thus if the damping ratios ζ_1 and ζ_2 are found experimentally then with these equations the proportionality constants α_0 and α_1 can be obtained.

For the bimorph cantilever as outlined in Table 3.6 of Section 3.4.1 the damping ratios were found experimentally using logarithmic decrement [7]. The ratio of two successive amplitudes in a damped system can be used to calculate the damping ratios as follows. The logarithmic decrement is given by

$$\delta = \ln\left(\frac{x(t)}{x(t+T)}\right), \tag{3.4.8}$$

where $x(t)$ is the measured amplitude and is periodic with period T. The decrement δ is then used in

$$\zeta = \frac{\delta}{(4\pi^2 + \delta^2)^{1/2}}, \tag{3.4.9}$$

to calculate the various damping ratios.

To measure the first damping ratio the piezoelectric cantilever was excited with base vibrations at the first resonance frequency with a resistor as the load. While an oscilloscope was connected to measure the voltage output over the load. When the input was stopped the oscilloscope screen was quickly captured and the data exported to MatLab. The following figure shows the voltage output obtained with an oscilloscope over the load resistor.

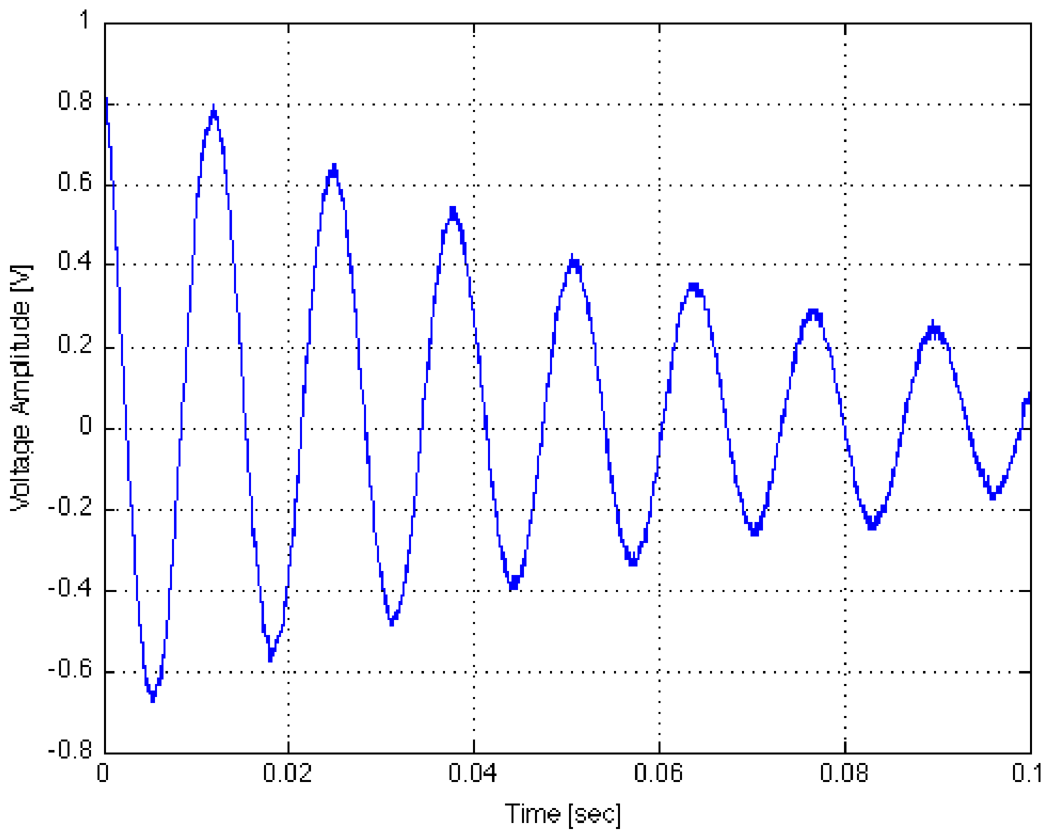

Figure 3.6: Successive damped oscillation amplitudes of excited piezoelectric cantilever. No higher harmonics are significantly present, hence this is a good data set for logarithmic decrement measurements.

This image shows that each successive amplitude is smaller and that the decay follows an exponential envelope. The actual value of the amplitude is irrelevant and only the successive ratios of amplitudes that is of importance. The exact peak values were measured with the oscilloscope. However, quite often when shutting off the input base acceleration higher harmonics were present. This could be due to the sudden jerk in motion when stopping the input. Such a case is shown in the following image.

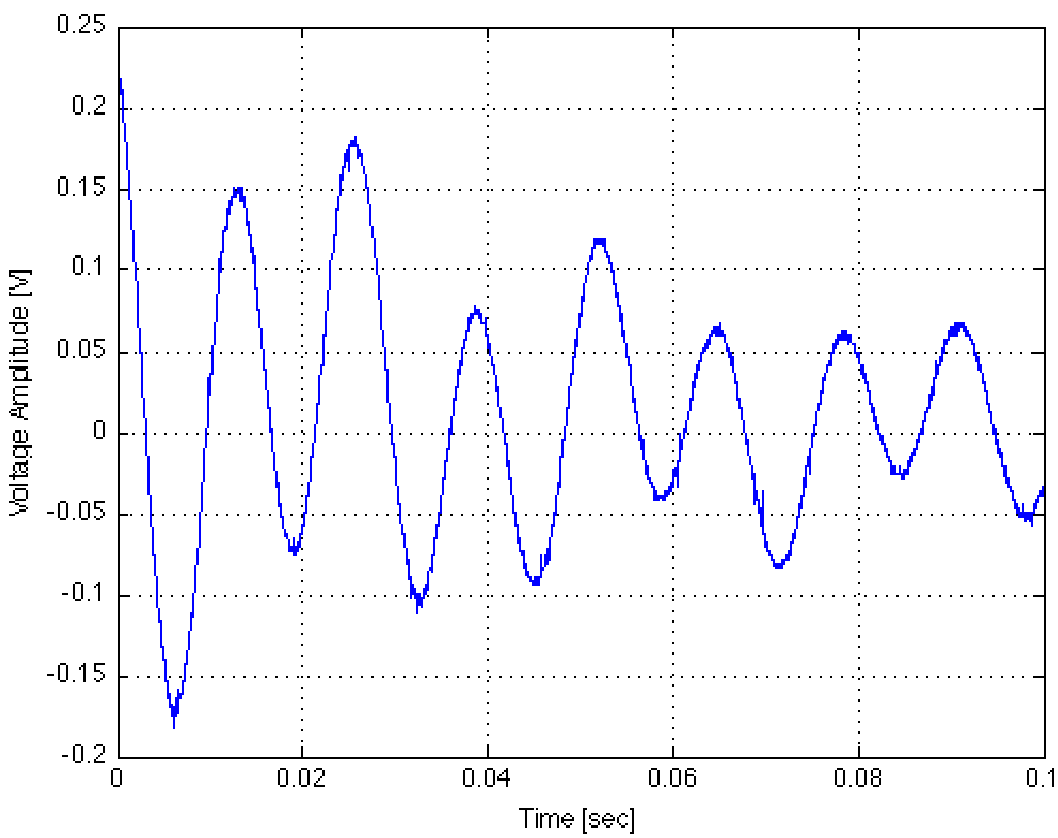

Figure 3.7: Successive damped oscillation amplitudes of excited piezoelectric cantilever. Higher harmonics are significantly present hence this is not a good data set for logarithmic decrement measurements.

It is clear from this image that logarithmic decrement cannot be applied and such situations were not used in the averaging procedure. In total 115 amplitude ratios from good decays such as in Fig. 3.6 were gathered and averaged. To measure the second damping ratio this procedure was repeated in a similar fashion as the for the first damping ratio with the exception that the lever was excited with base vibrations tuned to the second resonance frequency. Since the higher the frequency the more energy is put into the cantilever system and so the chances of harmonics in the decay such as in Fig. 3.7 becomes more common. Therefore, the second resonance mode was more difficult to obtain good decaying results, only 44 amplitude ratios were gathered and used to average the results. The averaged damping ratios were measured to be

$$\zeta_1 = (2.8 \pm 0.6)\% \tag{3.4.10}$$

$$\zeta_2 = (2.0 \pm 0.6)\% \tag{3.4.11}$$

In the bimorph case study of Section 3.3 a very similar piezoelectric cantilever compared to the one presented here was used. The authors of the original study presented their experimentally measured first damping ratio to be $\zeta_1 = 2.7\%$ [12]. This gives confidence in the damping ratios as was measured as the agreement is quite good.

Finally, it should be noted that the damping ratios do not significantly effect the location of the resonance frequencies but mostly only their amplitudes. Since the usage of the MatLab script solving the equations of motions for the piezoelectric cantilever is mostly to locate the resonance frequencies and not so much predict the amplitude output, the accuracy of the damping ratios is not very important. This was tested by using the Matlab script to calculate the first two mode locations and amplitudes given the four extreme values of the damping ratios given their plus/minus values (i.e. $\zeta_1 = 2.2\%$ and $\zeta_2 = 1.4\%$, $\zeta_1 = 2.2\%$ and $\zeta_2 = 2.6\%$, $\zeta_1 = 3.4\%$ and $\zeta_2 = 1.4\%$, $\zeta_1 = 3.4\%$ and $\zeta_2 = 2.6\%$). This is summarized in the following table with the resistive load $R_{\text{load}} = 9920\,\Omega$ and no tip mass.

Table 3.7: RANGE OF DAMPING RATIOS TO TEST EFFECTIVENESS

Damping ratios	Resonance frequencies	Amplitudes
$\zeta_1 = 2.2\%$	$f_1 = 75.647$ Hz	0.8333 V
$\zeta_2 = 1.4\%$	$f_2 = 477.583$ Hz	0.2257 V
$\zeta_1 = 2.2\%$	$f_1 = 75.647$ Hz	0.8333 V
$\zeta_2 = 2.6\%$	$f_2 = 477.168$ Hz	0.1421 V
$\zeta_1 = 3.4\%$	$f_1 = 75.650$ Hz	0.6103 V
$\zeta_2 = 1.4\%$	$f_2 = 477.583$ Hz	0.2258 V
$\zeta_1 = 3.4\%$	$f_1 = 75.650$ Hz	0.6102 V
$\zeta_2 = 2.6\%$	$f_2 = 477.168$ Hz	0.1421 V

The data in the table clearly shows that changing either or both of the damping ratios does not significantly effect the location of either the first or second mode of vibration and only changes the respective amplitudes. Further each vibration mode corresponds directly to the respective damping ratio. In other words, changing the first damping ratio only changes the amplitude of the first resonance mode.

These results are consistent with circuit theory regarding RLC circuits. In an RLC circuit the resonance is given by

$$f_{\text{res}} = \frac{1}{2\pi}\frac{1}{\sqrt{LC}} \tag{3.4.12}$$

that does not depend on the resistance R. However, the resistance does partly determine the voltage output taken anywhere on the RLC branch.

Therefore, given these findings, if one is only interested in locating the resonance modes the damping ratios do not play a significant role. The following subsection outlines how the piezoelectric bimorph cantilever was tuned to a particular frequency using the MatLab script.

3.4.3 Tuning of Cantilever

The purpose of tuning the piezoelectric bimorph cantilever is to harvest the most amount of power possible from a vibrating source. For the experimentation chapter, the vibration sources of interest are typically vibrating at 120 Hz. Therefore, adjustments must be made in order to reach that frequency.

There are two factors that effect the vibration modes of the lever that should be considered. The first is due to the construction of the mount on the bimorph cantilever. The yellow mount, as seen in Fig. 3.3, changes the actual piezoelectric lever length to an effective lever length. By this it is meant that there is not a definite lever length as different input vibrations can result the lever to bend differently in the area of the yellow mount. Therefore, although the actual length[5] of the piezoelectric material of cantilever is 63.5 mm, the mount width which is 12.5 mm can effect the output of the cantilever such that the effective length of the lever can be anything in between the overlap of the piezoelectric material and the yellow mount. Thus the effective length is between 57.3 mm to 63.7 mm.

As was found with experimental work while getting familiar with the set up and the properties of the cantilever, the effective length of the lever changes given different vibration inputs. The way to overcome this problem is to adjust the effective length in the MatLab script such that the first predicted vibration mode matches with experimental measurements. Once the MatLab script is tuned, the various information can be extracted from it.

The second factor that effects the vibrations modes is the impedance of the attached load. Of course this makes sense when considering the RLC circuit such as in Fig. 2.3. Depending on the load's properties the vibration modes may change within a range of a few hertz. Therefore, when trying to tune the lever to, say, 120 Hz, it is not practical to assume a certain load condition.

In other words, the cantilever, without tip mass is in the range of mid-70's Hz depending on the load. However, the lever should be tuned to 120 Hz for applications as will be shown in Chapter 4. Therefore, the MatLab script can be

[5] This measurement is provided by the manufacturer [4].

used to calculate how much of the lever's length should be cut-off in order to raise the fundamental resonance frequency. However, the two factors as discussed may change the frequency and so it is impossible to cut the lever such that it will always be tuned to 120 Hz.

To overcome this problem the code was used to calculate how much to cut off the lever and to overshot 120 Hz, say around 130 Hz. Then a proof mass can be used to fine tune the lever depending on the conditions of the two factors as discussed. The code was also used to predict roughly where the proof mass mount should be placed along the lever in order to fine tune it.

More precisely, with the MatLab script, it was calculated that if 13 mm were to be cut off, then the first mode of resonance would be roughly 120.9 Hz with a $1000\,\Omega$ load resistor without a proof mass. If a proof mass[6] of 2.26 grams were to be attached at the tip then the first resonance frequency would drop to 75.8 Hz. However, with a cut-off of 13 mm the range of tune-ability is too small and ideally should be a bit higher.

If a proof mass is added then the deflection of the cantilever is greater and in turn produces a stronger electric dipole moment across the terminals. Yet if the 2.26 grams proof mass were to be used then a total of 23.68 mm would have to be cut off in order to tune the lever to 120 Hz. Cutting off so much piezoelectric material is not practical, as the less piezoelectric material, the smaller of a current can be drawn. Therefore, a balance between cutting off the lever and using the proof masses should be found.

It was calculated that is 15 mm were cut off and the 2.26 grams proof mass was used then the lever could be tuned to 120 Hz, provided that the masses are located at about the half way point along the lever. This is quite practical as any fine tuning required due to changes in the load impedance can easily be done by sliding the

[6]Neodymium rare Earth magnets are used for the proof mass. These make it easy to adjust the location of the along the lever where the masses are attached. Further they are not damaging to the cantilever itself and hold tightly onto the lever due to mutual magnetic attraction. Two of these magnets, one on top and the other on the bottom, weight 2.26 grams. Any number of magnets can be added each with a weight of 1.13 grams.

masses up or down along the lever's length. Furthermore, 15 mm seems to be the least amount of material that needs to be cut off that still provides a large range in tune-ability.

Therefore, given these lines of argument and analyses with the MatLab code, it was decided to cut off 15 mm from the piezoelectric bimorph cantilever and use to proof mass as indicated. Hence the length as described in Table 3.7 should be updated to subtract 15 mm.

3.5 Chapter Contributions

This chapter investigated the simulation aspect of analyzing piezoelectric cantilevers. The purpose of this chapter was twofold. First purpose was to test the equations as coded in a MatLab script and verify the accuracy of the script. This was done by studying two case studies found in literature. The first case study was of a unimorph cantilever. Studying this case helped underline the importance of accuracy and the equivalent modes needed to obtain a desired accuracy. The second case study was of a bimorph cantilever that was similar to the actual lever used in the experimental section. The results of studying these case studies is that the MatLab script is determined to be accurate and can be used to predict the equivalent circuit components.

The second purpose of this chapter was to introduce and study the actual cantilever that will be used in the experimental chapter. In order to study the bimorph cantilever some side steps had to be taken such as the determining the damping ratios and tuning the cantilever. It is not practical to derive, using the MatLab script, the equivalent circuit components in this chapter as the load impedance as well as the proof mass will change these values. Hence these will be calculated in the experimental section as appropriate for the set-up.

The two most important features of simulating the cantilever, as outlined in this chapter, were as follows. The first and most important is the use of multiple equivalent circuit modes. It is not enough to use a single equivalent mode in order to predict the first resonance frequency. Ideally about four equivalent modes should be taken into consideration when interested in the first and second resonance frequencies. Furthermore, if one is purely interested in the first mode of vibration, one can use a large number of equivalent modes, but then only use the first mode values, such as was done in the bimorph cantilever case study by Kong. et al.

The other important features that was studied in this chapter was the damping ratios. First the theory was set up and then experimental measurements were taken. It was determined that the damping ratios only have an effect on the respective amplitudes but do not significantly effect location of the modes. Due to the relatively large error during the experimental procedure, the range of the damping ratios is too large to accurately predict the amplitudes as well as the location of the resonance modes. Further, the experimental set-up of the shaker used to input the base vibrations into the system causes some issues that were not outlined here, but will be explained in more detail in Section 4.1.

Chapter 4

Experimentation

The purpose of this chapter is to examine the feasibility of vibrational energy harvesting with real-world applications. There has been much work done on designing harvester units via simulations and idealized laboratory settings, however little attention has been devoted to realistic applications. As discussed in Section 1.5, the PM circuits, albeit quite efficient, are complicated and consist of several components. The strategy in this chapter is to test a PM circuit which is as simple as possible, and albeit its efficiency is much lower than modern PM circuits as proposed in literature, is still able to convert enough energy into a useable form.

Not only is the proposed PM circuit simpler, the input vibrations are also not ideal and, as will be demonstrated, contain many significant harmonics. As nearly no real-world application produces perfect sinusoidal vibrations without any harmonics present, it is important to study these harmonics and whether their presence has any significant effect on vibrational energy harvesting. The two main real-world applications are a large transformer and several industrial fans.

This chapter is not to argue against efficient PM circuit designs, but the main goal is to demonstrate vibrational energy harvesting is possible in a sufficient manner for applications such as WSNs with simplicity as a design feature. Further still, as discussed in Section 4.1, the experimental setup to test and tune the energy harvester is very basic and costs a fraction of the price compared to normal shaker table setups usually used in literature. Lastly, a particular experiment is presented that highlights a discrepancy between simulation and experimental results for higher modes of vibrations. This higher mode discrepancy could be a limitation of the equations derived in Chapter 2 for a piezoelectric cantilever of the bimorph geometry. A discussion follows with possible solutions to correct the discrepancy.

The outline of this chapter is as follows. The preceding section presents the experimental setup that includes a cost efficient custom-made shaker setup. Section 4.2 proposes the harvester unit that is to be used in the experimental work. The harvester unit consists of the piezoelectric cantilever as outlined in Section 3.4 and the PM circuit. The cantilever is also tuned using the custom shaker setup to prepare for the experiments.

Next the real-world applications are presented. First in Section 4.3 experiments are conducted on a transformer that feeds a university laboratory. Second in Section 4.4 experiments on different industrial fans are performed. Each experiment is over a duration of 24 hours. The chapter then concludes with results obtained and contributions.

Finally, Section 4.5 is a demonstration experiment that shows the compatibility of the MatLab script as was presented in the previous chapter with a slightly modified harvester unit. This section is important as it outlines some limitations of the code as mentioned.

4.1 Experimental Setup

The most important piece of equipment for a vibrational energy harvesting laboratory setup is the vibration shaker. Normal vibration shakers[1] are rather

[1]Dalimar Instruments Inc. quoted a miniature shaker (model number: K2007E1) with integrated amplifier with BNC input, 31 N (7 lbf) pk sine force, 13 mm (0.5") pk-pk stroke to be $6209.00 CAD or $4657.00 CAD with a university discount.

expensive and can cost several thousand dollars for even a small desktop unit. Due to this it was decided to build a simple custom shaker for the purpose of testing and tuning of the piezoelectric bimorph cantilever. The following image is of the finished speaker shaker.

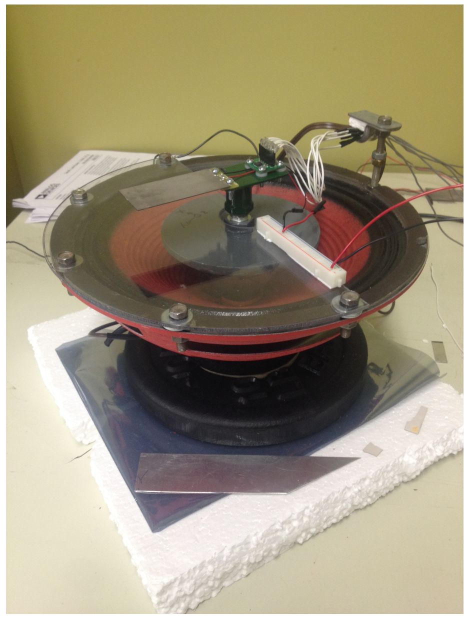

Figure 4.1: Custom shaker setup made from speaker.

The shaker is made from an old 10 inch, 25 Watt, 8 Ohms, 50-18000 CPS (cycles per second) Le Cavalier speaker by Marsland in Waterloo, Canada. This unit was found in recycling at the University of Winnipeg and had no initial costs. The unit was then prepared with a 15 lbs weight attached to the bottom with an epoxy. This extra weight was to increase the stability of the speaker by lowering its center of gravity and also to help absorb any small harmonics that may travel through the shaker setup.

The cone of the speaker was covered and glued with a grey wooden disk to serve as the base on which the mounting devices are attached. On the center of the base plate a threaded copper tubing was glued that allowed for the attachment of the mount (green as seen in Fig. 4.1). The rear of the speaker was fitted with a support for the various cables that were attached to the setup. This was done in order to reduce any tension in the cables which may pull the mount and base plate away from its natural equilibrium position.

Finally a plastic shield was attached over half of the speaker's open surface, to protect the piezoelectric cantilever from air disturbances caused while the speaker is active. Although the air pressure waves caused by the active speaker are minimal and only noticeable by hand when the frequency and amplitude are high, these waves would cause interference with the way the cantilever vibrates. Without the protective covering the cantilever would have to be treated to have two forcing functions as an input as opposed to a single base acceleration input.

The total cost of preparing this shaker setup was well below $100 CAD which is less than 1.4% the cost of a professional miniature shaker[2]. The entire shaker setup was placed on a 1.5 inch thick styrofoam slab to absorb any other vibrations entering the system externally. The system was also levelled to allow the disk plate with the mount and cantilever to shake freely in z-direction (up and down) with minimal sideways motion.

To ensure that the shaker was performing as desired and to also measure the input base vibrations (the forcing function), a tri-axial accelerometer unit was also attached on the mount next to the base of the cantilever. The accelerometer can be seen in either Fig. 3.3 or Fig. 3.4. The sensitivity, or gain, of the accelerometer is 420 mV/g and was purchased from Digi-Key Cooperation[3].

[2]Custom shaker < $100, Dalimar shaker = $6209 + 13% tax. Therefore, custom shaker < 1.4% Dalimar shaker.

[3]A single-axis 1200 mV/g MMA1260EG accelerometer was used to test the endurance of accelerometers. The accelerometer was connected to the shaker system and observed with the oscilloscope. First strong neodymium rare Earth magnets were held close to the accelerometer but no oscilloscope changes were noticed. The accelerometer is not magnetic and so magnets do not cause an interference as was evident. This was important to establish as the proof mass used to tune the lever was small disk neodymium magnets. Secondly, an old piezoelectric ignitor was used to create high voltage shocks to test the sensitivity. After a few shocks to the accelerometer was damaged and the oscilloscope measurements flatlined. Based on this it was decided to ground the speaker shaker in order to prevent any static build up that may damage the tri-axial accelerometer.

No amplification system was required to drive the speaker and an Agilent 33522A, 2-channel, 250 MSa/s, 30 MHz function/arbitrary waveform generator was attached directly to the speaker to drive the base acceleration. Measuring equipment used throughout experimentation process included a Tektronix four channel 200 MHz oscilloscope, an Agilent 34461A 6 1/2 digit digital multimeter (DMM) and an Agilent 34410A 6 1/2 DMM. The DMMs were used to collect current and voltage data that was exported with the Agilent Connectivity Utility software to a laptop.

4.2 Harvester Unit Description

The harvester unit is an entire module used for measuring vibrations and collecting energy via vibrational energy conversion. The unit consists of an accelerometer, the piezoelectric bimorph cantilever (with a proof mass for fine tuning), the PM circuit, and a housing to contain all the parts and allow for attachment to vibrational sources. Figure 4.2 shows the harvester unit used in the experiments as outlined in this chapter.

The housing of the harvester unit is made of aluminium and is therefore not magnetic. Since the applications for the harvester unit, i.e. the sources of vibration, by coincidence all have ferromagnetic properties, a strong square magnet is used to firmly attach the harvester unit to the vibration sources. The magnet cannot be seen in the figure as it is in the compartment below the accelerometer. This method of attachment makes it possible to firmly secure the harvester unit to ferromagnetic metals either on the back side of the unit of the bottom (both of which are used in the experiments).

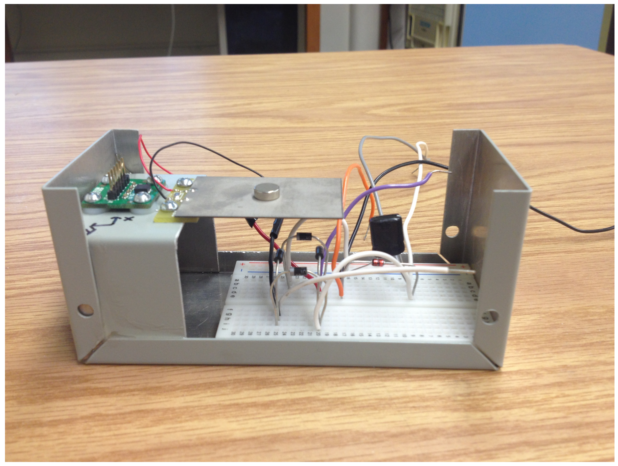

Figure 4.2: Harvester unit used in experiments. The unit consists of an accelerometer (left, on green chip), bimorph piezoelectric cantilever, proof mass (two neodymium magnets near the centre on the lever), and the PM circuit.

The accelerometer is a tri-axial EVAL-ADXL335Z purchased from Digi-Key cooperation with a sensitivity of 420 mV/g. Although the only axis useful for energy harvesting is the z-axis (up and down base motion), a tri-axial accelerometer was chosen in order to study the other axes as well. Due to the construction of the bimorph cantilever, the x- and y-axis vibrations do not contribute significantly to the dipole displacement of the PZT material (see Section 1.2). However, for investigation purposes knowing the motion of a vibration source in all three directions can be of interest.

The PM circuit is assembled on a solderless breadboard that allows for the harvester unit to take on various different PM circuit designs. Several different PM designs were discussed in Section 1.5. The PM design chosen for the experiments is one of the most simplest. The terminals of the piezoelectric bimorph cantilever are attached to a full diode bridge. Schottky diodes are chosen as they have a very low forward voltage drop ideal for vibrational energy harvesting. Low quality silicon diodes can have forward voltage drops of up to 1

V whereas Schottky diodes typically range between 0.2 to 0.5 V. As the vibration sources may have low amplitudes and thus the piezoelectric element produces accordingly small voltages, Schottky diodes require less voltage to turn them on allowing for the next stage of the PM circuit.

After the bridge is the super-capacitor in parallel with a Zener diode. The Zener diode is to protect the super-capacitor from over-voltage. Due to higher capacitance rating on the super-capacitor (1 F) and the small size of the element, the voltage rating is fairly low (2.5 V). It is unlikely that the voltage after the bridge is ever larger than 2.5 V, and so the Zener diode is in place just in case it does happen. The super-capacitor is a radial electric double-layer, 1 F, 2.5 V lead free capacitor with a tolerance of -20% and +80%. With such high tolerances, the capacitor was tested for its true capacitance. The measurement was done with a LC103 capacitor and inductor analyzer by Sencore. After a series of measurements at room temperature the average capacitance was found to be 1.462 F. This measurement is only accurate at room temperate and may change depending on temperature as well as wear on the component.

Since the purpose of the experiments is to provide proof-of-concept for the design presented in this thesis, the manufacture rating of 1 F is continued to be used in the plots which will be shown in this chapter. The extra 46.2% in capacitance is considered to account for any sources of error or leakages in the experiments. Since any errors associated with the experiments are likely less than 46.2%, the actual charge collected is larger than what will be presented in the following experiments. Since the goal is demonstration of proof-of-concept and not extremely precise measurements, and underestimate of charge is acceptable.

The harvester unit is tuned initially to 120 Hz using the laboratory setup as discussed in Section 4.1. The particular frequency of 120 Hz is chosen due to the common nature of mechanical vibrational sources to vibrate with a harmonic, among many others sometimes, of 120 Hz. The cantilever is tuned by slightly adjusting the position of the two neodymium proof masses until, using a DDM, the peak frequency is located. Due to the electrical properties of the piezoelectric bimorph cantilever, the load attached, i.e. the PM circuit, will effect the location of the resonance points. Therefore, when tuning the cantilever with the proof mass, one cannot change the circuit design without having to re-tune the lever anew. However, for the purpose of the experiments in the proceeding sections, the same PM circuit design is used throughout and the lever does not have to be retuned. Other PM designs are briefly discussed in the thesis conclusion in Chapter 5.

4.3 Transformer Application

This section examines a transformer as an application for vibrational energy harvesting. The 75 kVA, 600 V, 3-phase transformer feeds a laboratory. As is common, large transformers tend to make a humming sound as their housing or casing vibrates at twice the electrical frequency. Thus the vibrations on the transformer have a fundamental frequency of 120 Hz. The following is a picture of the transformer. Attached to the right side is the harvester unit consisting of the piezoelectric bimorph cantilever tuned to 120 Hz and the PM circuit.

Figure 4.3: Transformer used for application in vibrational energy harvesting. Attached to the right side is the harvester unit.

The harvester unit was set up for two 24-hour experiments in order to collect as much charge on the 1 F super-capacitor as possible. Each experiment was done twice as shown in the following set of images with all the left images corresponding to the first 24-hour experiment and the right corresponding to the second 24-hour experiment. Figures 4.4 and 4.5 are set of images of the vibration in the z-direction taken at the start up of each experiment.

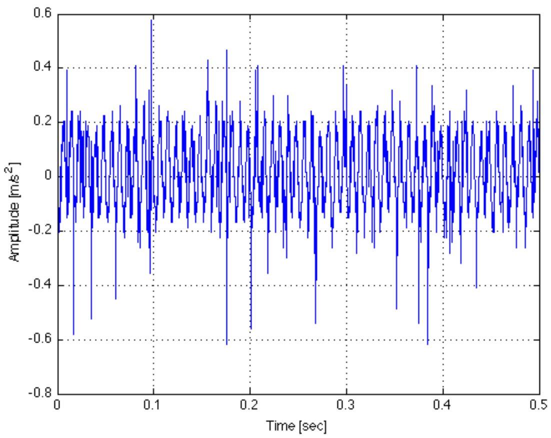

Figure 4.4: Z-axis vibration.

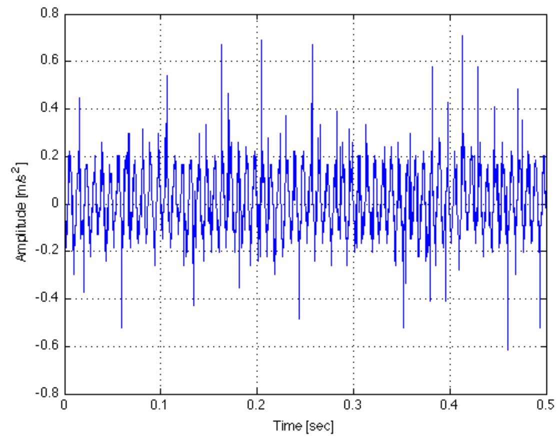

Figure 4.5: Z-axis vibration.

To get a better understanding of the harmonics contained in the vibrations the Fourier spectrum is produced in the following set of figures.

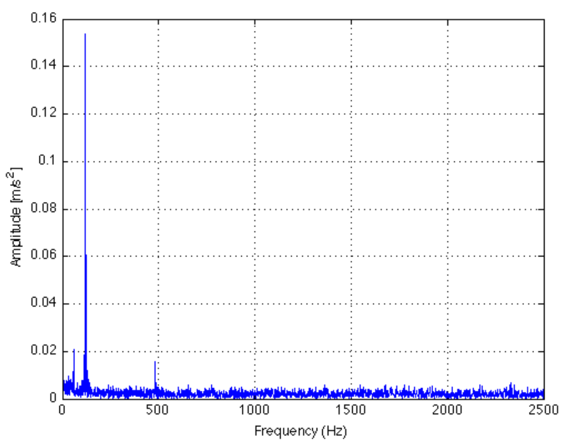

Figure 4.6: Fourier spectrum of input vibrations. $F_{\text{fund}} = 120\,Hz$ and $A_1 = 0.154\,m/s^2$.

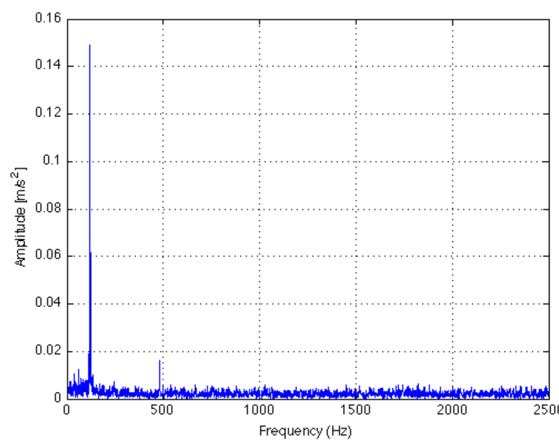

Figure 4.7: Fourier spectrum of input vibrations. $F_{\text{fund}} = 120\,Hz$ and $A_1 = 0.15\,m/s^2$.

The vibration measurements were taken one day apart, however, both are essentially the same. There is a strong fundamental component at 120 Hz with an amplitude of about 0.152 m/s^2. All other harmonics can be treated as such they are zero. Therefore, tuning the harvester unit to 120 Hz should harvest the maximum power available in the vibrational energy.

After running each experiment for 24 hours, the following data was collected. First is the voltage across the super-capacitor. This is shown in the following set of figures.

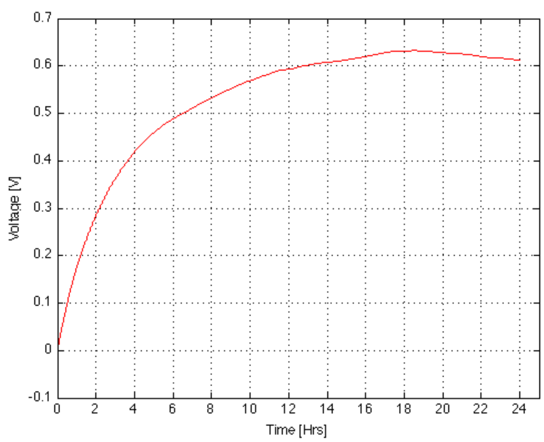

Figure 4.8: Voltage across the 1F super-capacitor.

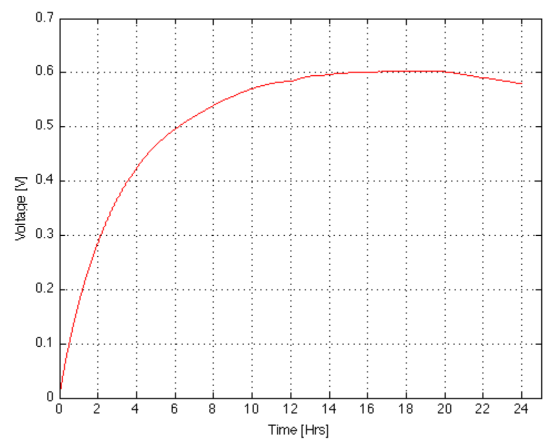

Figure 4.9: Voltage across the 1F super-capacitor.

The voltages build up exactly as expected. Namely a charging capacitor voltage plot. It is seen that after the 18^{th} hour in the first experiment and the 20^{th} hour of the second experiment that the voltage peaks and then drops slightly. It is not known why this drops happens. However, it is possible that the transformer vibrates with a smaller amplitude due to conditional load changes on the transformer's secondary side[4]. Figures 4.10 and 4.11 show the current going into the super-capacitor is shown.

[4] Since the harvest unit was unchanged for both experiments, the drop in voltage must be due to external parameter changes. It could be that the temperature in the room drops at night causing a change in capacitance and hence the voltage drop as seen in the figures.

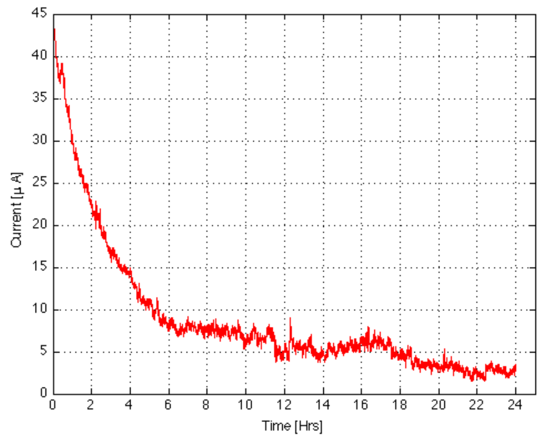

Figure 4.10: Current entering the super-capacitor.

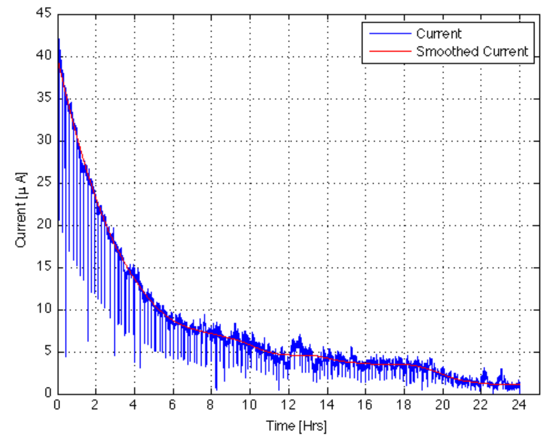

Figure 4.11: Current entering the super-capacitor.

Similar to the voltage plots, the current plots show expected behaviour, namely that of exponential decay as the super-capacitor charges. Note that the Agilent DMM measured some noise in the second experiment. This was smoothed out with a smoothing function in MatLab as shown in the plot. With simple Coulomb counting, it was determined that the total charge that went into the super-capacitor for the first experiment was Q = 0.768178 C while the second experiment produced Q = 0.695519 C of charge. Therefore, the average charge collected in the super-capacitor is Q = 0.695519 C. Note however, that these measurements do not include any leakage current in the Coulomb count that was done. Therefore, the actual charge might be slightly less. Further it was assumed that the rating of the super-capacitor, namely 1 F, is fairly accurate. However, this is known not the be entirely true as the super-capacitor's capacitance depends partly on the external temperature.

On the same note as the current plots, it is also of interest to see the power flow into the super-capacitor. This is shown the following in Figures 4.12 and 4.13.

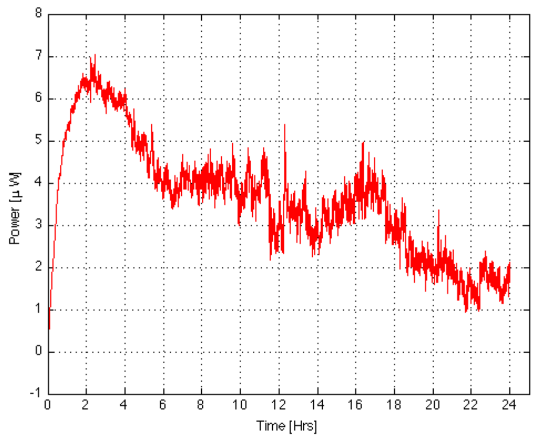

Figure 4.12: Power flow into the super-capacitor.

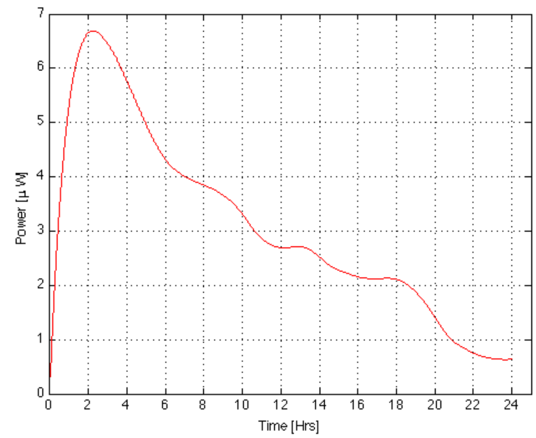

Figure 4.13: Power flow into the super-capacitor.

Both power plots indicate that the peak power flow occurred after about two hours of charging the super-capacitor. Note that the second power plot is much smoother due to the current smoothing earlier. These plots are consistent with the exponential behaviour of both the voltage and current plots.

Finally of most interest is the energy available for applications such as WSNs as discussed in Section 1.4. The energy plots are shown in Figures 4.14 and 4.14.

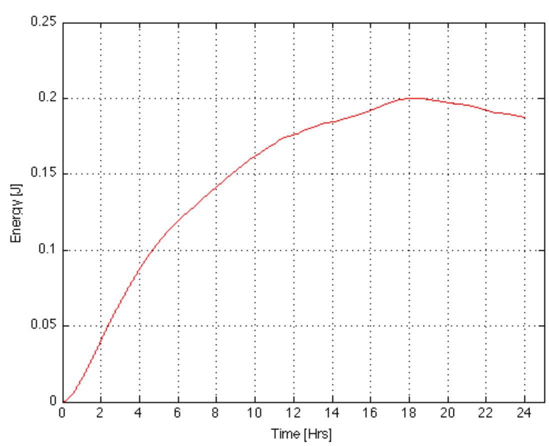

Figure 4.14: Energy available on the super-capacitor.

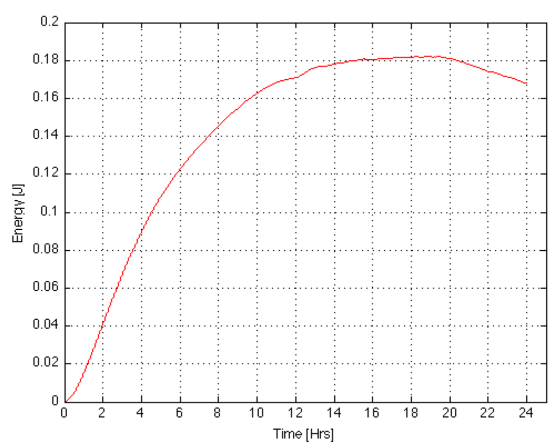

Figure 4.15: Energy available on the super-capacitor.

From these plots it can be seen that in the first experiment the peak energy available is 0.2 J while in the second experiment 0.18 J of energy are available. Thus roughly an average of 0.19 J of energy are available during the peak. If the application of this energy harvester unit is for WSNs then their operation can be made such that the radio IC turns on during the peak energy times every 24 hours. If the radio IC is on peak demand for 15 minutes then there is about 211 μW of power available. As discussed in Section 1.4 this much power is reasonable for modern WSNs technology.

4.4 Industrial Fans Application

This section investigates industrial sized fans as a possible vibration source for energy harvesting. Two different fans are studied (fan # 13 and fan # 15) which is outlined in the following two subsections respectively. These fans are of the Nano-Systems Fabrications Laboratory of the University of Manitoba. Since these large sized fans are on at all times to pressurize and circulate the air for the class 10 cleanroom, they are ideal for vibrational energy harvesting. The third subsection investigates the same fans but the cantilever is positioned differently, making use of a different vibration axis. For the first two subsections each experiment was performed twice with each respective figure placed side-by-side.

4.4.1 Industrial Fan # 13

This fan was chosen among the many fans in that laboratory as it not only exhibits large vibrational amplitudes but also strong harmonic content. The following is an picture of the fan.

Figure 4.16: Industrial fan #13 used for application in vibrational energy harvesting.

The harvester unit was attached in the centre of the fan as the vibrations were measured to be quite large there. The following set of images show the vibration in the z-direction for the first and second experiment performed.

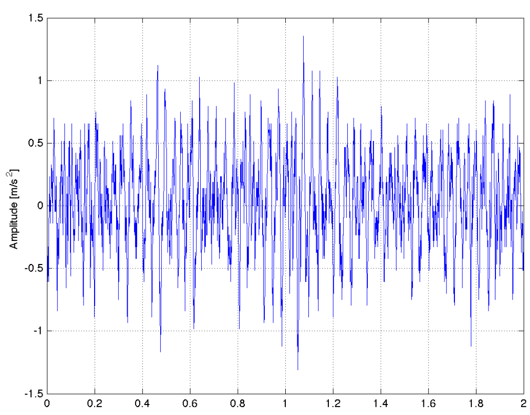

Figure 4.17: Z-axis vibration.

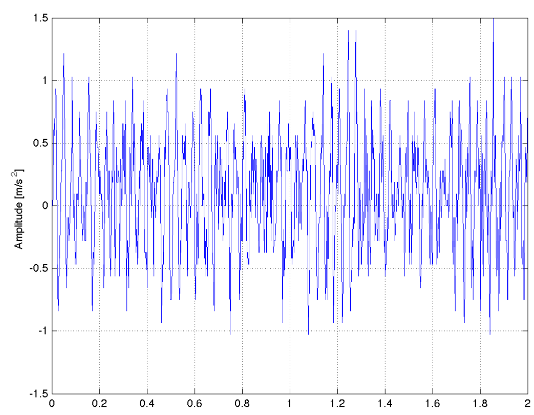

Figure 4.18: Z-axis vibration.

As can be seen, the amplitudes are up to three times as large as compared to the transformer accelerations in Figures 4.4 and 4.5. However, even though the amplitudes are larger, there are many more harmonics present. This is seen in the following set of figures.

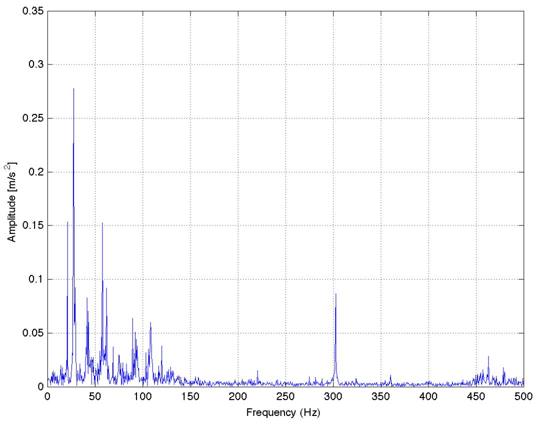

Figure 4.19: Fourier spectrum of input vibrations. $A_{120\text{ Hz}} = 0.0380\, m/s^2$.

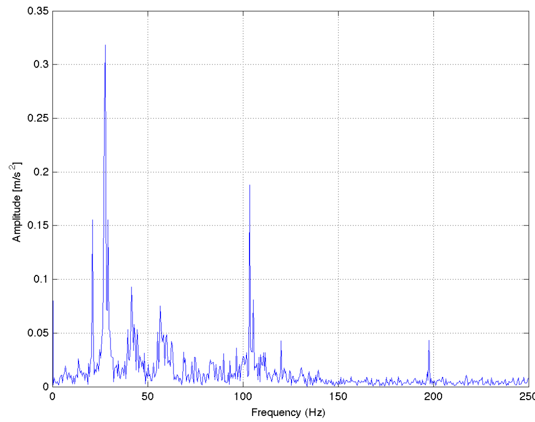

Figure 4.20: Fourier spectrum of input vibrations. $A_{120\text{ Hz}} = 0.0428\, m/s^2$.

The two successive Fourier spectrums show that there is a large number of harmonics present. There are many peaks of various harmonics. For example in Fig. 4.19 there is a large peak around 21 Hz with an amplitude of 0.1535 m/s^2. Another large peak around 28 Hz with an amplitude of 0.2777 m/s^2, and the largest peak at 41.5 Hz with an amplitude of 0.83 m/s^2. There is even a peak past the 120 Hz mark at 302.5 Hz with an amplitude of 0.0868 m/s^2, which is larger than the 120 Hz amplitude. Further, looking at the spectrums of both figures, there does not seem to be a fundamental frequency. Indeed these vibration signals are quite noisy and can hardly be considered periodic. However, as can be seen, there is indeed a 120 Hz component within the vibrational Fourier spectrum[5]. With such large and dominant harmonics it is expected that the voltage and current signal would to be quite distorted as well. Figures 4.21 and 4.22 show the voltages across the super-capacitor.

[5]One could in principle tune the cantilever to the frequency with the highest amplitude, which, in this case is around 41.5 Hz. However this requires either a very long cantilever or a large proof mass both of which are impractical. It was therefore decided to keep the tuning at 120 Hz throughout the experiments for simplicity and practicality.

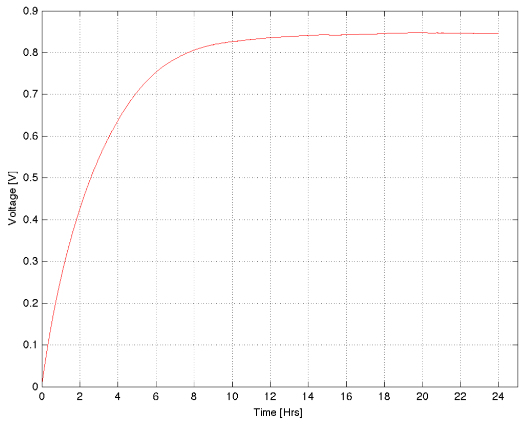

Figure 4.21: Voltage across the 1F super-capacitor.

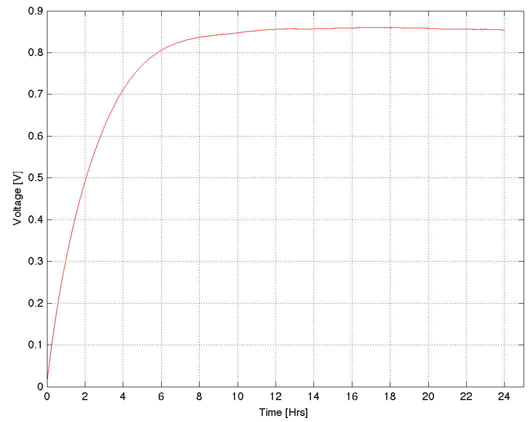

Figure 4.22: Voltage across the 1F super-capacitor.

Quite interestingly enough, about 0.85 V was built up over the capacitor in either 24 hour experiments. The plots follow the expected curve shape for a charging capacitor. However, no notable distortions are presents as was expected. This can be explained by looking at the following current plots.

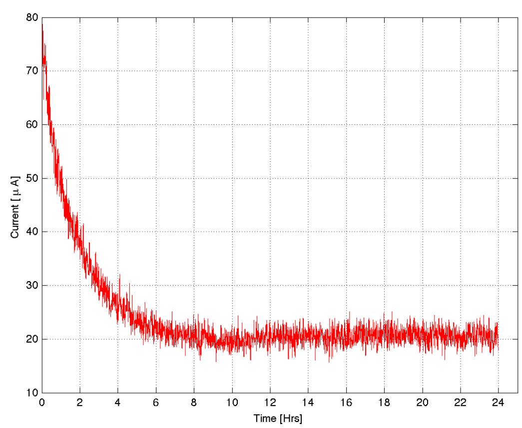

Figure 4.23: Current entering the super-capacitor.

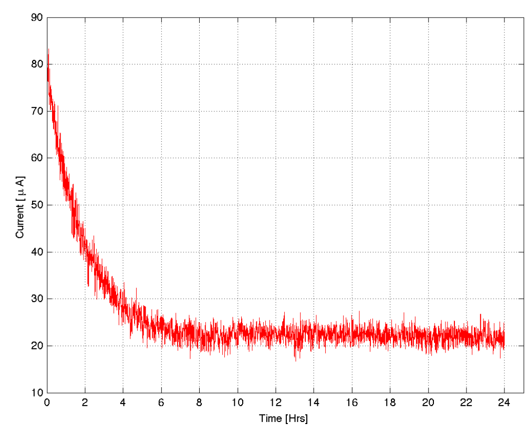

Figure 4.24: Current entering the super-capacitor.

These current plots were filtered several times through a smoothing function in MatLab, and still they are quite distorted. Comparing the scale between the voltage and current plots it becomes clear that since the currents are orders of magnitudes smaller than the voltages, no significant distortions are seen in the voltages. Therefore, the voltage plots appear much smoother compared to the current plots. Further still the current plots do not exponentially go to zero as would be expected and as was seen in Figures 4.10 and 4.11. Instead the currents seem to settle to around 20 μA. Since the voltages plots appear to level off after about 16 hours, the current has reached its maximum rate at that time. Therefore, the current of 20 μA is the inflow of charge that is equal to the leakage charge and the system has reached an equilibrium. Therefore, since only the inflow of charge was measured with the DMM, the Coulomb count is a over estimation of the actual charge collected.

The first experiment collected an inflow of charge of $Q = 2.0965$ C and the second experiment $Q = 2.2802$ C. This accounts to an average total inflow of charge of $Q = 2.18835$ C. Clearly this charge is grossly too much as the capacitor, at best, has a capacitance of 1.462 F while the maximum voltage is around 0.85 V. Which implies, by $Q_{\max} = CV = (1.462)(0.85) = 1.2427$ C, that the average total charge of 2.18835 C is 76% larger than theoretically possible. However, it is possible to calculate backwards to obtain what the leakage current ought to be in order to account for the total average charge that entered the super-capacitor. The difference between the theoretical maximum and the calculated total average charge is $\Delta Q = 2.18835 - 1.2427 = 0.94565$ C, which over 24 hours implies a leakage current of 10.95 μA. This is nearly half the asymptotic amount shown in the current plots. However, it should be understood that this figure is only a rough estimate as A) the exact capacitance is unknown due to the temperate sensitivity of a super-capacitor and thus the uncertainty in the theoretical maximum charge, and B) as the leakage current is assumed to be constant throughout the entire 24 charging.

To get a better sense for how much charge is available for applications such as for WSNs, the power and energy plots are shown next. First the power plots are shown in the following set of figures.

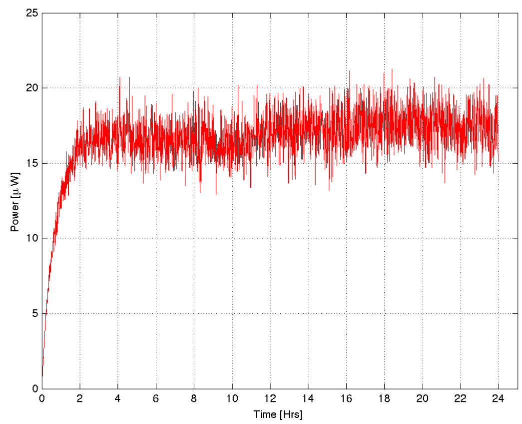

Figure 4.25: Power flow into the super-capacitor.

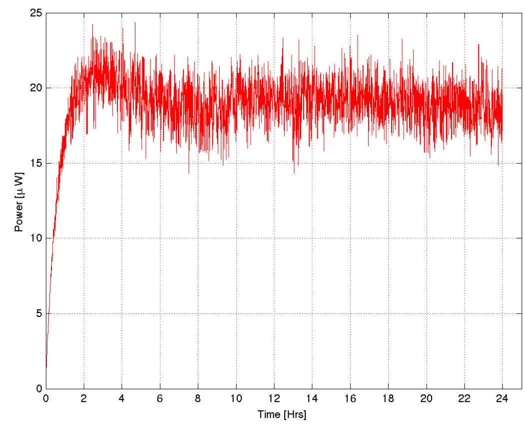

Figure 4.26: Power flow into the super-capacitor.

Due to the noisy nature of the current plots, the power plots are also quite noisy. Unlike the power plots for the transformer in Figures 4.12 and 4.13, here the power plots do not seem to peak but rather level off after 2-4 hours and remain quite high comparatively. However, most importantly is the energy available at the end of the 24 hours. This is shown in the following set of figures.

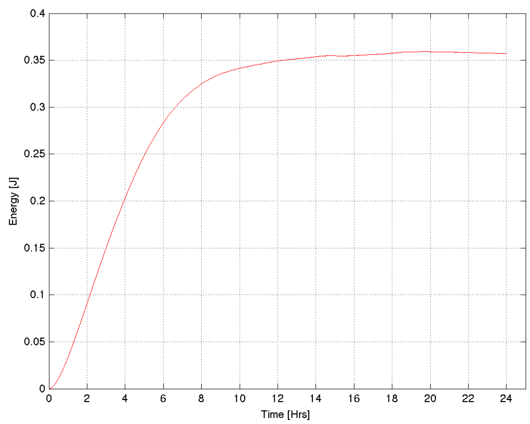

Figure 4.27: Energy available on the super-capacitor.

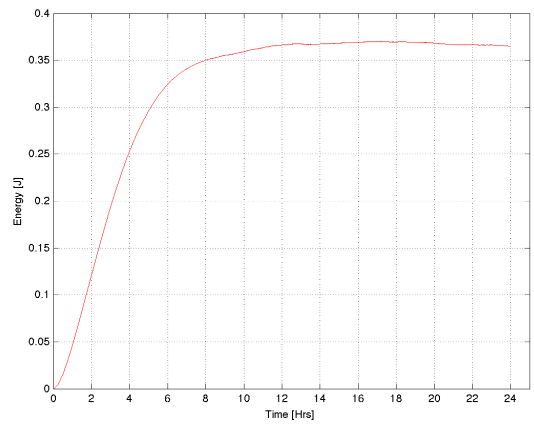

Figure 4.28: Energy available on the super-capacitor.

The combined average energy level at the end of the 24 hours is 0.36 J. This is considerably higher than the peak energy as was seen in the transformer experiments. Therefore, as was done for the transformer case, if an IC radio on a WSN node is active for 15 minutes per day, the chip may draw about 400 μW of power during that time. Considering that this is a gross underestimate, as was explained in Section 4.2, the capacitance was taken to be 1 F, and not the 1.462 F. Therefore, even though the vibration signals on fan # 13 were quite distorted due to large harmonics to the point that the Fourier spectrum indicated more random than periodic behaviour, enough charge may be collected for the purpose of powering WSNs.

4.4.2 Industrial Fan # 15

The second fan used in the experiments is fan # 15. A picture of the fan is shown in the following figure.

Figure 4.29: Industrial fan #15 used for application in vibrational energy harvesting.

Although the construction of this fan as compared to the previous fan # 13 is similar, the vibrations are quite different. The following figures are the vibrations of the two respective experiments on fan # 15 in the z-direction.

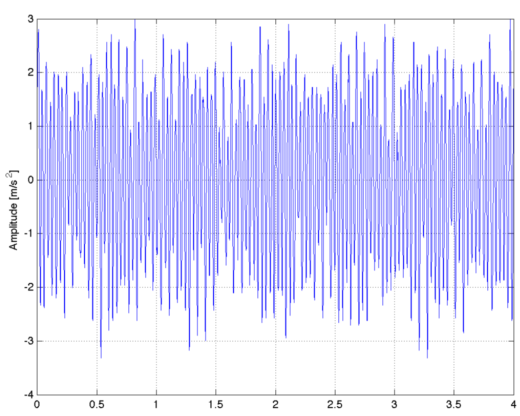

Figure 4.30: Z-axis vibration.

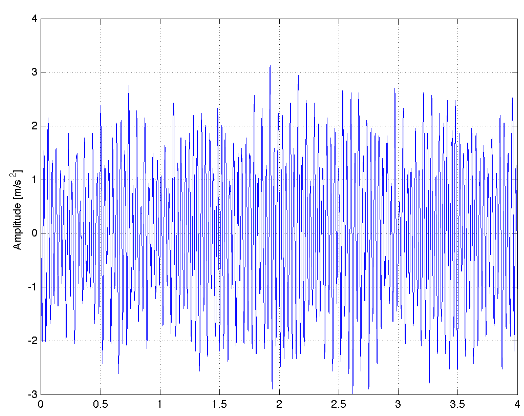

Figure 4.31: Z-axis vibration.

Similar to the previous fan, the vibrations on fan # 15 also seem rather noisy. An inspection of the Fourier spectrum should provide more detail. This is shown in the following set of figures.

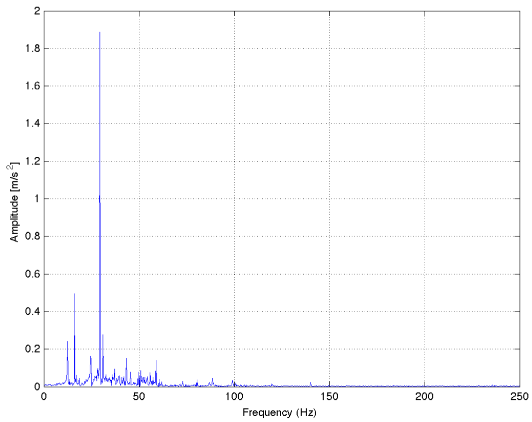

Figure 4.32: Fourier spectrum of input vibrations. $A_{120\,\mathrm{Hz}} = 0.015\, m/s^2$.

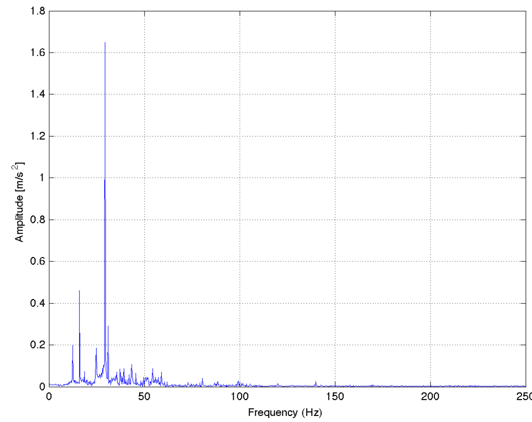

Figure 4.33: Fourier spectrum of input vibrations. $A_{120\,\mathrm{Hz}} = 0.0171\, m/s^2$.

Here it can be seen that A) the amplitudes are larger, and B) there are less harmonics. Since both Fourier spectrums have very similar harmonic distribution, which was unlike fan # 13, the vibrations here are much more periodic. Albeit these better working conditions for energy harvesting, the 120 Hz amplitudes are slightly smaller than on fan # 13 by more than a factor of two. With this data, it is expected that the energy available at the end of the 24 hours ought to be less than that which was seen in the fan # 13 experiments. First the voltage plots are shown in the following set of figures.

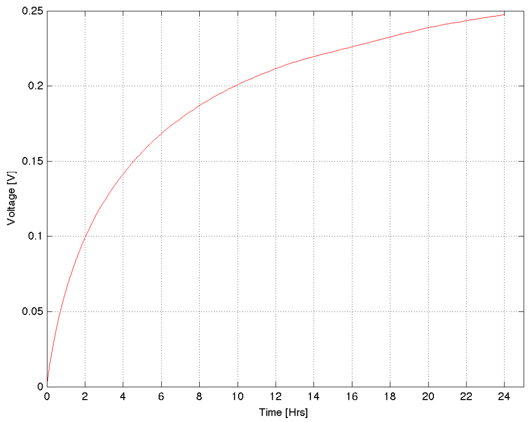

Figure 4.34: Voltage across the 1F super-capacitor.

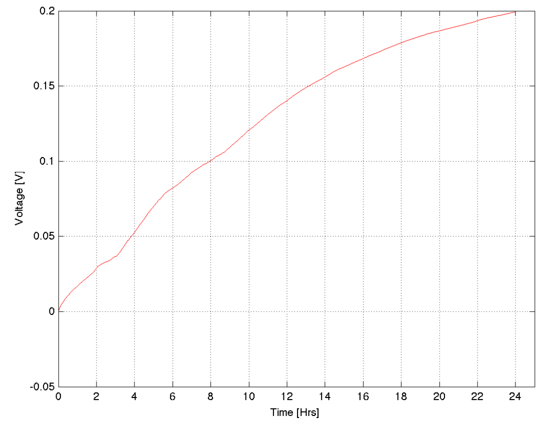

Figure 4.35: Voltage across the 1F super-capacitor.

It is clear from these plots that the voltage did not have enough time to level off due to the low excitation amplitude at the 120 Hz mark as discussed above. Further, the second voltage plot in Fig. 4.35 does not quite have the expected voltage curve for a charging capacitor. This curve shape might be explainable when looking at the current plots. These are provided in the following set of figures.

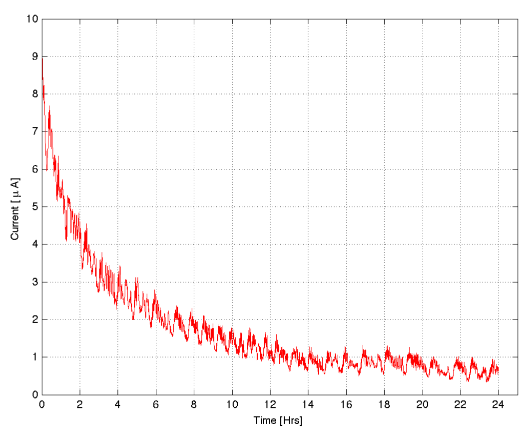

Figure 4.36: Current entering the super-capacitor.

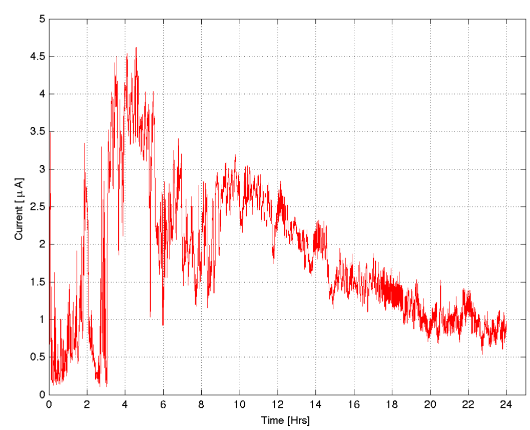

Figure 4.37: Current entering the super-capacitor.

Once again, these current curves are quite noisy due to the harmonics and the small scale on which the currents are plotted. Therefore, the current plots were smoothed with a smoothing function in MatLab (the current plots as shown are already the smoothed curves). The first current plot shows the expected behaviour. Not only is the shape correct, the curve also appears to tend to zero as was originally expected but that was not the case for the currents plots of fan # 13. Therefore, the Coulomb count should be more accurate than the gross overestimate of the fan # 13 Coulomb count.

On the other hand, the current plot of the second experiment on fan # 15, as seen in Fig. 4.37, has a quite unexpected waveform. This can explain the unusual corresponding voltage curve as the current is abnormal. The cause for this is likely a change in vibration in either amplitude or harmonics, or both. Since the vibration Fourier spectrum was not tracked for the duration of the 24 experiments, it cannot be concluded with perfect confidence that a change in vibration characteristics is the cause, however it is quite likely. Perhaps the fan during that particular experimental run was more active or another external source caused injection of vibration harmonics into the system.

Although the two current plots of fan # 15 are quite different from each other, the respective Coulomb count are impressively similar. The first experiment collected a total of incoming charge of $Q = 0.1519$ C while the second collected $Q = 0.1556$ C. This charge is considerably less than on either fan # 13 or the transformer. This was as expected after considering the Fourier spectrum of the vibrations. Next the power plots are shown in the following set of figures.

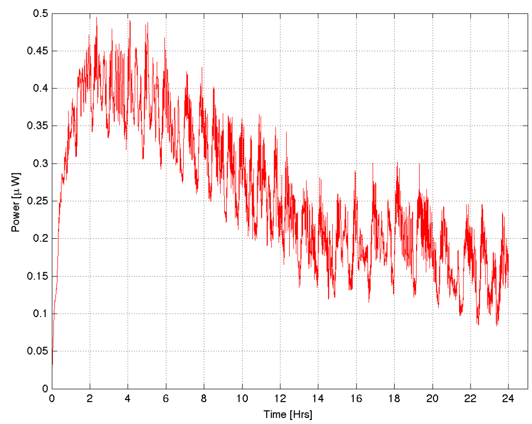

Figure 4.38: Power flow into the super-capacitor.

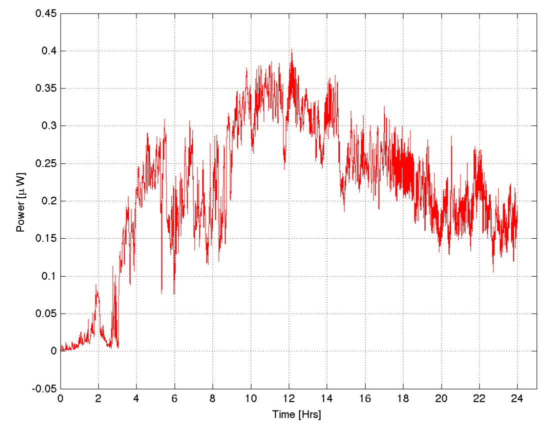

Figure 4.39: Power flow into the super-capacitor.

Even thought both respective current plots were smoothed with a smoothing function in MatLab, the power plots still display quite a large distortion. However, the first power plot is quite as expected. The power peaks somewhere between two and four hours and then decreases. Also unsurprisingly the second power plot is unusual due to the corresponding current curve. Finally the energy plots are shown in the following set of figures.

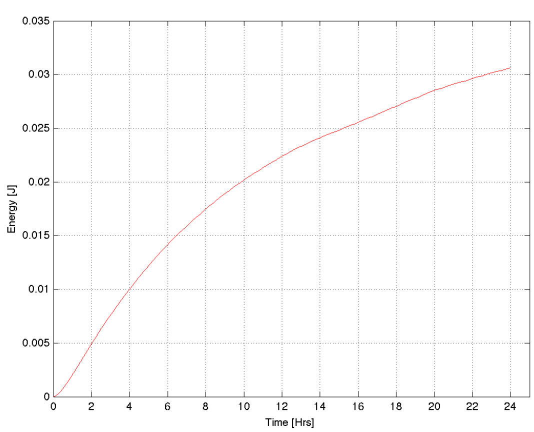

Figure 4.40: Energy available on the super-capacitor.

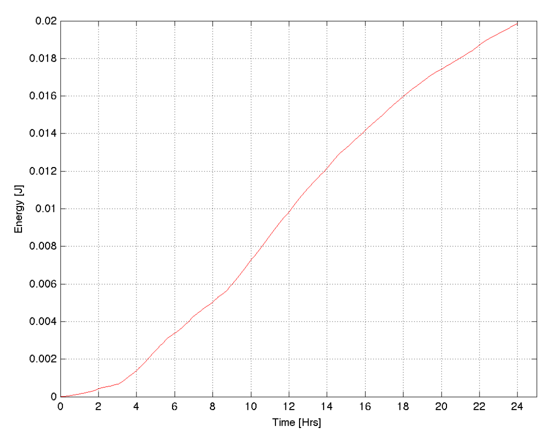

Figure 4.41: Energy available on the super-capacitor.

Considering the Fourier spectrum of the vibrations on fan # 15, the low energies as seen in the energy plots is quite expected. The highest energy peak (reached by the first experiment) was just under 31 mJ. If a radio IC turns on for 15 minutes per day, it would only have 34.4 μW of power available. This is more than a factor of 11 less than the power available on fan # 13. However, considering that this figure is an underestimate (due to only using 1 F as opposed to 1.462 F), and the fact that some WSNs have been reported to require around this much power (see Section 1.4), even this small amount of power may be enough for applications in WSNs.

4.4.3 Repositioning of Harvester Unit

As was seen in the previous two subsection on fans # 13 and # 15, the vibrations contained a lot of harmonics. However, only the z-axis vibrations were considered in those studies as that is the only direction that has significant effects on the cantilever. In this subsection another vibration axis is considered. Fans # 13 and # 15 are considered again in two successive experiments with the data of fan # 13 on the left and fan # 15 on the right of all the following figures. To see why considering other vibration axis might be useful, the following set of figures shows the x-, y-, and z-axis vibration on both fan respectively.

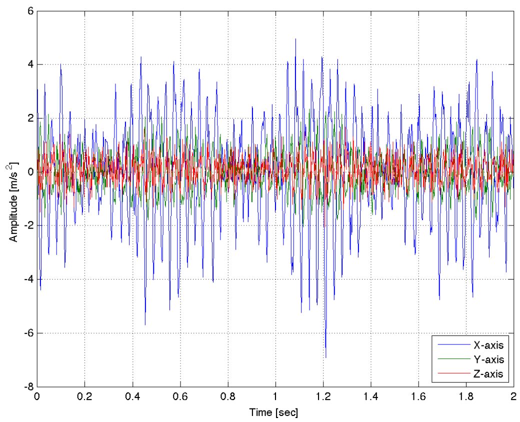

Figure 4.42: Three axis of vibration on fan # 13.

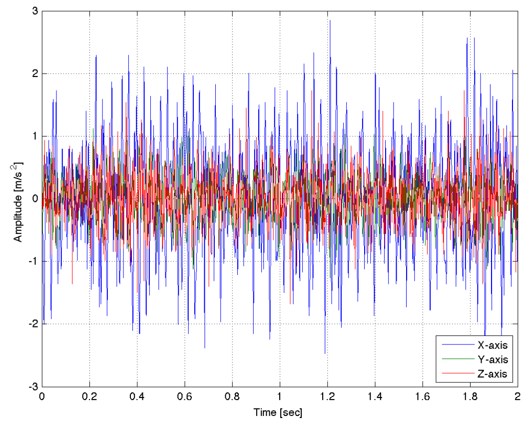

Figure 4.43: Three axis of vibration on fan # 15.

Two interesting features should be noted about the vibrations as seen in these figures. Firstly it is evident that the x-axis direction has larger amplitudes than either of the other two. The x-axis is horizontal outward direction normal to the face of the fans. Recalling that before the z-axis direction was used, which corresponds to the harvester unit to be such that the cantilever is horizontal as seen in Fig. 4.2. Therefore, for this subsection the harvester unit is repositioned to be in a vertical state with the cantilever suspended downward. This utilizes the x-axis and becomes the new z-axis.

The second feature to note is that fan # 13 has a beat frequency in the x-axis (the new z-axis) whereas the other fan does not. This beat frequency is so pronounced that one is able to feel it with bare hands when touching fan # 13. The following figures are the Fourier spectra of the vibrations in the new z-axis.

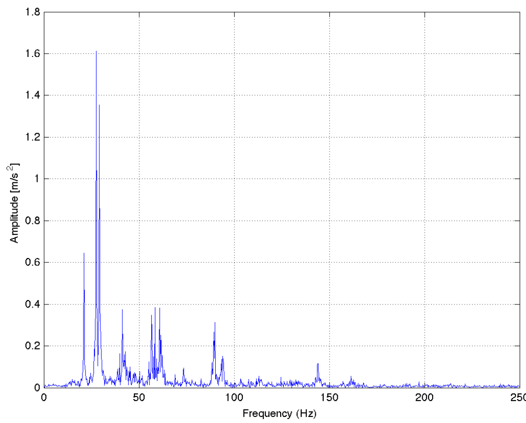

Figure 4.44: Fourier spectrum of input vibrations for fan # 13. $A_{120\text{ Hz}} = \text{noise}$.

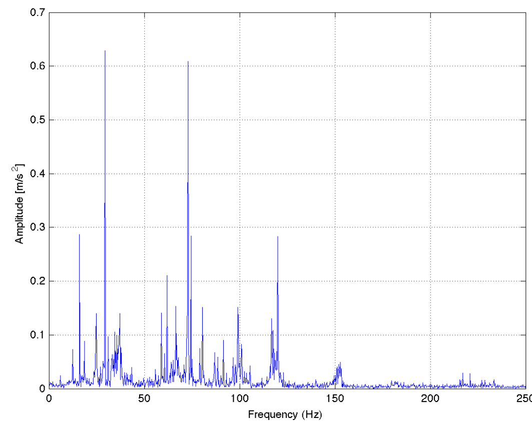

Figure 4.45: Fourier spectrum of input vibrations for fan # 15. $A_{120\text{ Hz}} = 0.283\, m/s^2$.

Interestingly the 120 Hz component of fan # 13 is not any larger than noise from other harmonics. This leads to imply that there is next to no contribution of a 120 Hz component. The other fan however does have a contribution at 120 Hz with an amplitude of 0.283 m/s^2. Also note that there are a lot more harmonics than in both fans on this z-axis as compared to the previous z-axis. The amplitude of fan # 15 is exceptionally larger than on the same fan but the previous z-axis.

The following set of figures is the voltage across the super-capacitor for fan # 13 and # 15 respectively. Considering that for fan # 13 there is no excitation frequency input at 120 Hz, it is reasonable to expect a very low voltage curve.

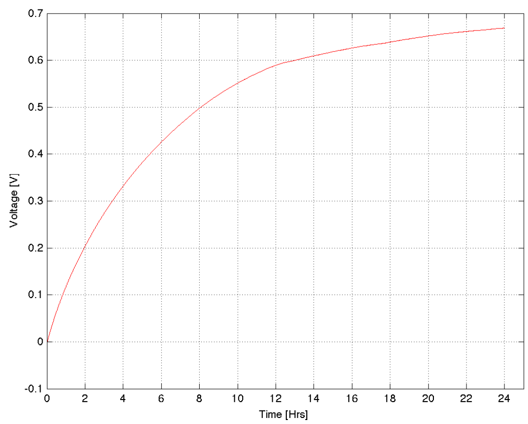

Figure 4.46: Voltage across the 1F super-capacitor on fan # 13.

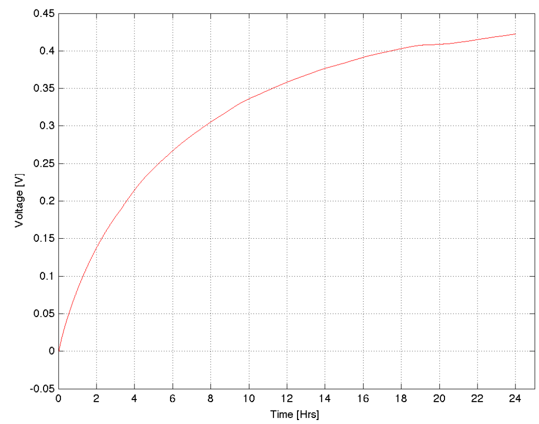

Figure 4.47: Voltage across the 1F super-capacitor and fan # 15.

The first feature to note is that neither voltage plots have reached an asymptote. This is quite interesting as fan # 13 had such a low amplitude at 120 Hz but has a higher voltage than fan # 15 which had quite a large amplitude at 120 Hz. This leads to suggest that the presence of harmonics can have quite unpredictable results. In the case of fan # 13, harmonics effected the voltage in a constructive manner, causing a larger voltage build-up. Whereas the harmonics on fan # 15 had destructive effect causing the voltage to not build up as much as was expected.

Next the current plots are shown in Figures 4.48 and 4.49.

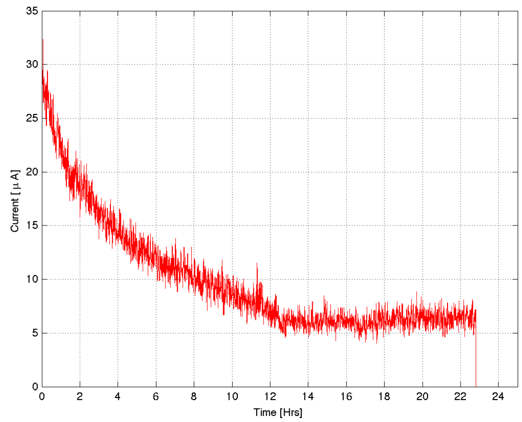

Figure 4.48: Current entering the super-capacitor of fan # 13.

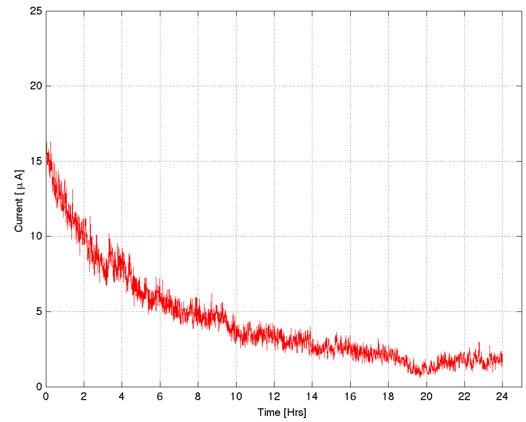

Figure 4.49: Current entering the super-capacitor of fan # 15.

The DMM malfunctioned on the 23$^{\text{rd}}$ hour of the experiment for fan # 13. However, it appears that the current at that stage had already levelled off at just above 5 μA. Notice that the current starts out much larger on fan # 13 as compared to fan # 15, which is consistent with the previous voltage plots. The Coulomb count of the inflowing charge on fan # 13 is $Q = 0.8214$C (because the last hour is missing in this, the Coulomb count is slightly an underestimate as compared to the other Coulomb counts) and on fan # 15 $Q = 0.3830$ C. Next the power plots are shown.

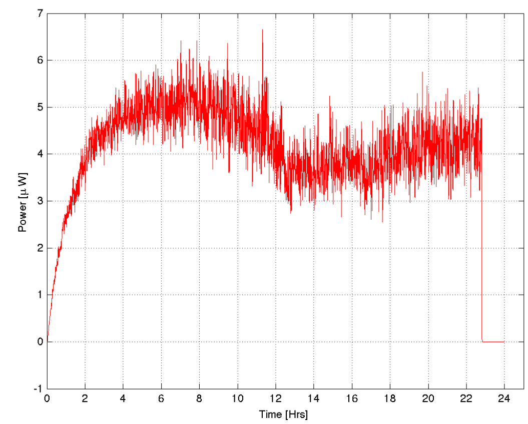

Figure 4.50: Power flow into the super-capacitor.

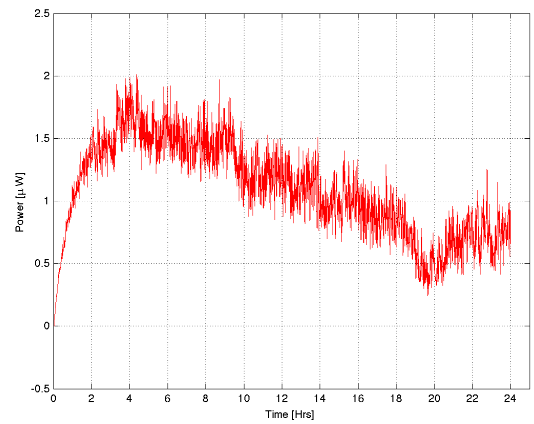

Figure 4.51: Power flow into the super-capacitor.

The power flow of fan # 13 is curious as the power appears to be increasing after the 14th hour. This is consistent with the slight upwards tail seen in the corresponding current. The power plot of fan # 15 is as expected with a peak at about the 4th hour, except for near the end when a similar upwards tail is apparent. Next the energy plots are shown.

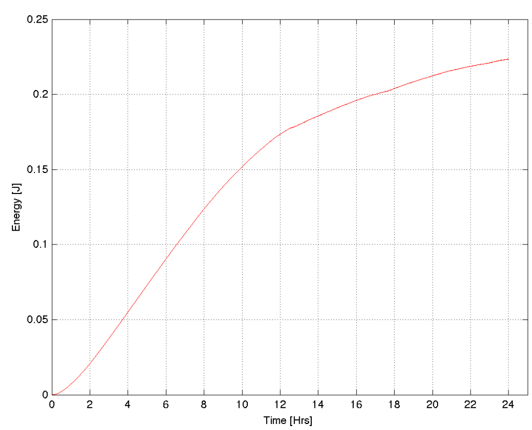

Figure 4.52: Energy available on the super-capacitor.

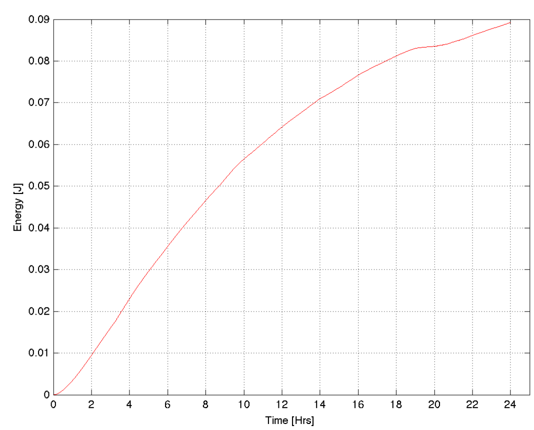

Figure 4.53: Energy available on the super-capacitor.

Consistent with the voltage plots, these energy plots are not yet levelled off. Their end vales are 0.22 J and 0.09 J for fan # 13 and # 15 respectively. These values are 0.6 times and 2.9 times the respective energy peaks from the previous z-axis (before changing the cantilever position from horizontal to vertical).

4.5 Higher Mode Discrepancy

This section does not consider energy harvesting using the harvester unit as was done in the previous sections, but instead presents a possible limitation of the equations derived in Chapter 2 that describe the physics of piezoelectric cantilevers. A curious phenomena, called in this thesis *the higher mode discrepancy*, which was discovered through testing and experimentation is presented and discussed. The higher mode discrepancy is a disagreement between the predicted higher modes using the MatLab script and the experimentally measured modes. This discrepancy seems to be inherent to the bimorph construction as higher modes using a unimorph were shown to agree within literature (see Section 3.2).

To illustrate the discrepancy, the original bimorph cantilever as outlined in Section 3.4.1 is used and excited with the speaker shaker. A PM circuit is not necessary to demonstrate the higher mode discrepancy. In fact a PM circuit would be a hinder in this study. This is because a frequency sweep is performed that would cause continuous transients for continuously changing frequencies if the PM circuit contains any energy storage elements. Therefore, no PM circuit is attached and only a resistor of 9930 Ω is added as a load. This eliminates any transients and allows for an accurate frequency spectrum.

The following figure is of a frequency sweep with the RMS ac voltage over the resistor as an output. The sweep is linear and took 900 seconds to sweep from 1 Hz to 1500 Hz in order to capture the first three modes of vibrations accurately.

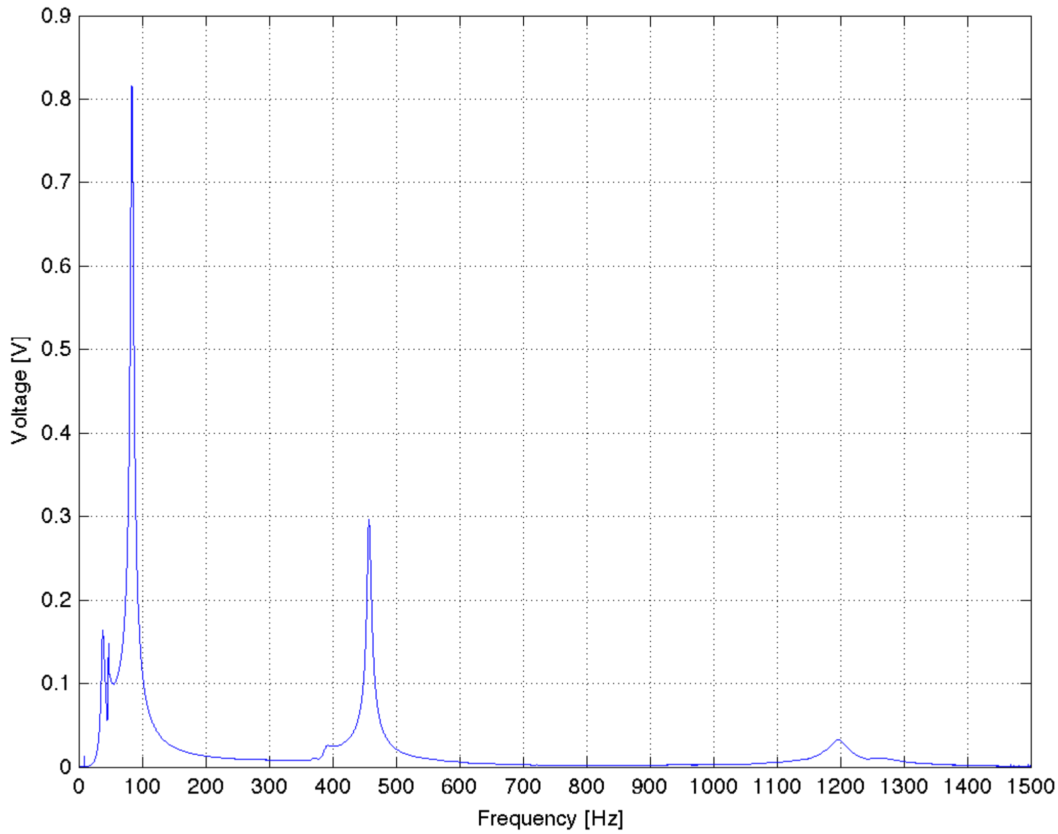

Figure 4.54: Frequency sweep over resistor $R_{\text{out}} = 9930\,\Omega$. The voltage along the y-axis is measured in RMS. The three first peaks of resonance are: $f_1 = 76.8\,Hz$, $f_2 = 450.9\,Hz$, $f_1 = 1190.0\,Hz$.

The first three modes of vibration are clearly visible in the frequency sweep as seen in the figure. There is a small cluster of resonance peaks around 50 Hz just prior to the first mode of vibration. This cluster is caused by the resonance of the speaker shaker itself and is unavoidable with this particular setup. However, since the first mode of vibration is far enough away from the cluster there is no mutual interference. Further, around 390 Hz, just before the second mode of vibration, is a small kink. While the first cluster appears on every frequency sweep that was done, the kink around 390 Hz does not always appear and hence it is believed that it is not a resonance point of the speaker shaker. The exact cause of the kink is unknown. However, just like the first cluster, the second mode is located far enough away to not cause any interference. The following table summarizes the results of the experimental frequency sweep and the MatLab simulations results. The simulated results include eight ECM modes to ensure accuracy of the first three modes of vibration.

Table 4.1: HIGHER MODE DISCREPANCY RESULTS

Mode	Experimental	Simulation	Percent difference
f_1 [Hz]	76.8	76.6	0.26%
f_2 [Hz]	450.9	483.3	7.19%
f_3 [Hz]	1190.9	1339.2	12.45%

As can be seen in the table, the percent difference grows with increasing number of resonance modes considered. It is expected that this discrepancy will continue to grow for modes higher than three albeit this was not performed as increasingly higher modes of decreasingly smaller amplitudes make them difficult to find with this speaker shaker setup. Notice also that the first mode of the simulation results can be made as accurate as desired as the effective length of the lever has a range of acceptable values (see end of Section 3.4.1 for a discussion on the effective length of the cantilever.).

It is curious to note that such a discrepancy does not exist for the unimorph cantilever configuration as higher modes were shown to agree with experimental and simulation results in Section 3.2. Therefore, it allows to conjecture that the discrepancy is a consequence of the bimorph geometry. If this is the case then it can also be assumed that multi-layer cantilevers with more than two PZT and one supporting shim experiences this discrepancy and perhaps even to higher degree.

However, the exact cause of the discrepancy is not known. It is likely that this effect is caused by a mechanical mechanism of the manner in which the bimorph cantilever vibrates. Perhaps sheering forces between the three layers arise that were either insignificant or nonexistent in the unimorph case. Or perhaps the stiffness of the lever is not modelled accurately which could explain the systematic percent difference in the modes. If either of these are the case, then in principle it should be possible to find a correction term to account for the difference and improve the accuracy of the model.

Another likely explanation of the discrepancy could be that the assumed mode shapes in Assumption 1 is simply not accurate for higher modes. Some authors such as Erturk and Inman [10, 12] or Inman [7] use different assumed mode shapes. Although investigating these other assumed mode shapes has not been done in this thesis work, it can be done by adjusting the theory accordingly and editing the MatLab script. This is left for future work.

What ever the cause of the discrepancy in reality this effect does not have any significant impact in vibrational energy harvesting as was studied in this thesis. This is because only the first mode of vibration is utilized in these sort of applications as the amplitude of the first mode is considerably larger than any other mode for thin rectangular cantilevers. It is, however, possible that certain constructions of piezoelectric cantilevers could have successive modes that have a higher amplitude than lower order modes. For energy harvesting the mode with the highest amplitude should always be chosen if the frequency of said mode is available with the geometric restrictions of the physical PZT transducer. Therefore, finding a solution to the higher mode discrepancy is purely an intellectual exercise and has little value in practical applications of vibrational energy harvesting to power WSNs.

4.6 Chapter Contributions

This chapter presented the experimental aspect of piezoelectric vibrational energy harvesting. The laboratory setup utilizing the speaker shaker made for a cheap and innovative setup costing less than 1.4% of traditional shakers. This allowed for experimental laboratory testing and tuning of the cantilever. Although this setup was sufficient for the testing and tuning as was required in this thesis, the speaker shaker had some drawbacks such as non-vertical vibration excitation and non-constant amplitude vibration over a large range of frequencies. However, neither of these drawbacks is significant for the purposes of this study.

The first experiment was performed on a laboratory transformer that has regular and fairly clean vibrations. Two suggestive 24 hour experiments were performed on the transformer and it was found that enough energy can be gathered in the super-capacitor to realize WSNs applications.

Afterwards two different industrial fans were used in several experiments. It was found that the fans exhibit quite different vibrations both in terms of amplitudes as well as harmonics. Also the harvester unit was tested in two positions first in the regular horizontal position and then, by rotating the harvester unit to utilize another vibration axis, the vertically downwards position. In all of the experiments enough energy was gathered in order to use for applications with WSNs.

Not only were all the results positive, they were also very conservative for two reasons. First, as was discussed early in the chapter, the actual capacitance is much higher than the rated capacitance on the super-capacitor. The reason why the actual capacitance was not used is because this value fluctuates as it is a function of temperature among other parameters. Since the Coulomb count was an over-estimate, the capacitance curves were not able to be obtained accurately. Therefore, given this reasoning the extra capacitance was considered to account for any sources of error that is still quite conservative. The second factor to consider was that the PM circuit used was rather primitive and not nearly as efficient as modern PM circuit designs as discussed in Section 1.5. If using a dc-dc converter as part of the PM circuit, and even better using impedance or resistance matching, the energy collected can increase by a factor of four.

A very curious phenomena due to harmonics was discovered via the experiments in this chapter that was not previously discussed in literature.

Namely the positive and negative interferences of harmonics within the vibration sources. Especially noticeable in the fan applications, a large presence of harmonics can be useful in energy harvesting. As was studied, even a vibration source that does not have a significant harmonic contribution to which the cantilever is tuned (e.g. 120 Hz) can still be utilized for vibrational energy harvesting. Such results have two significant consequences. Firstly the fine-tuning of a cantilever may not be as important as previously thought if enough harmonics are present in the vibrational source such as was found in the industrial fans. Secondly the designing and engineering of harvester units should change focus away from idealized laboratory settings and towards realistic applications. As was demonstrated, each vibrational source can have quite different harmonics. If enough harmonics are present it becomes very difficult to model and predict the energy outcome on the storage device (a super-capacitor in this study), not to mention the open-circuit voltage across the PZT element. Therefore, if designing a harvester unit it is of utmost importance to sample the vibrational source harmonics first and adjust the harvester unit accordingly.

For example, the transformer had a sharply peaked harmonic at 120 Hz and so it makes sense to tune the cantilever to exactly 120 Hz in order to harvest the maximum power available. This is useful only if no other significant harmonics are present. However, applications such as the industrial fans, which have such strong and distorted vibrations that they can hardly be considered periodic, may alter the way a cantilever is designed. If one does not have the restriction of tuning the cantilever to a particular frequency, then other design focuses can be achieved such as for example smaller cantilever designs.

Another curious phenomena that was discovered during the experimentation and testing in the laboratory is the higher mode discrepancy. This phenomena, which is non-existing for the unimorph case, has not been reported in literature. The exact cause of the higher mode discrepancy was not discovered, however several solutions are proposed that may help provide a solution in order to correct the simulations. It is suspected that this higher mode discrepancy is a function of geometry of the PZT transducer and therefore also present in multi-layer PZT harvesters albeit this was not studied. Nevertheless the higher mode discrepancy is not a major problem when it comes to engineering the harvester unit as most often only the first mode of vibration is utilized.

Chapter 5

Conclusion & Future Work

This thesis investigated the feasibility of vibrational energy harvesting using piezoelectric cantilevers. A large spectrum of the various aspects involved with such energy harvesting was considered including the mathematical framework needed to describe the physics, the simulation based on the mathematics which was important for tuning the cantilever as well as obtaining ECM components, and finally experimentation to verify the simulations as well as present a proof-of-concept harvester unit design.

The following two sections briefly outline the contributions made in this thesis as well as suggested future work that may expand on the present study.

5.1 Thesis Contribution and Conclusion

No innovative or novel theoretical contributions were presented in Chapter 2 that lead to a new or deeper understanding of the physics of vibrational energy harvesting using piezoelectric transducers. However, this chapter pulled together all the various works done in literature and presented a logical and fully detailed derivation from the start using Hamiltonian analysis to the end drawing an isomorphism to RLC circuits. Such a complete derivation is useful for readers new to this topic.

Similarly for Chapter 3, no significantly novel contributions to the field of vibrational energy harvesting were made in terms of simulations. This is because much of the theoretical and simulation work has been done and published in the literature. However, this chapter, just like the previous one, pulled together and reenforced various theoretical features of a energy harvesting system. Further this chapter demonstrated how to obtain the ECM components that may be used to better design PM circuits. This could be a very useful tool, especially for electrical engineers, to use alongside simulation software such as PSpice or PSCAD in order to model the PM circuits accurately.

The crux of the thesis contributions are found in Chapter 4. The most striking and counterintuitive discovery was that vibrational sources that contain many harmonics may be used to harvest energy even though the first resonance frequency of the cantilever may not directly be excited. With this understanding comes the possibility of relaxing the precise fine tuning previously thought to be necessary. This allows to focus on other engineering design criteria such as geometry of the cantilever or other restrictions. Unfortunately due to the complicated motion of highly excited vibrational sources such as the industrial fans studied, the harmonic distribution is too dynamic and seemingly chaotic to incorporate into simulation and design of harvester units. An alternative approach is to analyze each vibrational source separately and design the harvester unit around the harmonics present.

Another interesting discovery of Chapter 4 is the higher mode discrepancy found experimentally in the bimorph geometry. In the unimorph geometry, higher modes (the first three) were matched in simulations with experimental results and therefore no such higher mode discrepancy were found to exist. However, the bimorph cantilever, presumably also other multi-layer transducers, exhibit a discrepancy between the higher modes predicted with simulations to the experimentally measured modes. The exact cause of this phenomena is not understood as of current, however several solutions have been suggested.

The collective experimental results suggest that vibrational energy harvesting is quite feasible with the strategy employed in this study. Namely to realize energy harvesting with a PM circuit as simple as possible. Albeit the PM circuit used in this study is rather inefficient compared to modern circuits used in this application, the energy collected was nevertheless sufficient for applications within WSNs. With this bare minimum approach successful, more future work presents itself in order to increase the energy harvested from vibrations.

5.2 Future Work

The most obvious design consideration that can be improved upon is the PM circuit design. As previously stated, the energy harvested with the inclusion of a dc-dc converter can increase by more than a factor of four. Sophisticated impedance matching and power point tracking algorithms can be implemented to increase the harvested energy even further. Much work has been done in this regard and it is simply a matter of designing the most efficient PM circuit suitable depending on the vibration source.

Besides improving upon the PM circuitry design other features can also be improved such as the shape of the piezoelectric cantilever. For example a triangularly shaped cantilever with the sharp tip at the free end of the lever has a better strain distribution along the piezoelectric material and thus establishes a larger voltage across the terminals as compared to rectangular cantilevers under the same conditions [35]. Further, and along the lines of geometry shape, reducing the size of the piezoelectric cantilever to fit in the size of one cubic centimetre is the design goal of some authors [8]. Indeed the cantilever and the overall harvester unit used in this thesis may be too large and bulky for practical applications such as for WSNs. Although industry interest has already emerged and companies such as MicroGen Systems Inc. is selling off-the-shelf, pre-tuned, harvester units [36] that are not significantly smaller than the harvester unit presented here.

With an increasingly growing interest in environmentally friendly technologies there is some focus on adapting lead-free piezoelectric materials for energy harvesting as opposed to PZT [1]. Although PZT is the most common material to use in vibrational energy harvesting as the piezoelectric effect is the strongest, there exist many other materials that may be substituted in its place. With improving vibrational energy harvesting efficiencies due to, for example, better PM circuits or cantilever shapes, adapting a lead-free material and thus harvesting slightly less energy becomes affordable.

This thesis demonstrated the feasibility of vibrational energy harvesting using a simplistic design strategy. As was discussed much improvement can be made in order to optimize the energy available in vibrations. At this point in the research community such technology is starting to become mature and most design issues have been addressed. Therefore, vibrational energy harvesting with piezoelectric materials becomes a matter of optimization for each vibrational source. Using vibrational energy to power WSNs has become a realized possibility and with further improvements being made in the coming years alongside with decreasing energy demands of modern technology, vibrational energy harvesting will see a growing application range beyond WSNs.

Appendices

Appendix A

Method of Hamilton's Principle

The method of Hamilton's principle allows the equations of motion to be solve of systems, much like Newton's laws do. However, Hamilton's principle is more general than Newton's laws that can be derived from the principle. Here the derivation of the Euler-Lagrange equation using Hamilton's principle as a starting point is shown. The Euler-Lagrange equation is analogous to Newton's laws of motion with the added advantage that the form of the Euler-Lagrange equation is invariant in any generalized coordinate system.

To be able to state Hamilton's principle, several definitions must first be made. A functional, denoted with the use of square brackets such as $F[g]$, is a scalar value that has functions as inputs. For example [31],

$$F[g] = \int_a^b f(g)dx, \tag{A.0.1}$$

is a functional where $f(g)$ is some function of g and its derivatives. Consider the functional

$$S[q,\dot{q}] = \int_{t_1}^{t_2} L(q_i(t),\dot{q}_i(t),t)dx. \tag{A.0.2}$$

The function L is defined as the kinetic energy minus the potential energy such as

$$L \equiv T - V, \tag{A.0.3}$$

and is called the *Lagrangian*. The i generalized coordinates are given by q_i while the generalized velocities are $\dot{q}_i$. With L defined as the Lagrangian, the functional S in (A.0.2) is called the *action*.

When dealing with the action one is often interested in the variation of the action. Consider the first order perturbation in the generalized coordinates

$$q_i(t) \to q_i(t) + \delta q_i(t), \tag{A.0.4}$$

where the variation is arbitrary along any path between the end points t_1 and t_2 but remains zero at the endpoints. The variation in the action to first order can be defined as

$$\delta S[q,\dot{q},t] \equiv S[q+\delta q,\dot{q}+\delta\dot{q},t] - S[q,\dot{q},t]. \tag{A.0.5}$$

When combining this with the first order Taylor expansion of the Lagrangian with first order perturbations

$$L(q+\delta q,\dot{q}+\delta\dot{q},t) = L(q,\dot{q},t) + \frac{\partial L}{\partial q_i}\delta q_i + \frac{\partial L}{\partial \dot{q}_i}\delta\dot{q}_i, \tag{A.0.6}$$

the following is obtained

$$\delta S = \int_{t_1}^{t_2} \left(\frac{\partial L}{\partial q_i}\delta q_i + \frac{\partial L}{\partial \dot{q}_i}\delta\dot{q}_i \right) dt. \tag{A.0.7}$$

Notice that in the definition of the the variation of the action, δS, only first order terms were considered just like the Taylor expansion following. One could include higher terms in both and arrive at the same result.

A more elegant derivation of δS is done by defining the variation as an operator on the family of curves of the generalized coordinates with parameter α such that

$$\delta q_i(\alpha) = \left. \frac{\partial q_i(\alpha)}{\partial \alpha} \right|_{\alpha=0} \tag{A.0.8}$$

$$\delta S[\alpha] = \left. \frac{dS[q(\alpha)]}{d\alpha} \right|_{\alpha=0} \tag{A.0.9}$$

with $q_i(0,t) = q_i(t)$. Thus applying the variation on the Lagrangian results in

$$\begin{aligned}
\delta S &= \frac{d}{d\alpha} \int_{t_1}^{t_2} L(q_i(t), \dot{q}_i(t), t) dt \bigg|_{\alpha=0} \\
&= \int_{t_1}^{t_2} \left(\frac{\partial L(q(\alpha), \dot{q}(\alpha), t)}{\partial q_i} \frac{\partial q_i(\alpha, t)}{\partial \alpha} + \frac{\partial L(q(\alpha), \dot{q}(\alpha), t)}{\partial \dot{q}_i} \frac{\partial \dot{q}_i(\alpha, t)}{\partial \alpha} \right) dt \bigg|_{\alpha=0} \\
&= \int_{t_1}^{t_2} \left(\frac{\partial L}{\partial q_i} \delta q_i + \frac{\partial L}{\partial \dot{q}_i} \delta \dot{q}_i \right) dt, \qquad \text{(A.0.10)}
\end{aligned}$$

which is as stated before. The variation in the action as in either equation (A.0.2) or (A.0.10) can be manipulated into a more recognizable form by using integration-by-part such that

$$\delta S = \int_{t_1}^{t_2} \left(\frac{\partial L}{\partial q_i} - \frac{d}{dt} \frac{\partial L}{\partial \dot{q}_i} \right) \delta q_i dt + \frac{\partial L}{\partial \dot{q}_i} \delta q_i \bigg|_{t_1}^{t_2}. \qquad \text{(A.0.11)}$$

Recalling that the perturbation or variation is only *between* the limits and is held stationary *at* the limits, the second term in the last equation is identically zero.

Finally Hamilton's principle can be invoked which states that the variation of the action must be zero. In other words, given any constraints of motion, a system evolves such that the total energy is always at a minimum. This powerful statement can be expressed quite elegantly and succinctly as

$$\delta S = 0. \qquad \text{(A.0.12)}$$

Hamilton's principle therefore implies that the integrant in (A.0.11) must be identically zero. Thus the result is given as

$$\frac{\partial L}{\partial q_i} = \frac{d}{dt} \frac{\partial L}{\partial \dot{q}_i}, \qquad \text{(A.0.13)}$$

which is the famous Euler-Lagrange equation.

Appendix B

Piezoelectric Cantilever Impedance

For efficient power management circuit designs impedance matching is often employed between the piezoelectric generator and the load (see Section 1.5). It is therefore of interest to examine the impedance of a piezoelectric cantilever. The impedance of a piezoelectric cantilever is capacitive in nature [17]. To demonstrate this property the bimorph cantilever described in Section 3.4.1 is examined with properties outlined in Table 3.6[1]. No tip mass is considered in this analysis.

Using the MatLab script the equivalent circuit components are calculated using four equivalent modes. The following table lists the first mode values.

Table B.1: ORIGINAL CANTILEVER FIRST MODE COMPONENTS

$L_1\,[H]$	$C_1\,[\mu F]$	$R_1\,[\Omega]$	N_1	$V_1\,[V/g]$	$C_p\,[\mu f]$
1	5.657	23.538	0.067	0.070	0.267

Recalling from Section 3.1, the ideal transformer with turn ratio N_1 can be absorbed into an equivalent RLC circuit. Therefore, it is easy to calculate the impedance of the first RLC mode (using four equivalent modes for accuracy). The

[1] Note that the effective length is chosen to be 60 mm.

impedance is given by

$$Z_1(\omega) = \left(\frac{1}{R_1/N_1^2 + j\omega L_1/N_1^2 + \frac{1}{j\omega C_1 N_1^2}} + j\omega C_P \right)^{-1}. \tag{B.0.1}$$

Using this equation is it straightforward to find the open and closed circuit resonance frequencies. The closed circuit resonance frequency is 66.92 Hz while the open frequency is 69.85 Hz. The following two plots show the resistance and the reactance of the impedance with two vertical dashed lines indicating the closed and open frequencies respectively.

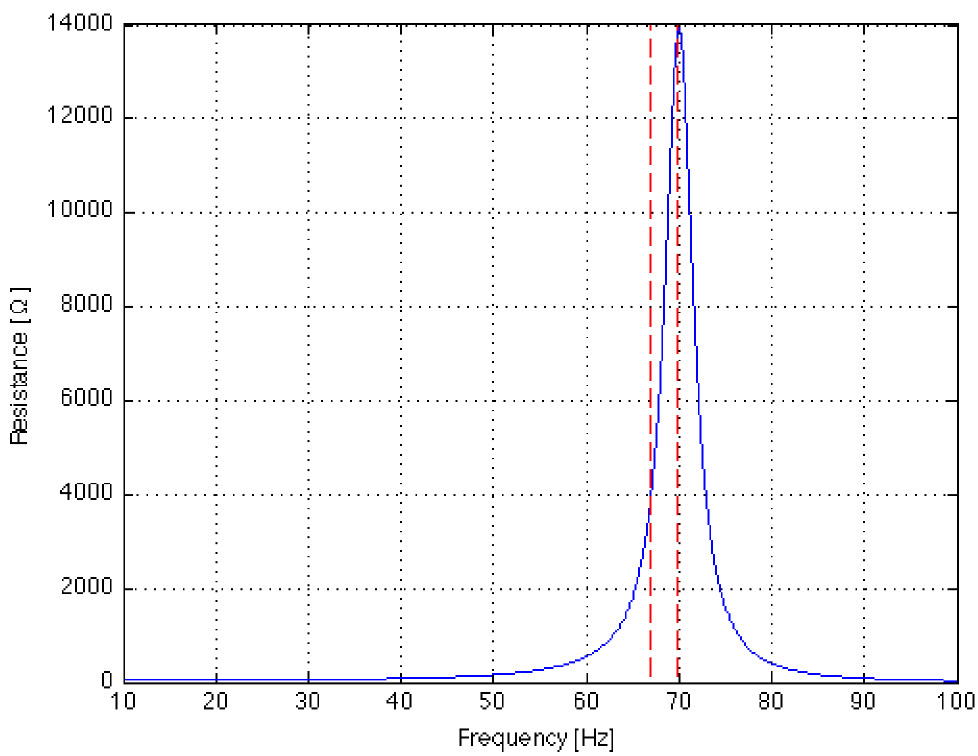

Figure B.1: Resistance frequency response of original bimorph cantilever. The left and right vertical lines are the closed and open circuit resonance frequencies respectively.

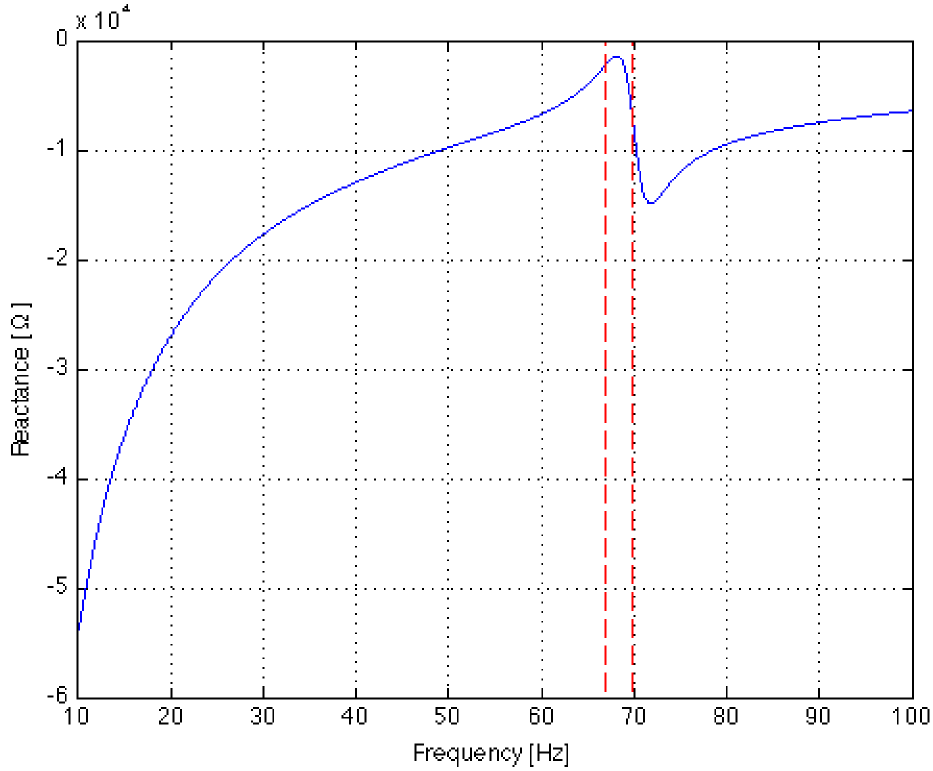

Figure B.2: Reactance frequency response of original bimorph cantilever.

Therefore, it can be seen that the reactance is at a magnitude minimum in the frequency range between the closed and open circuit values but remains capacitive at all times. This is consistent with results found in references [17, 20].

In terms of impedance matching PM circuit designs, as discussed in Section 1.5, it can be seen that while operating around the resonance frequency, the reactance is small and therefore under certain conditions a resistive impedance matching algorithm can be employed to good accuracy. However, while operating away from the resonance frequency and implementing full impedance matching, then due to the capacitive nature of piezoelectric cantilevers a rather large inductive element must be used in a PM circuit design. This is usually not practical, since a desired design feature of the PM circuits is miniaturization.

References

[1] P. K. Panda, "Review: environmental friendly lead-free piezoelectric materials," *J. Mater Sci*, vol. 44, pp. 5049-5062, July 2009.

[2] APC International Ltd. Mackeyville, PA, USA. www.americanpiezo.com.

[3] C. Kittle, *Introduction to Solid State Physics*, 8th ed., John Wiley & Sons, Inc. 2005.

[4] Piezo Systems Inc. Woburn, MA, USA. www.piezo.com.

[5] H. S. Tzou, *Piezoelectric Shells: Distributed Sensing and Control of Continua*, Kluwer Academic Publishers, 1993.

[6] T. R. Meeker, "Publication and proposed revision of ANSI/IEEE standard 176-1987 ‘ANSI/IEEE standard on piezoelectricity‘." *IEEE Trans. Ultrason. Ferroelectr. Freq. Control*, vol. 43, pp. 717-773, Aug. 1996.

[7] D. J. Inman, *Energy Vibration*, Prentice Hall, 2001.

[8] S. Roundy and P. K. Wright, "A piezoelectric vibration based generator for wireless electronics," *Smart Mater. Struct.*, vol. 13, pp. 1131-1142, Aug. 2004.

[9] APC International Ltd., *Piezoelectric Ceramics: Principles and Applications*, 2nd Ed., APC International Ltd., 2011.

[10] A. Erturk and D. J. Inman, "A distributed parameter electromechanical model for cantilevered piezoelectric energy harvester," *J. Vib. Acoust.*, vol. 130, pp. 041002-15, Aug. 2008.

[11] E. Lefeuvre *et al.*, "Buck-boost converter for sensorless power optimization of piezoelectric energy Harvester," *IEEE Trans. Power Electron.*, vol. 22, pp. 2018-2025, Sept. 2007.

[12] A. Erturk and D. J. Inman, "An experimentally validated bimorph cantilever model for piezoelectric energy harvesting from base excitations," *Smart Mater. Struct.*, vol. 18, pp. 1-18, Jan. 2009.

[13] J. Rabaey *et al.*, "2002 picoradios for wireless sensor networks: the next challenge in ultra-low-power design," *Proc. Int. Conf. on Solid-State Circuits*, vol. 1, pp. 200-201, Feb. 2002.

[14] W. Wang *et al.*, "Autonomous wireless sensor network based building energy and environment monitoring system design," *2010 2nd Conf. on Environmental Sci. and Inform. Applicat. Tech.*, vol. 3, pp. 367-372, July 2010.

[15] N. Kong and D. S. Ha, "Low-power design of a self-powered piezoelectric energy harvesting system with maximum power point tracking," *IEEE Trans. Power Electron.*, vol. 27, pp. 2298-2308, Feb. 2011.

[16] S. Roundy, P. K. Wright, and J. Rabaey, "A study of low level vibrations as a power source for wireless sensor nodes," *Computer Communications*, vol. 26, pp. 1131-1144, July 2003.

[17] G. K. Ottman *et al.*, "Adaptive piezoelectric energy harvesting circuit for wireless remote power supply," *IEEE Trans, Power Electron.*, vol. 17, pp. 669-676, Nov. 2002.

[18] G. K. Ottman, H. F. Hofmann, and G. A. Lesieutre, "Optimized piezoelectric energy harvesting circuit using step-down converter in discontinuous conduction mode," *IEEE Trans. Power Electron.*, vol. 18, pp. 699-703, Mar. 2003.

[19] R. W. Erickson and D. Maksimovic, *Fundamentals of Power Electronics*, 2nd Ed., Kluwer Academic Publishers, 2001.

[20] N. Kong *et al.*, "Resistive impedance matching circuit for piezoelectric energy harvesting," *J. of Intell. Mater. Syst. and Struct.*, vol. 0, pp. 1-10, Jan. 2010.

[21] N. Kong *et al.*, "A self-powered power management circuit for energy harvested by a piezoelectric cantilever," *Applied Power Electronics Conference and Exposition*, pp. 2154-2160, Feb. 2010.

[22] A. Erturk and D. J. Inman, "On mechanical modeling of cantilevered piezoelectric vibration energy harvesters," *J. of Intell. Mater. Syst. and Struct.*, vol. 19, pp. 1311-1325, Apr. 2008.

[23] J. Yuan, T. Xie, and W. Chen, "Energy harvesting with piezoelectric cantilever," *2008 IEEE International Ultrasonics Symposium Proceedings*, pp.1397-1400, Nov. 2008.

[24] A. M. Flynn and S. R. Sanders, "Fundamental limits on energy transfer and circuit considerations for piezoelectric transformers," *IEEE Trans. Power Electron.*, vol. 17, pp. 8-14, Aug. 2002.

[25] L. Ajitsaria *et al.*, "Modeling and analysis of a bimorph piezoelectric cantilever beam for voltage generation," *Smart Mater. Struct.*, vol. 16, pp.447-454, Feb. 2007.

[26] A. Khaligh, P. Zeng, and C. Zheng, "Kinetic energy harvesting using piezoelectric and electromagnetic technologies-state of the art," *IEEE Trans. Ind. Electro.*, vol. 57, pp. 850-860, Feb. 2010.

[27] N. G. Elvin and A. A. Elvin, "A general equivalent circuit model for piezoelectric generators," *J. of Intell. Mater. Syst. and Struct.*, vol. 20, pp. 3-9, May 2009.

[28] H. A. Sodano, G. Park, and D. J. Inman, "Estimation of electric charge output for piezoelectric energy harvesting," *Strain Journal*, vol. 40, pp. 49-58, 2004.

[29] N. E. duToit, B. L. Wardle, and S. Kim, "Design considerations for MEMS-scale piezoelectric mechanical vibration energy harvesters," *J. Vib. Acoust.*, vol. 71, pp. 121-160, Feb. 2005.

[30] H. A. Sodano *et al.*, "Model of piezoelectric power harvesting beam," *International Mechanical Engineering Congress and Exposition*, pp. 345-354, Nov. 2003.

[31] J. Ziprick, "Hamiltonian quantization with constraints," B.Sc. thesis, Dept. of Phys., Univ. of Winnipeg, Winnipeg, MB, 2009.

[32] N. E. duToit, "Modeling and design of a MEMS piezoelectric vibration energy harvester," M.S. thesis, Dept. Aero. Astro., MIT, Cambridge, MA, 2005.

[33] I. Newton, *Philosophiæ Naturalis Principia Mathematica*, Philosophical Transactions of the Royal Society, 1687.

[34] Y. Yang and L. Tang, "Equivalent circuit modeling of piezoelectric energy harvesters," *J. of Intell. Mater. Syst. and Struct.*, vol. 20, pp. 2223-2235, Oct. 2009.

[35] Z. S. Chen, Y. M. Yang, and G. Q. Deng, "Analytical and experimental study on vibration energy harvesting behaviors of piezoelectric cantilevers with different geometries," *2009 International Conference on Sustainable Power Generation and Supply*, pp. 1-6, 2009.

[36] MicroGen Systems Inc. Rochester, New York, USA. www.microgensystems.com.